

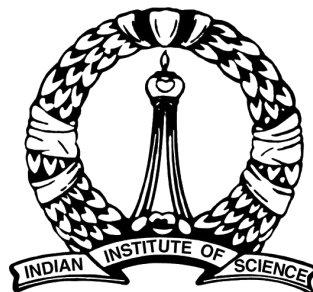
Numerical and experimental investigation of Process-Structure-Property relationship in Organic Photovoltaics

A Thesis

Submitted for the Degree of
Doctor of philosophy
in the **Faculty of Engineering**

by

Fiyanshu Kaka



Department of Materials Engineering
Indian Institute of Science
Bangalore – 560 012 (INDIA)

September 2020

© Fiyanshu Kaka
September 2020
All rights reserved

DEDICATED TO

My Dear Mother

Acknowledgements

I express sincere gratitude to my advisors Prof. Abhik N Choudhury and Prof. Praveen C Ramamurthy, for guiding me through this odyssey and providing computational and experimental resources. Frankly, this thesis would not be in the shape it is today without their support and critical suggestions.

I also take this opportunity to thank past and present Chairman Prof. T.A. Abinandanan and Prof. Satyam Suwas for providing departmental facilities. A substantial portion of the simulations done in this thesis was performed at SERC and SSCU facilities; I would like to acknowledge them for providing computational resources 24x7.

I feel grateful to have found wonderful friends in my labmates Sumeet, Kiran, Bhalchandra, Arka da, Kavita, Jagdish and Arul. They were all ears to my challenges and always reverted with their invaluable counsel. When I came to Materials Engg. Department from a Polymer Engg. background, it was Kiran who ensured my smooth transition. My seniors Arka da, Bhalchandra Jagdish, Kavita and Arul were always available for their inputs. Last but not least, thanks Sumeet for everything; I admire your generosity.

Synopsis

The world energy requirement is heavily dependent on fossil fuels that are both limited in quantity and have serious environmental repercussions. It is well known that fossil fuel reserves around the world are fast depleting and we are experiencing global warming as a result of the release of greenhouse gases due to the burning of fossil fuels. Therefore, it becomes imperative to look for alternative renewable sources of energy. Since solar energy is abundantly available, it becomes natural to think of tapping it for our energy requirements. Amongst various solar technologies, the third generation solar cells, namely Organic Photovoltaics (OPVs) have garnered significant research interest. The primary reason for their popularity has been the possibility of applying various cost-effective solvent-based techniques for active layer deposition such as spin-coating, ink-jet and flexographic printing. Also, organic solar cells combine the advantages of plastics, i.e., lightweight and ease of molecular synthesis with the semiconducting nature of conjugated molecules and therefore, have found a niche application in flexible electronics. It has been over three decades since OPVs were discovered and they have made tremendous progress in terms of tapping the solar energy. In 1986, when Tang [1] developed a bilayer organic solar cell, it rendered a power conversion efficiency of about 1%, and today organic solar cells have achieved 17%[2] power conversion efficiency. This improvement has been possible due to significant advances in morphology design, device architecture, organic semiconductor synthesis, transport layers, processing techniques and understanding of device physics.

The device performance of OPVs is controlled by the underlying complex Bulk-Heterojunction (BHJ) morphology which is in turn influenced by the processing parameters such as blend composition, annealing time and evaporation rate of solvent. The focus of this thesis is on optimising OPV performance by understanding the Process-Structure-Property (PSP) correlation in organic-semiconductors as depicted in Figure 1. In this thesis, firstly, experiments have been carried out on model P3HT:PCBM (donor-acceptor) system to study the effect of blend ratio between polymer (P3HT) and fullerene derivative (PCBM) as well as the influence of annealing time on device performance. However, since the optimization of the processing parameters,

0. SYNOPSIS

particularly for deriving active-layer BHJ morphologies with high efficiencies is non-trivial as the parameter space is large, the adoption of a theoretical framework becomes necessary.

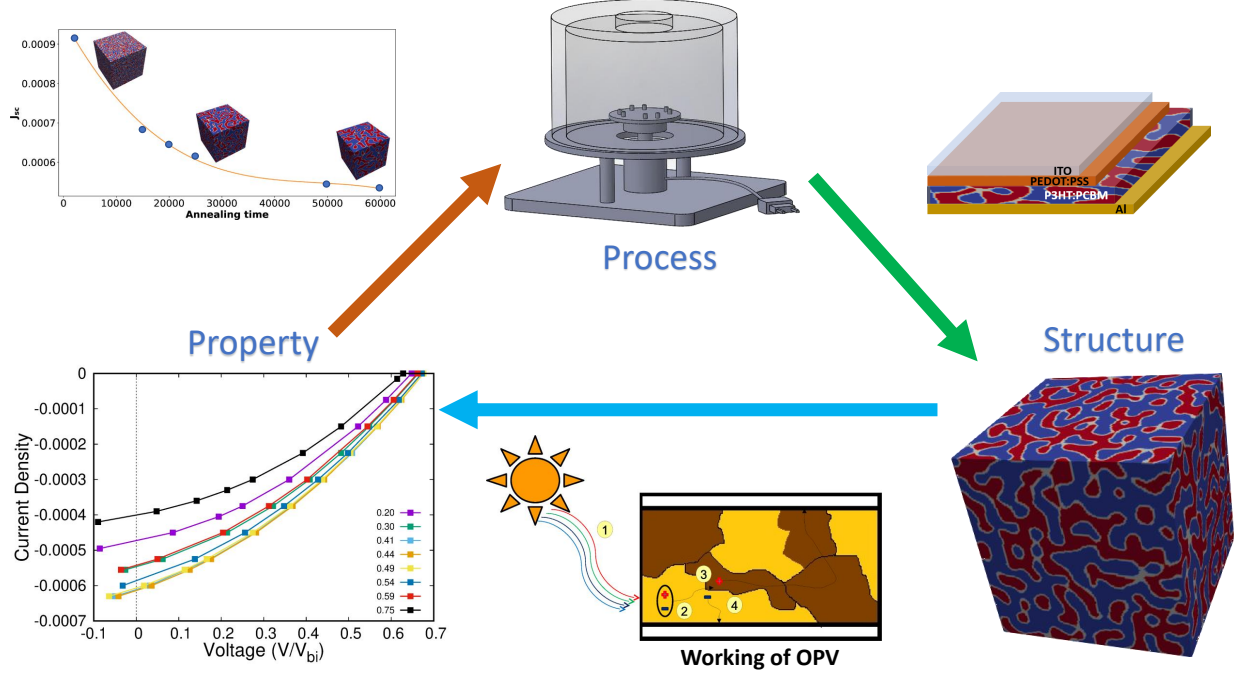


Figure 1: PSP relationship in OPVs

In the theoretical framework, we present an elegant approach for deriving both the process-structure and structure-property correlations based on the diffuse-interface method. Herein, we derive process-structure correlations using phase-field simulations based on the Cahn-Hilliard formalism for modeling phase-separation. A range of morphologies as a result of processing parameters such as blend ratio, annealing time, and evaporation rate of solvent is generated using the process-structure model. Thereafter, we derive the structure-property correlations again using a diffuse interface approach for calculating the electronic properties such as the Power Conversion Efficiency (PCE), Fill-Factor (FF), short-circuit current density (J_{sc}), and the open-circuit voltage (V_{oc}) for the simulated microstructures. We have adopted a diffuse interface approach to model structure-property relationship in order to incorporate heterogeneities in electronic properties and solve for the drift-diffusion equation where the sharp interface between the domains is smeared over a finite length. This diffuse-interface mapping, however, requires that the driving forces for the diffusion are determined based on the gradients of the chemical potential of the electrons and holes respectively. Therefore, we have chosen

0. SYNOPSIS

the chemical potential as well as the electrostatic potential as the two-state variables for the structure-property model, whereby the gradients of the chemical potential and the electrostatic potential describe the driving forces for diffusion and drift respectively. The advantage of the diffuse interface approach is that the boundary conditions at the interface are imposed implicitly, thus allowing for easier computational treatment of complex geometries as in case of BHJ OPVs. Also since the dynamic variable in our model is the electrochemical potential instead of the concentration, this leads to a more straightforward numerical treatment since, as the steady-state approaches, at the interface, the gradient in electrochemical potential diminishes. In contrast, the concentration sees variations differing by orders of magnitude. The structure-property model is benchmarked against analytical results obtained from the classical sharp interface model. Thus, utilizing the combination of the diffuse-interface process–structure and structure-property correlations, the optimal composition for Donor-Acceptor OPVs has been determined.

However, since Donor-Acceptor OPVs possess a limited absorption of the solar spectrum, and the addition of a ternary component with a complementary absorption spectrum addresses this issue, we carried out experimental studies on Donor-Acceptor-Acceptor OPVs. Here, experiments exploring the effect of blend ratio on device performance were conducted on PTB7-Th, CoI8DFIC, and PCBM ternary system. The experiments motivated the numerical studies wherein the PSP relationship in ternary OPVs has been optimized using the above-mentioned theoretical framework. Further, in order to expedite the theoretical prediction, a robust and elegant data analytics model is built wherein using the simulated data, the photovoltaic properties are predicted without the need for running additional computationally-intensive simulations for intermediate blend ratios. In order to develop the data analytics model, we first represent the microstructure quantitatively [3] using spatial 2-point correlation maps of the phases [4, 5, 6, 7]. The dimensionality of the vectorised 2-point correlation maps is further reduced by using Principal Component Analysis (PCA) to concisely capture the features that show maximum variance in the dataset [8, 9, 10]. The Principal Components (PCs) act as a bridge between the processing conditions and photovoltaic properties thus facilitating the establishment of PSP correlations in Donor-Acceptor-Acceptor OPVs. This work is done in the broad overview of the Integrated Computational Materials Engineering (ICME) framework wherein the processing parameters are optimised by determining the process-structure-property relationships.

The results obtained for the above-mentioned studies are briefly described in the following sections:

0. SYNOPSIS

Experimentation

Firstly, experiments were carried out on model P3HT:PCBM (donor-acceptor) system for the conventional device architecture (Figure 2(a)) to study the effect of blend ratio between polymer (P3HT) and fullerene derivative (PCBM) as well as the influence of annealing time on device performance. We observed that there is an optimal composition at which the device efficiency is maximised as seen in Figure 2(b). Further, it is seen that the short-circuit current density (J_{sc}) gets optimised at one particular annealing time (Figure 2(c)). Secondly, since ternary OPVs are state-of-the-art polymer solar cells and exhibit better device characteristics and stability, experiments were done on Donor-Acceptor-Acceptor (DAA) ternary blend comprising PTB7-Th, COi8DFIC and PC₇₀BM for the device architecture shown in Figure 3(a). The effect of ternary component's weight ratio on device efficiency for DAA blend is depicted in Figure 3(b). Here again, we observed an optimal composition with respect to device efficiency.

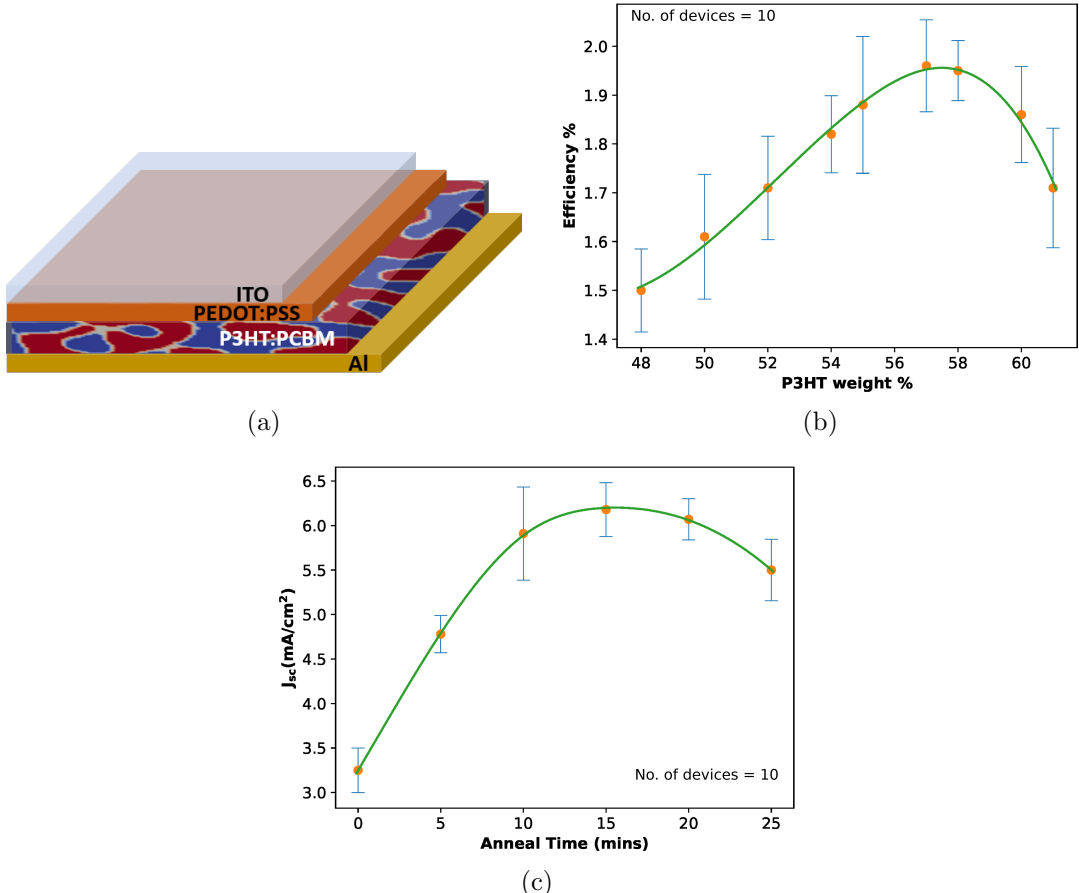


Figure 2: (a) Device architecture (b) Experimental efficiency vs weight % of PCBM (c) Experimental J_{sc} vs annealing time

0. SYNOPSIS

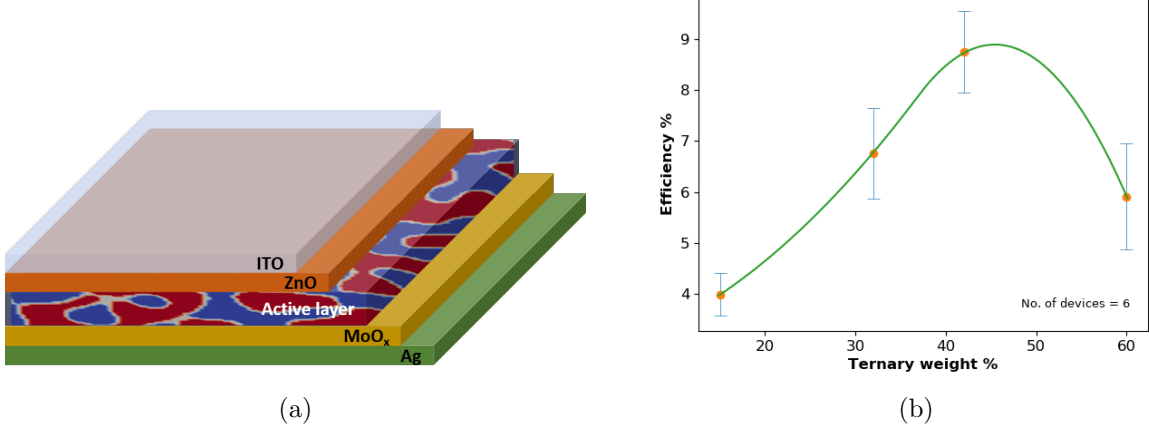


Figure 3: (a) Device architecture (b) Experimental efficiency vs weight % of ternary acceptor

These experimental studies set the motivation for investigating the PSP relationship in OPVs, which was carried out in the following chapters.

Donor-Acceptor OPVs

In order to understand and quantify the morphological features that influence device performance as was seen experimentally, we modeled the process-structure-property relationship using the diffuse-interface approach in Donor-Acceptor OPVs. We first established process-structure correlations by generating a range of morphologies with various blend ratios of donor and acceptor organic-semiconductor for different annealing periods. Secondly, we calculated effective electronic properties corresponding to the simulated structures. The results from the theoretical framework seem to follow trends similar to those from the experimental measurements (Figure 4(a)). We find that the necessary condition for fabricating an efficient OPV device is the existence of a bi-continuous network of donor and acceptor phases as this leads to percolating channels for electrons and holes to their respective electrodes (Figure 4(b)). Amongst the percolating morphologies, the ones with a higher interfacial area lead to higher short circuit current density (J_{sc}) and eventually to a better efficiency owing to a higher generation of carriers at the interface.

Having established the PSP relationship in Donor-Acceptor OPVs, we went on to investigate the same in sophisticated Donor-Acceptor-Acceptor OPVs.

0. SYNOPSIS

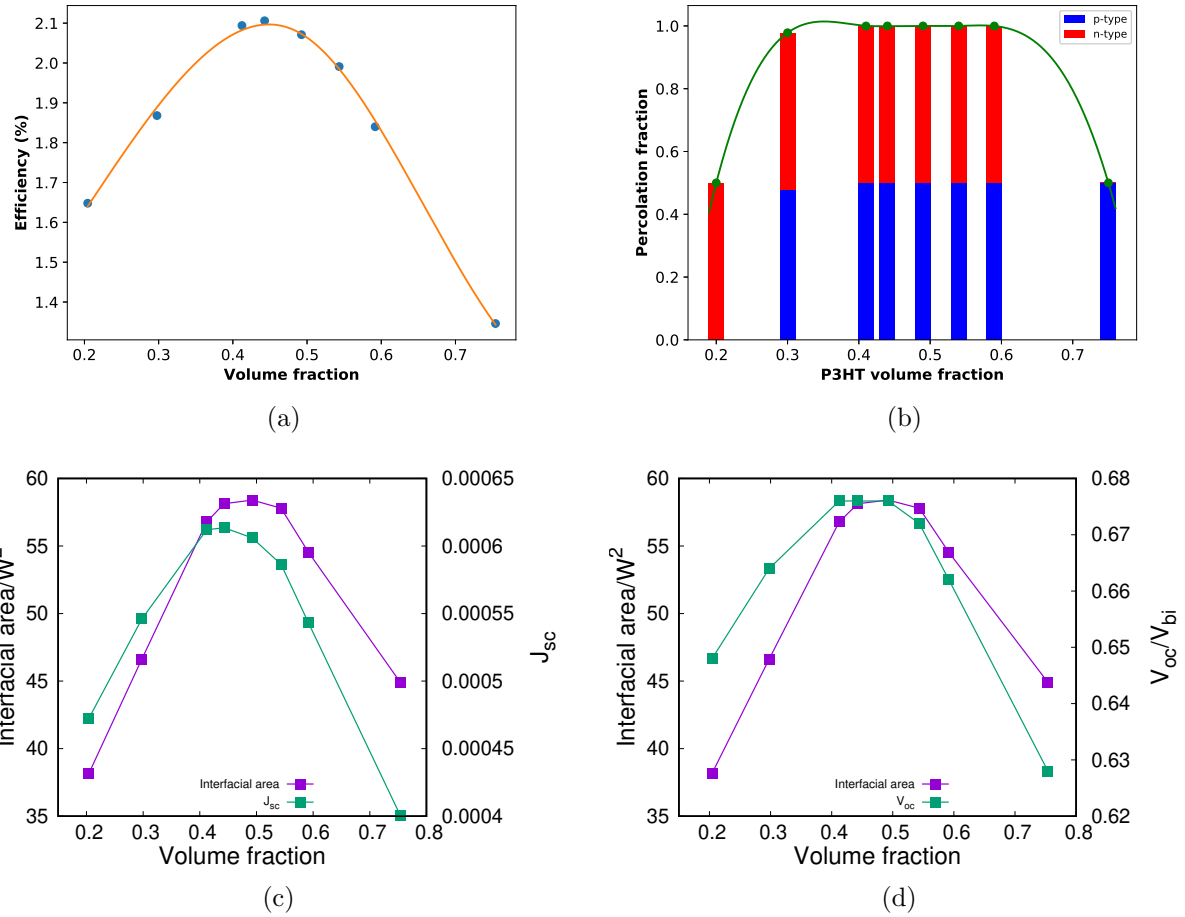


Figure 4: Simulation results depicting (a) efficiency vs volume fraction (b) percolation fraction vs volume fraction (c) J_{sc} and interfacial area vs volume fraction (d) V_{oc} and interfacial area vs volume fraction. The interfacial area has been normalised with respect to the square of depletion width (W). Note: The lines have been drawn just to follow the points and have no physical significance.

0. SYNOPSIS

Donor-Acceptor-Acceptor OPVs

In this chapter, we derive process-structure correlations for the ternary system where a third component acting as an acceptor is added to a binary OPV. This leads to structures that can be classified as Donor-Acceptor-Acceptor (DAA). Thereafter, we derive the structure-property correlations using the diffuse-interface approach for the simulated microstructures involving the three-phases in the active-layer. We used geometrical descriptors of morphology such as interface area, tortuosity and percolation fraction to analyse the variation of the simulated microstructure with photovoltaic properties such as J_{sc} , V_{oc} , FF and PCE. It has been found that the percolation fraction and interface area have a strong influence on device performance (Figure 5). While the morphological descriptors are critical characteristics of the morphology and influence the device performance, the set of geometrical descriptors that can describe the entire range of shapes of the donor and acceptor phases may sometimes be large given the variety of morphologies that the phases can assume. Moreover, the arrangement of the phases within the microstructure is not directly captured by the given geometrical parameters. These features influence the local electric field, the carrier conduction pathways and subsequently, the photovoltaic properties. This difficulty in precisely capturing all the features of the morphology using geometrical descriptors, sets the motivation for using data-science in this work that further aids in expediting the identification of optimal morphology. In the data analytics model, a statistical representation of the microstructure using spatial correlation maps and dimensionality reduction techniques has been adopted. Thereafter, a maximisation of PCE has been performed in order to identify the corresponding blend ratio which had not been explored using the structure-property simulations. Therefore, given the donors and acceptors for fabricating ternary OPVs, the morphologies resulting in sub-optimal device performance can be screened out, and the probable blend ratios for maximal device performance can be identified. This *in silico* framework comprising physics-based and data-science approach would accelerate the optimisation of ternary blend morphology for device fabrication.

Evaporation induced phase-separation in Donor-Acceptor OPVs

In the last chapter of this thesis, we explore the effect of the solvent evaporation rate and the Donor-Acceptor blend composition on the active-layer morphology and subsequently on the device performance. The active-layer deposition involves two processes, i.e., evaporation of

0. SYNOPSIS

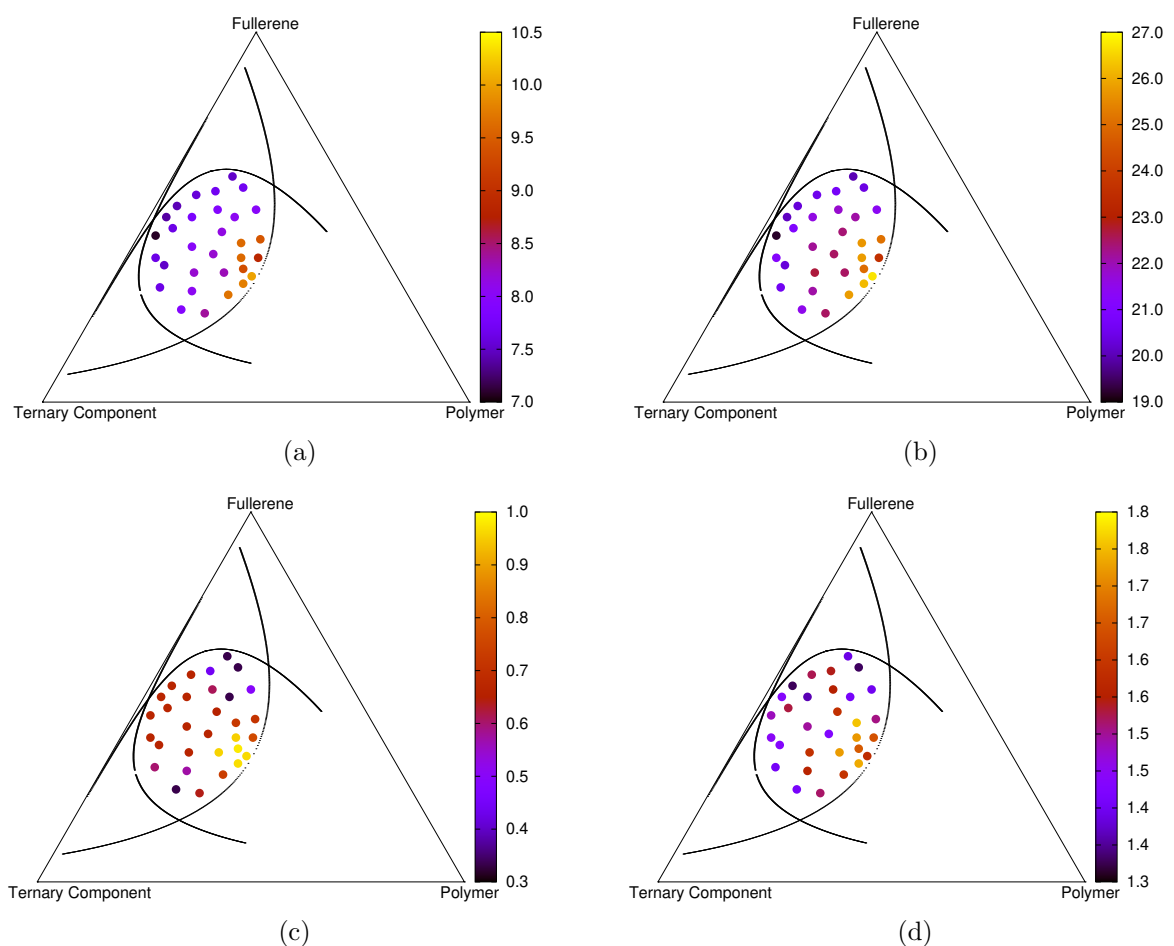


Figure 5: Simulation results depicting the variation of (a) efficiency, and morphological descriptors such as (b) total interface area, (c) percolation fraction and (d) tortuosity with blend ratio on simplex. The tri-percolating morphologies have been found to exhibit highest efficiencies.

0. SYNOPSIS

the solvent and the phase-separation of the Donor-Acceptor blend. The relative rates of the two processes, i.e., solvent evaporation rate at the top surface and diffusion rate of the donor (polymer) and acceptor (fullerene) molecules within the film is represented by the Mass Biot number (Bi_m) which influences the resulting microstructure, particularly along the thickness of the film and eventually the photovoltaic properties namely J_{sc} , V_{oc} , FF and PCE. The variation of the microstructure along the thickness of the active layer and its evolution with time for various Bi_m and blend compositions has been investigated using the process-structure model and further mapped to the photovoltaic parameters using the structure-property model. This is essential since if the top region of the organic semiconductor film (active layer) exhibits optimal performance, whereas the bottom region exhibits sub-optimal performance, the effective electronic properties of the device are adversely affected. We found that there exists a threshold Bi_m (that varies depending on the initial blend ratio), below which the bottom region of the active layer does not phase-separate thus deteriorating the PCE. Also, it was observed that at high Bi_m , the resulting morphology possesses fine domains (see Figure 6). This resulted in higher interfacial area and thus higher generation of carriers, subsequently leading to high J_{sc} , V_{oc} and PCE as depicted in Figure 7. Since optimal device performance is a result of bi-percolating microstructure and high interfacial area, we further analysed the effect of blend composition on device performance by probing different initial donor-acceptor blend ratios.

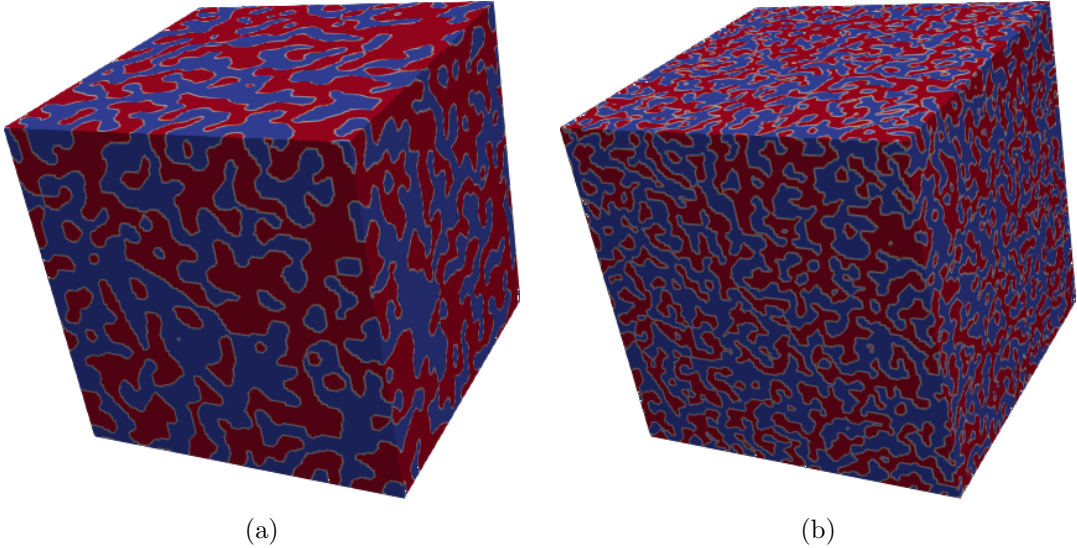


Figure 6: Microstructure for element 4 corresponding to (a) $Bi_m = 0.01$ and (b) $Bi_m = 1.66$. Microstructure resulting from a high Bi_m has fine domains whereas the one with low Bi_m has coarse domains.

0. SYNOPSIS

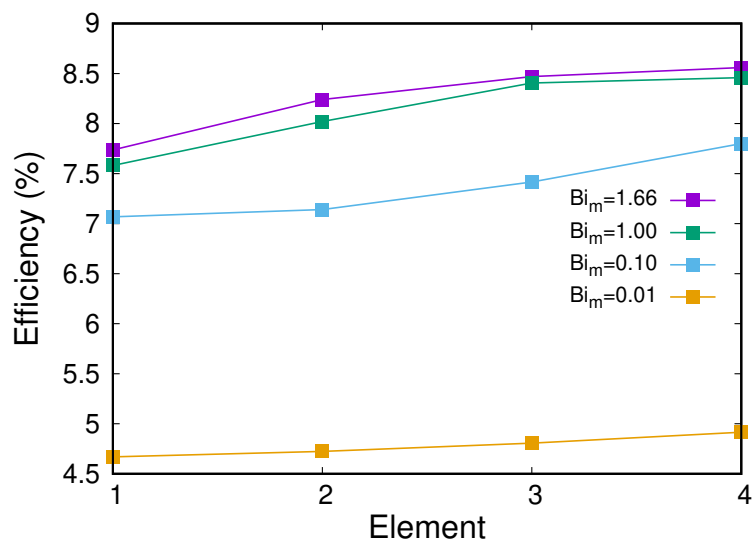


Figure 7: Simulation results depicting efficiency as a function of element for blend composition 0.10:0.45:0.45 for various Bi_m .

Contents

Acknowledgements	i
Synopsis	ii
Contents	xii
List of Figures	xvi
List of Tables	xxi
List of Symbols	xxii
1 Introduction	1
1.1 Brief historical context of organic solar cells	1
1.2 Working of OPV:	2
1.2.1 Charge-conduction mechanism	2
1.2.1.1 Morphology Engineering	4
1.3 Essential characteristics of organic solar cells	4
1.4 Bottlenecks and opportunities in OPVs	7
1.5 Phase-field modeling	8
1.6 Materials Data Science	9
2 Literature review and motivation	12
2.1 Donor-Acceptor OPVs	12
2.2 Donor-Acceptor-Acceptor (DAA) OPVs	17
2.3 Evaporation induced phase-separation during spin-coating	19
3 Experimentation	21
3.1 Experimental protocol	21

CONTENTS

3.1.1	Materials used	21
3.1.1.1	Substrate and top-contact electrode	21
3.1.1.2	Hole Transport Layer (HTL)	22
3.1.1.3	Active layer	22
3.1.1.4	Electron Transport Layer (ETL)	22
3.1.1.5	Bottom-contact electrode	22
3.1.2	Device fabrication protocol	23
3.1.2.1	Solution preparation	23
3.1.2.2	Substrate cleaning and treatment	23
3.1.2.3	Deposition of the transport layers	23
3.1.2.4	Spin-coating the active layer	24
3.1.2.5	Evaporation of bottom-contact electrode	24
3.2	OPV characterisation	25
3.2.1	J-V characteristics	25
3.2.2	Stylus profilometer	25
3.2.3	Atomic Force Microscope (AFM)	26
3.2.4	Scanning Transmission X-ray Microscopy (STXM)	27
3.3	Binary OPVs	27
3.4	Ternary OPVs	28
4	Formulation	33
4.1	Process-structure model	33
4.1.1	Energy of a compositionally inhomogeneous system	34
4.1.2	Kinetics	36
4.1.3	Non-dimensionalization for process-structure model	39
4.1.4	Numerical solution	39
4.2	Structure-property model	40
4.2.1	Semiconductor equations	40
4.2.2	Free-Energy	44
4.2.3	Model Formulation	44
4.2.4	Non-Dimensionalization for Structure-Property model	47
4.2.5	System Initialization	47
4.2.6	Benchmarking structure-property model	49
4.2.7	BHJ-Morphology	51
4.3	Assumptions	51

CONTENTS

5 Donor-Acceptor OPVs	58
5.1 Model parameters	58
5.1.1 Process-structure relationship	58
5.1.2 Structure-property relationship	60
5.2 Numerically optimal blend ratio for device fabrication	60
5.3 Analysis	63
5.3.1 Effect of blend-ratio	63
5.3.2 Effect of Annealing	64
5.4 Summary	64
6 Donor-Acceptor-Acceptor OPVs	67
6.1 Model parameters	67
6.1.1 Process-structure relationship	67
6.1.2 Structure-property relationship	68
6.2 Results	70
6.3 Quantitative Microstructure Characterization	76
6.4 Summary	82
7 Evaporation induced phase-separation in Donor-Acceptor OPVs	83
7.1 Introduction	83
7.2 Modeling	84
7.2.1 Evaporation model	84
7.2.2 Process-structure relationship	87
7.2.3 Structure-property relationship	88
7.3 Results	89
7.4 Summary	98
8 Conclusions & Outlook	103
8.1 Experiments	104
8.2 Donor-Acceptor OPVs	104
8.3 Donor-Acceptor-Acceptor OPVs	105
8.4 Evaporation induced phase-separation in Donor- Acceptor OPVs	105
Appendices	108
Bibliography	112

CONTENTS

List of Figures

1	PSP relationship in OPVs	iii
2	(a) Device architecture (b) Experimental efficiency vs weight % of PCBM (c) Experimental J_{sc} vs annealing time	v
3	(a) Device architecture (b) Experimental efficiency vs weight % of ternary acceptor	vi
4	Simulation results depicting (a) efficiency vs volume fraction (b) percolation fraction vs volume fraction (c) J_{sc} and interfacial area vs volume fraction (d) V_{oc} and interfacial area vs volume fraction. The interfacial area has been normalised with respect to the square of depletion width (W). Note: The lines have been drawn just to follow the points and have no physical significance.	vii
5	Simulation results depicting the variation of (a) efficiency, and morphological descriptors such as (b) total interface area, (c) percolation fraction and (d) tortuosity with blend ratio on simplex. The tri-percolating morphologies have been found to exhibit highest efficiencies.	ix
6	Microstructure for element 4 corresponding to (a) $Bi_m = 0.01$ and (b) $Bi_m = 1.66$. Microstructure resulting from a high Bi_m has fine domains whereas the one with low Bi_m has coarse domains.	x
7	Simulation results depicting efficiency as a function of element for blend composition 0.10:0.45:0.45 for various Bi_m	xi
1.1	Schematic depicting working mechanism of BHJ OPV	4
1.2	Schematic of J-V curve. Blue curve corresponds to the J-V curve whereas green curve corresponds to the power that can be extracted from the device.	5
1.3	Standardised solar spectrum for various Air Mass(AM) coefficients.	7
3.1	(a) Substrate with ITO coating shown in black and glass in pink. (b) Spin-coated substrate with three sides of the film scraped off, the active layer is depicted by orange color and the scraped off region by yellow color.	24

LIST OF FIGURES

3.2	Six device pixels represented by the overlap between top-contact and bottom-contact electrode.	25
3.3	(a) Device architecture (b) energy band diagram (c) experimental efficiency vs weight % of PCBM (d) experimental J_{sc} vs annealing time Note: The lines have been drawn using spline interpolation just to follow the points and have no physical significance.	29
3.4	Phase contrast image of P3HT:PCBM active layer for 1:0.8 blend ratio. The light yellow phase corresponds to P3HT fibrils whereas dark brown phase corresponds to PCBM.	30
3.5	(a) Device architecture (b) energy band diagram (c) experimental efficiency vs weight % of ternary acceptor. Note: The lines have been drawn using spline interpolation just to follow the points and have no physical significance.	31
3.6	PC ₇₀ BM is depicted by green color and PTB7-Th by red. The domains size is around 100 nm.	32
4.1	(a) Bulk free energy for a representative system (a, b and c represent polymer, fullerene and ternary component respectively) with $\chi_{ab} = \chi_{bc} = \chi_{ca} = 3$, $N'_a = 5$, $N'_b = 1$ and $N'_c = 1$. (b) Isothermal section of the phase diagram for polymer, fullerene and ternary component.	35
4.2	Surface profiles of the morphologies generated using the process-structure model that have been binarised and then smoothed for incorporation in the structure-property model.	43
4.3	Device with a representative BHJ morphology sandwiched between the electron and hole transport layers. The HTL is represented by blue color whereas ETL by grey color. On the color bar, 0 corresponds to the polymer-rich phase, 1 corresponds to fullerene rich phase, and 2 corresponds to ternary component rich phase	48
4.4	Morphology of bilayer device. 1 represents p-type Organic Semiconductor (OS), and 0 represents n-type OS with junction having a diffuse profile.	50
4.5	Simulation results depicting (a) electrostatic potential profile (b) charge density profile (c) variation in depletion width with bias.	52
4.6	Simulation results depicting (a) dark J-V characteristics (b) effect of light intensity on device characteristics, G_o is the coefficient of generation rate of carriers.	53
4.7	BHJ morphology with blend ratio 1:2.5.	54

LIST OF FIGURES

4.8	Simulation results depicting dark and light J-V characteristics of device with BHJ morphology of active layer.	55
5.1	(a) Isothermal section of the phase diagram of P3HT, PCBM and CB. BHJ morphology with blend ratio (b) 1:1.25 (c) 1:1.5 (d) 1:2.0 (e) 1:2.2 (f) 1:5.4 On the color bar, 0 corresponds to PCBM rich phase whereas 1 corresponds to P3HT rich phase	59
5.2	BHJ morphology with blend ratio (a) 1:5.4 (b) 1:3.5 (c) 1:2.0 (d) 1:1.5 (e) 1:1.25 (f) 1:0.8	61
5.3	Simulation results depicting (a) J-V characteristics of morphologies with different volume fractions of P3HT (b) efficiency vs volume fraction. Note: The lines have been drawn using spline interpolation just to follow the points and have no physical significance.	62
5.4	Simulation results depicting (a) percolation fraction vs volume fraction (b) J_{sc} and interfacial area vs volume fraction (c) V_{oc} and interfacial area vs volume fraction. Note: The lines have been drawn using spline interpolation just to follow the points and have no physical significance.	65
5.5	Simulation results depicting the effect of annealing on J_{sc} . Note: The lines have been drawn using spline interpolation just to follow the points and have no physical significance.	66
6.1	(a) Isothermal section of the phase diagram for polymer, fullerene and ternary component. BHJ morphologies with volume fraction of polymer, fullerene and ternary component (b) 0.04:0.45:0.51 (c) 0.17:0.55:0.28 (d) 0.20:0.25:0.55 (e) 0.31:0.39:0.30 On the color bar, 0 corresponds to polymer rich phase, 1 corresponds to fullerene rich phase and 2 corresponds to ternary component rich phase	69
6.2	Simulated J-V characteristics of a device with blend composition 0.32:0.34:0.34. These characteristics have been further processed to extract photovoltaic parameters i.e., J_{sc} , V_{oc} and FF	70
6.3	Schematic depicting the calculation of the length of the percolating cluster. In yellow is shown the percolating cluster and the black line represents the path traced by the centroid of the cluster at each XZ plane.	72
6.4	Simulation results depicting the variation of (a) efficiency (PCE), (b) total interface area, (c) percolation fraction and (d) tortuosity with time.	73

LIST OF FIGURES

6.5 (a) Efficiency, (b) total interface area, (c) percolation fraction and (d) tortuosity maps on simplex depicting the variation of PCE and morphological descriptors with blend ratio as obtained using simulations. The tri-percolating morphologies have been found to exhibit highest efficiencies.	75
6.6 Morphology of device exhibiting highest efficiency (blend composition: 0.32:0.34:0.34) on the left and lowest efficiency (blend composition: 0.04:0.45:0.51) on the right for DAA system. On the color bar, 0 corresponds to polymer rich phase, 1 corresponds to fullerene rich phase and 2 corresponds to ternary component rich phase.	76
6.7 Maps of photovoltaic parameters (a) J_{sc} , (b) FF and (c) V_{oc} extracted from the simulation data on simplex depicting their variation as a function of blend composition.	77
6.8 PC 's fitted with ϕ_p and ϕ_f (a) PC_0 (b) PC_1 and (c) PC_2 with $r^2 \approx 0.994$, $r^2 \approx 0.998$ and $r^2 \approx 0.85$ respectively.	79
6.9 Predicted J_{sc} and η values using linear regression with PC_1 , PC_2 and ϕ_p as independent variables against the simulated J_{sc} and η . (a) J_{sc} , $r^2 = 0.93$ (b) η , $r^2 = 0.88$. The dashed line mathematically represents $y = x$ and solid line depicts fit of the predicted data.	80
6.10 Simulated (a) J_{sc} and (b) η values in color plotted against the PC_1 and PC_2 scores. It can be noted that J_{sc} and η vary inversely with PC_1 and PC_2 scores.	81
6.11 Plot depicting η as a function of ϕ_p and ϕ_f . The maximum η is obtained for the blend composition 0.34:0.32:0.34 with respect to polymer, fullerene and ternary acceptor.	81
7.1 Evaporation induced phase-separation (a) CAD model of spin-coater. (b) Simplex representing the evaporation of solvent pushing the system to spinodal regime. (c) Schematic representing the stages of film formation during spin-coating.	85
7.2 Schematic depicting the representative elements that are tracked for polymer and fullerene volume fraction and the decrease in their heights with time.	87
7.3 Volume fraction profiles in the 1D domain with time for (a) Polymer (ϕ_p) and (b) Fullerene (ϕ_f). Note: The system height has been normalised with respect to itself at each time step in this figure.	91
7.4 Volume fraction profiles for elements 1-4 with time for (a) Polymer (ϕ_p) and (b) Fullerene (ϕ_f)	92

LIST OF FIGURES

7.5 Morphology evolution of elements 1-4 as a function of time for $Bi_m = 1.66$. On the colorbar 0 corresponds to polymer rich phase whereas 1 corresponds to fullerene rich phase.	93
7.6 Microstructure for element 4 corresponding to (a) $Bi_m = 0.01$ and (b) $Bi_m = 1.66$. Microstructure resulting from a high Bi_m has fine domains whereas the one with low Bi_m has coarse domains.	94
7.7 Map of B in the spinodal regime on the simplex. It can be observed that the magnitude of B is higher in the interior of the spinodal regime and lower at the periphery. The red curve corresponds to the polymer-fullerene binodal.	94
7.8 Morphologies of various elements for blend composition 0.15:0.38:0.47. It can be observed that element 1 has not phase-separated whereas elements 2-4 have undergone spinodal decomposition. On the colorbar 0 corresponds to polymer rich phase whereas 1 corresponds to fullerene rich phase.	95
7.9 Isothermal section of the polymer-fullerene-solvent phase-diagram with points a, b and c corresponding to blend compositions 0.30:0.30:0.40, 0.15:0.38:0.47 and 0.03:0.52:0.45 respectively. The green portion of the curve represents the spinodal region.	96
7.10 Simulation results depicting (a) interfacial area normalised by square of depletion width (W) (b) tortuosity as a function of element for blend composition 0.10:0.45:0.45 for $Bi_m = 1.66$, $Bi_m = 1.00$, $Bi_m = 0.10$, and $Bi_m = 0.01$	97
7.11 Simulated J-V characteristics of element 4 for the blend composition 0.10:0.45:0.45.	99
7.12 Simulation results depicting efficiency as a function of element for blend composition 0.10:0.45:0.45 for various Bi_m	99
7.13 Simulation results depicting (a) Efficiency, (b) Short-circuit current density (J_{sc}), (c) Open-circuit voltage (V_{oc}) and (d) Fill Factor as a function of element for blend compositions 0.30:0.30:0.40, 0.10:0.45:0.45 and 0.02:0.60:0.38. All the elements corresponding to the blend composition 0.10:0.45:0.45 which is symmetric with respect to miscibility gap perform better than the other blend composition in terms of PCE.	100
7.14 Simulation results depicting (a) interfacial area and (b) tortuosity as a function of element for blend compositions 0.30:0.30:0.40, 0.10:0.45:0.45 and 0.02:0.60:0.38.	101

List of Tables

5.1	Process-Structure model parameter table for Donor-Acceptor system.	58
5.2	Structure-Property model parameter table for Donor-Acceptor OPVs.	60
6.1	Process-Structure model parameter table for Donor-Acceptor-Acceptor system. .	68
6.2	Fermi energy levels of electron and hole for polymer, fullerene and ternary component rich phases.	70
6.3	Structure-Property model parameter table for DAA system.	71
6.4	Coefficients of the second order equation fitting PC.	78
6.5	Coefficients of the multivariable linear regression model to predict the J_{sc} and η from the PC scores for DAA system.	80
7.1	Process-Structure model parameter table for polymer, fullerene and solvent system. .	88
7.2	Structure-Property model parameter table for polymer, fullerene and solvent system.	88

List of Symbols

0. LIST OF SYMBOLS

Symbol	Description	Units
ϕ_i	Volume fraction of i^{th} species (polymer, fullerene or ternary component)	-
F	Free energy functional	J/m^3
f	Flory Huggins free energy	J/m^3
N'_i	Relative size of i^{th} species (polymer, fullerene or ternary component)	-
V_m	Reference molar volume	m^3/mol
R	Universal gas constant	$J/molK$
T	Temperature	K
χ_{ij}	Flory Huggins interaction parameter	-
μ'_i	Chemical potential	J/m^3
$\bar{\mu}_i$	Chemical diffusion potential in process-structure model	J/m^3
κ_i	Gradient energy coefficient	J/m
h^α	Interpolation polynomial	-
ψ_α	Indicator function of phase α	-
Λ_i	Mobility of polymer, fullerene or ternary component	$m^5/J.s$
ϵ^α	Dielectric constant of phase α	F/m
μ_i	Diffusion potential in electronic model	J/mol
$\tilde{\mu}_i$	Electrochemical potential	J/mol
ξ	Electrostatic potential	V
V_{bi}	Built-in potential	V
OPV	Organic Photovoltaics	-
BHJ	Bulk-Heterojunction	-
PSP	Process-Structure-Property	-
PC	Principal Component	-
DAA	Donor-Acceptor-Acceptor	-
P3HT	Poly(3-hexylthiophene-2,5-diyl)	-
PCBM	Phenyl-C ₆₁ -butyric acid methyl ester	-
V_{oc}	Open-circuit potential	V
FF	Fill-Factor	-
PCE	Power Conversion Efficiency	-
q_i	Charge density	C/mol
c_i	Carrier density	mol/m^3
N_i^α	Doping density in α phase	mol/m^3
D_i^α	Diffusivity of the i^{th} species in α phase	m^2/s
λ_i^α	Electronic mobility	$m^2/V.s$
E_i^α	Fermi level of the hole and electron in the α -phase	J/mol
x_i^α	Mole-fraction of the i^{th} species (electron or hole)	-
M_i^α	Chemical mobility of electron or hole	$mol^2.s/kg.m^3$
G_0	Coefficient of generation rate of carriers	$mol/m^3.s$
W	Depletion width	m
k	Evaporation constant	m/s
a_{ij}	Second derivative of free energy with respect to ϕ_i and ϕ_j	J/m^3
Bi_m	Mass Biot number	-

0. LIST OF SYMBOLS

Chapter 1

Introduction

This chapter introduces the solar cells and in particular, polymer solar cells. A brief history of solar cells is presented along with the developments that took place in organic semiconductors and the eventual lead up to organic photovoltaics. The peculiar working mechanism of polymer solar cells is discussed, and the critical electrical characteristics are described. Also, pithy description of phase-field modeling is given since it forms the backbone of the modeling work in this thesis.

1.1 Brief historical context of organic solar cells

In 1839, Becquerel first observed the photovoltaic effect, thus laying the foundation for solar cells [11, 12]. The experiment involved immersing a silicon chloride or silver bromide coated platinum electrode in an electrolyte and then illuminating the electrodes. Upon illumination, he observed the development of current and voltage across the electrodes. In solid-state devices, the photovoltaic effect was observed in 1876 by Adam and his student Day [13]. Their work demonstrated the simplest solar cell wherein a Selenium semiconductor was sandwiched between electrodes. However, it was Fritts who realised a solar cell module similar to the one we see on rooftops nowadays in 1883 [14]. It was only after the famous work of Einstein in 1905 that the photoelectric effect got a fundamental understanding [15]. The rectifying nature of the devices developed till the early 1900s was due to metal-semiconductor junction. However, these devices gave a power conversion efficiency of less than one per cent. On the parallel lines of the development of solar cells, in the early 20th century, studies were done on organic solids for determining their electronic properties such as photoelectric effect, photoconductivity, etc [16, 17, 18, 19]. The work on organic crystal was the inception of the field of organic semiconductors.

1. INTRODUCTION

In the mid 20th century, electroluminescence in cellulose film was discovered [20]. In 1953, the first known Organic Photovoltaic (OPV) device was fabricated by Calvin and Kearns [21]. They manufactured the solar cell by coating a thin film of oxidised tetramethyl p-phenylenediamine ($\text{TM}\phi\text{D}$) via evaporation on magnesium phthalocyanine (MgPh) disk. In the next year, i.e., 1954, at the Bell Labs, Chapin, Fuller and Pearson developed a doped Si solar cell wherein the rectifying contact was due to PN junction. The device had a power conversion efficiency of six percent [22]. The third quarter of 20th century saw focussed research on organic crystals such as anthracene and naphthalene [23, 24]. Since the organic crystals required high voltages (order of 100 V) for conduction, the research shifted to amorphous organic solids [25, 26]. The challenge plaguing the commercialisation of organic semiconductors was a requirement of high voltage for conduction owing to their large thickness. This was bypassed by using amorphous solids of a lower thickness of the order of 100 nm. The reporting of high conductivity in π -conjugated polymers further attracted more interest. Heeger, MacDiarmid and Shirakawa were conferred the Nobel prize in chemistry for this discovery [27]. It is only in the 1970s that alternative materials for photovoltaic devices began to be considered in order to bring down material costs. The reconsideration of organic semiconductor in photovoltaic devices resulted in a breakthrough in 1986 when Tang [1] developed a bilayer solar cell. The first Bulk-Heterojunction (BHJ) OPV as we know today was fabricated by Hiramoto et al., [28, 29]. They had developed a small molecule OPV using Me-PTC and H_2Pc pigments. In 1992, polymer BHJ OPV was reported by Sariciftci et. al [30]. They used MEH-PPV as the donor and buckminsterfullerene as an acceptor in the active layer. Subsequently, in 1995, Yu et. al [31], reported more efficient polymer BHJ OPVs by morphology control. In the next section, the charge conduction mechanism in BHJ OPVs will be discussed.

1.2 Working of OPV:

1.2.1 Charge-conduction mechanism

The charge-conduction mechanism in the active layer of BHJ-OPV is different from that of inorganic semiconductors, and that is the reason for its brief discussion here. The mechanism is schematically depicted in Fig.1.1, and the various steps are enumerated below:

1. As light shines on the OPV, photons are absorbed, and the electrons get excited. This leads to the formation of excitons. An exciton is a hole and electron pair bound together by coulombic force given by Eq.(1.1). These are created predominantly in the donor material.

1. INTRODUCTION

$$F = \frac{1}{4\pi\epsilon\epsilon_0} \frac{q_e q_h}{r^2} \quad (1.1)$$

where F represents the attractive force; ϵ and ϵ_0 are the absolute and vacuum permittivity; q_e , q_h are elementary charges of electron and hole respectively and r is the distance separating them.

In inorganic semiconductors, the dielectric constant is high. For example, the dielectric constant of Si is 11.9. Therefore, the exciton readily dissociates into an electron and hole. However, in organic semiconductors, the dielectric constant is low; for example, the same for fullerene is 4.4. Therefore, as can be seen in (1.1), a lower dielectric constant leads to a higher attractive force between electron and hole. In contrast to inorganic semiconductors, these excitons cannot dissociate by virtue of thermal energy at ambient temperature and require an electric field to separate. Also, the localisation radius of the exciton is different in Si and organic solar cell. While in Si, the localisation radius is 9 nm, in case of organic semiconductors, it is 0.5 nm. The excitons occurring in inorganic semiconductors are referred to as Wannier excitons while the ones in organic semiconductors are referred to as Frekel excitons [32].

2. The exciton diffuses to the Donor-Acceptor (DA) interface where it experiences an energy level offset between the donor and acceptor phase. This leads to electron and hole experiencing forces in the opposite direction.
3. Exciton dissociates into a charge transfer (CT) complex which then further dissociates into an electron and hole. The dissociation is due to the electric field created by the energy difference between the Lowest Unoccupied Molecular Orbital (LUMO) of the p-type and n-type material. The diffusion length of the exciton is about 10-20 nm. If the domain sizes of the BHJ are not such that the exciton sees an interface within its diffusion length, it recombines via geminate recombination [33].
4. The charge carriers are then carried away to their respective electrodes. The collected electron-hole pair then leads to the flow of an electron in the external circuit.

In order to optimise the steps as mentioned above, strategies such as tailor-making the molecules and copolymers to get desired band gaps and energy levels have been adopted. However, in this work, the focus is on the role of BHJ-morphology on OPV performance.

1. INTRODUCTION

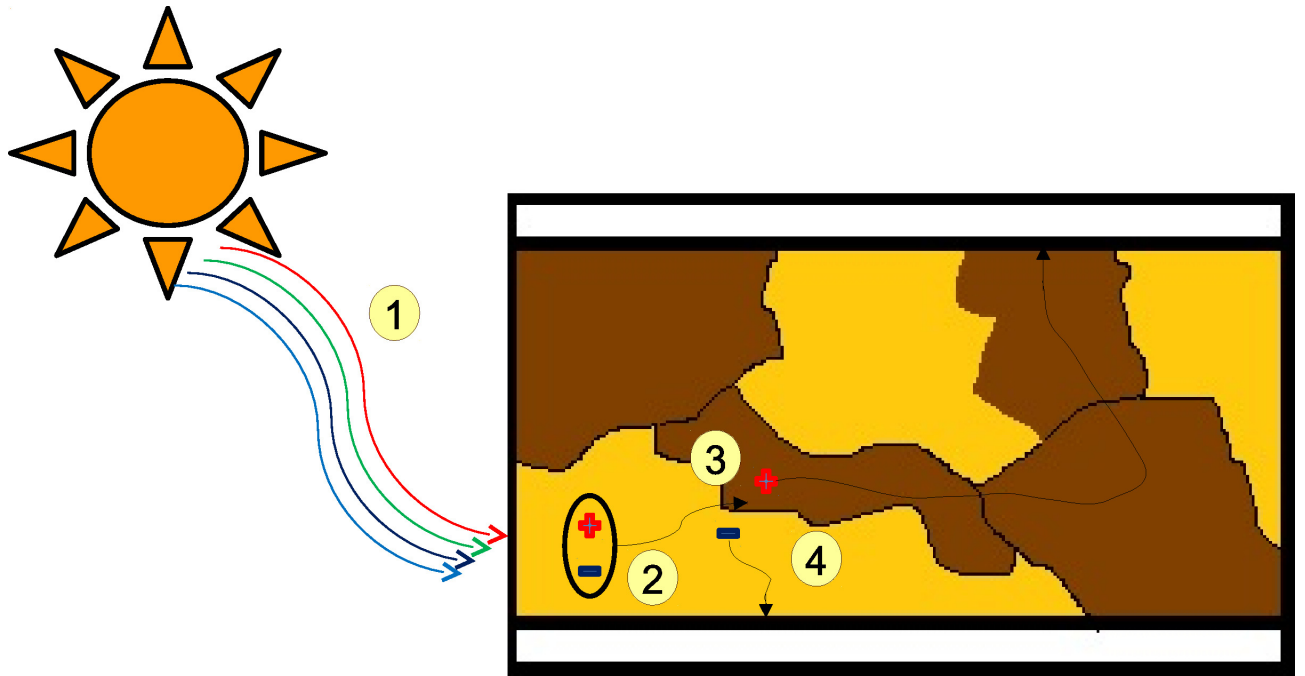


Figure 1.1: Schematic depicting working mechanism of BHJ OPV

1.2.1.1 Morphology Engineering

Having understood the working mechanism in the active layer, the importance of morphology can be better appreciated. As is evident from the charge conduction mechanism of OPVs, the key to an efficient solar cell is the optimisation of morphology (also referred to as morphology engineering) [34]. The point to note here is that there are two important processes involved in the working of OPV, i.e., exciton dissociation and carrier conduction through the morphology to the respective electrodes. Therefore, optimising the morphology in order to maximise exciton dissociation and transportation of the resulting electrons and holes to their respective electrode via a well-connected network of phases with minimal leakage of current and recombination of charge carriers is key to an efficient solar cell.

In the next section, specific essential characteristics of organic solar cell that are used to gauge its electronic performance will be described.

1.3 Essential characteristics of organic solar cells

The schematic of current density vs voltage curve for an organic solar cell is shown in Fig. 1.2. The blue curve corresponds to the J-V curve, whereas the green curve corresponds to the power

1. INTRODUCTION

that can be extracted from the device. The diode equation [35] is as follows:

$$J = J_s \left[\exp \left(\frac{qV}{nk_B T} \right) - 1 \right] \quad (1.2)$$

where, J represents the net-current density; J_s is the reverse saturation current density; q , the elementary charge; V , the external bias; k_B , the Boltzmann constant; T , the temperature; n , the ideality factor.

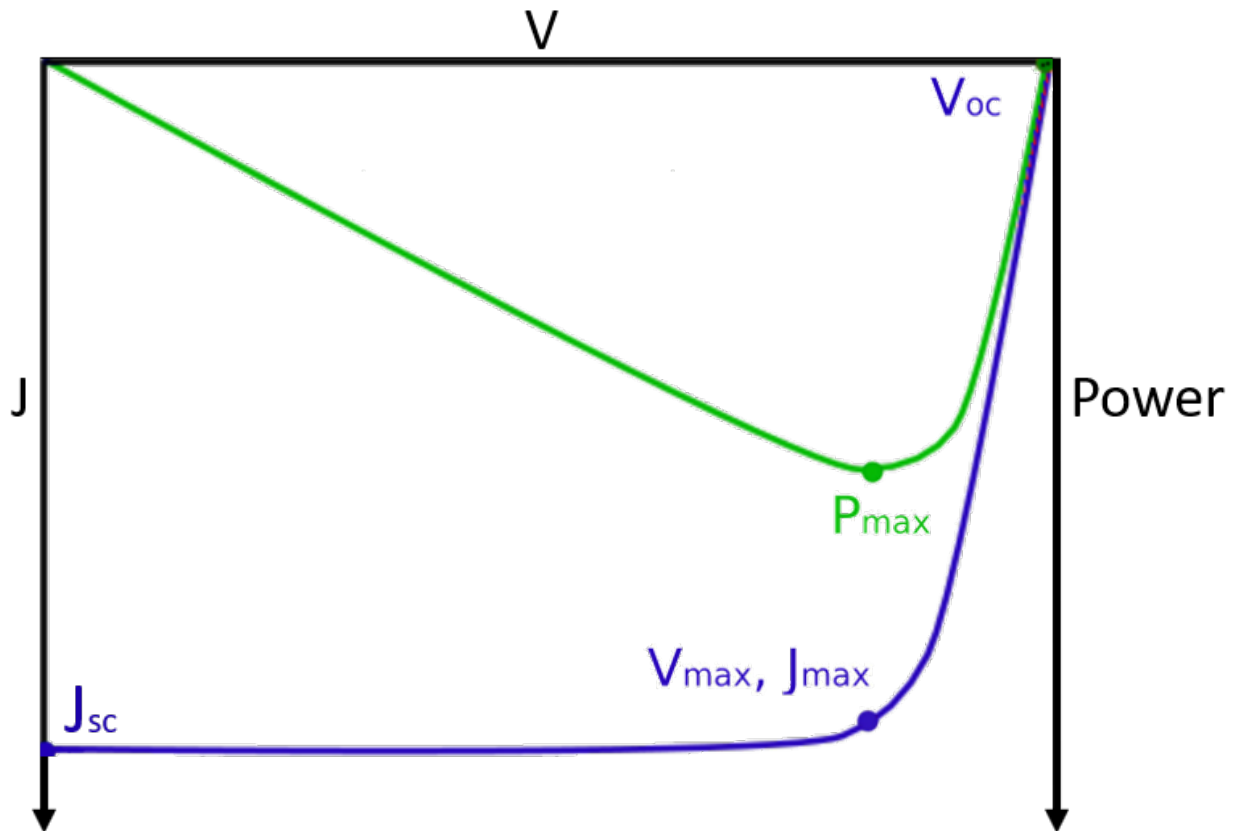


Figure 1.2: Schematic of J-V curve. Blue curve corresponds to the J-V curve whereas green curve corresponds to the power that can be extracted from the device.

- Short-circuit current density (J_{sc}): It represents the net current density of carriers at short-circuit condition, i.e., at no external bias. In other words, it is the effective carrier density due to the intrinsic electric field. J_{sc} is a function of the photoexcitation within the material, charge separation and conduction of carriers to the electrodes. Devices that

1. INTRODUCTION

capture a broader solar spectrum would naturally produce higher J_{sc} . Also, it is the largest current density that the device can exhibit.

- Open-circuit voltage (V_{oc}): It is the maximum voltage difference that can exist across the device and occurs when there is no current flowing through the device. Its magnitude is calculated by the difference in the quasi-fermi level of donor and acceptor phase plus a temperature-dependent quasi-fermi energy level term [36, 37].

$$V_{oc} \approx E_{LUMO}^{acceptor} - E_{HOMO}^{donor} - \frac{k_B}{e} \ln \left(\frac{n_e n_h}{N_c^2} \right) \quad (1.3)$$

where n_e and n_h represent the electron and hole densities respectively; N_c represents the density of states of acceptor LUMO and donor HOMO. For simplicity, the density of states of donor and acceptor have been considered equal.

- Fill-Factor (FF): It is defined as the ratio of maximum power that can be extracted from a device to the maximum ideal power (product of open-circuit voltage and short-circuit current density). Graphically, FF represents the largest rectangle that can be drawn in the J-V curve of a device. Essentially, FF is the measure of how well the separated charge carriers are conducted to the electrodes instead of getting recombined. It is evident that a J-V curve with higher FF would be squarer and therefore, FF is also said to be a representative of squareness of a J-V curve.

$$FF = \frac{P_{max}}{J_{sc} V_{oc}} \quad (1.4)$$

where, $P_{max} = J_{max} V_{max}$.

- Efficiency(η): It is a measure of the performance of the solar cell. It is the ratio of maximum power that can be extracted from the device to the incident solar power. The incident solar power is standardised as AM1.5. AM1.5 corresponds to an illuminance of 1000 W/m² and a solar zenith angle of 48.2°.

$$\eta = \frac{P_{max}}{P_{incident}} 100\% = \frac{J_{sc} V_{oc} FF}{P_{incident}} 100\% \quad (1.5)$$

1. INTRODUCTION

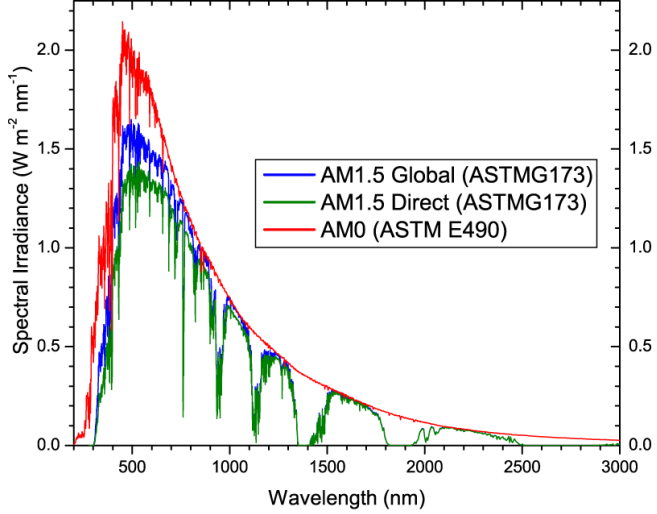


Figure 1.3: Standardised solar spectrum for various Air Mass(AM) cofficients.

- Series resistance (R_s): It is the combined resistance of carrier conduction within the OPV that includes contact resistance between the various layers and the electrode contact resistance. R_s of an OPV device can be gauged by the slope at V_{oc} . Exactly at V_{oc} , there is no effect of series resistance, since no current is flowing through the device, however, as we approach the open-circuit potential and the current begins to flow, R_s comes into the picture. Higher the slope of J-V curve near V_{oc} , lower is the series resistance and higher is the FF. Therefore, R_s strongly influences the FF of an OPV device.
- Shunt resistance (R_{sh}): It gives an estimate of the current leakage in the device and thus leads to reduced power output. The current leakage is attributed to pinholes and carrier traps. Also, if the active layer is not sufficiently thick, electrodes can get short-circuited, thus leading to current leakage paths. R_{sh} of an OPV device can be gauged by the slope at J_{sc} , lower the slope of the J-V curve near J_{sc} , higher is the R_{sh} , better is the device performance. Analogous to R_s , R_{sh} also adversely affects the FF.

In the following section, the bottlenecks and opportunities in OPVs are detailed.

1.4 Bottlenecks and opportunities in OPVs

With OPVs registering a Power Conversion Efficiency (PCE) of 17% [2], the elephant in the room, i.e., the issue of stability still needs to be addressed[38, 39] for commercialisation of organic solar cells. Duan and Uddin [40] provided a comprehensive summary of the factors

1. INTRODUCTION

affecting the stability of OPVs. They have highlighted the effect of photodegradation, thermal degradation at operating conditions, ambient atmosphere degradation, and mechanical instabilities while deploying OPVs on the field. While photodegradation and ambient atmosphere degradation involve chemical processes, the rest of the stability issues can be traced to the morphological instabilities. Multi-component blends have been able to partially resolve the problems of stability while simultaneously offering higher PCEs. It has been seen that the nanomorphology within the active layer has a significant influence on the device stability. This is because, over time, it is observed that the polymer blend demixes resulting in sub-optimal device performance [41]. Therefore, a judicious design of the ternary or higher component such that the intermolecular interactions freeze the nanomorphology is desirable from the stability standpoint. Baran and coworkers [42] demonstrated that the ternary blend comprising P3HT:IDTBR:IDFBR lead to a more stable nanomorphology in comparison to the binary blend containing P3HT:IDTBR. They found that the ternary blend retained >80% of the initial PCE upon 1200 hours of exposure to air under dark conditions, whereas the binary blend retained 70% of the initial PCE. Ternary blends with two acceptors have also demonstrated higher stability when subjected to thermal stress [43, 44]. The enhancement of stability due to favourable intermolecular interactions is not limited to ternary blends. Quaternary OPVs have been reported to have retained 72% of its initial PCE upon 1 year of operation at 65°C. Nam et al. attributed this remarkable efficiency to kinetic trapping that leads to suppression of domain phase separation as well as the domain growth. However, in the case of multi-component blends, the processing parameter space is huge, and device optimisation by experimental trial and error approach is both expensive and time-consuming. Therefore, there is a need for a theoretical approach to investigate the complex Process-Structure-Property (PSP) relationship in OPVs. In this thesis, the process-structure and the structure-property relationship has been established using a diffuse interface method. In the next section, we present a brief introduction of phase-field modeling.

1.5 Phase-field modeling

Phase-field modeling has been an integral part of this thesis. In this work, the phase-field technique has been used for simulating microstructures for various blend systems such as a polymer, fullerene and solvent; one donor and two acceptors. Therefore, a brief introduction of this technique is presented here. Essentially, phase-field modeling is a powerful technique to model microstructural evolution at the mesoscale. The inception of the diffuse-interface approach roots to work done by Van der Waals published in 1894. The work was initially

1. INTRODUCTION

published in Dutch and translated to English by Rowlinson [45, 46]. Van der Waals expressed the free-energy of the system as a function of the local density as well as its spatial derivatives. The mathematical framework for the phase-field model was repropose independently by Cahn and Hilliard [47]. The microstructural evolution entails movement of interfaces that are the boundaries between phases. The diffuse interface modeling approach incorporates a finite thickness of these boundaries provided this thickness is much smaller than the length scale of microstructural features of interest. An order parameter is used to describe the distribution of phases in the system. The order parameter may be any quantity that may be used to differentiate between the phases, such as density, composition, etc. based on the application. In the diffuse-interface approach, the order parameter varies continuously over the interface. This approach is in contrast to the sharp-interface one. The advantage of adopting the diffuse-interface approach for modeling microstructural evolution is that these models are robust as the evolution laws are derived in a thermodynamically consistent fashion and their implementation is typically possible with more straightforward numerical methods than corresponding sharp-interface approaches. This is particularly true for the morphological evolution in the realm of materials science which often involves complex geometries with multiple curvatures that are handled conveniently with the diffuse-interface models. The non-linear equation describing the spatial and temporal evolution of conserved variables like composition is given by Cahn[48] while the evolution of non-conserved variables is given by Allen and Cahn [49]. The phase-field model has been applied to a diverse range of applications such as grain growth and coarsening [50, 51, 52, 53, 54], formation of glasses[55], thin films [56, 57], electrochemistry [58, 59, 60, 61, 62, 63, 64, 65], propagation of cracks [66, 67], damage due to irradiation [68], and electromigration [69, 70, 71, 72]. In order to expedite the theoretical PSP prediction in OPVs, we also used a data-analytics model; a brief introduction about the use of data science in materials science and engineering is given in the next section.

1.6 Materials Data Science

Materials data science, just like data science in other disciplines, involves three basic steps: data management, data analytics and a recently added component to data science, i.e., e-collaboration science. The first component: data management involves storing, archiving, transmitting and retrieving large quantities of data. Specifically, in materials research where experimental conditions and characterisation protocols strongly influence the collected data, these nuances are referred to as metadata. The second component, data analytics involves using the data retrieved through experiments and computational science to extract useful information

1. INTRODUCTION

that can be used for guiding design and optimisation. The data mining is done using Principal Component Analysis (PCA), Machine Learning (ML), regression, etc. The more recent component of data science, i.e., e-collaboration science involves the use of existing platforms for sharing data amongst peers and also for setting-up novel platforms. In essence, the objective of materials data science is to use the extensive database of materials research involving experiments and computational materials science to yield materials knowledge to make better design and optimisation decisions as well as expedite the development of new materials.

Since deriving Process-Structure-Property (PSP) relationship is the core of materials research, materials data science attempts to process the existing database and subsequently develop invertible PSP linkages. In other words, data science tries to use the materials database with information on the effect of processing routes and conditions on the underlying microstructure that in turn influences the property of interest to guide design and optimisation [73].

The beginning of materials data science can be attributed to digitising of the microstructures, extracting simple information such as the average grain size, dislocation density, chemical composition and precipitate size and then correlating these measures to properties of interest [74]. These image processing techniques have been used to guide structure-property linkages as governed by Hall-Petch relationship [75, 76], solid-solution strengthening [77], precipitation hardening [78], slip resistance [79]. However, since the above-mentioned relationships depended on simple morphological measures, only a few structure-property linkages could be established. In order to decipher non-trivial linkages using the microstructure, it is necessary to use advanced data analytics techniques. Therefore, recently, the field of materials data analytics has started to involve scrutinizing the microstructure and then segmenting the microstructural database into groups [80, 81, 82, 83]. These groups are then further analysed to identify features [84, 85, 86, 87]. A more generic and versatile approach in terms of the applicability to a wide range of materials and multiple length scales has been proposed by Kalidindi et al., [3]. They described the microstructure using the n-point spatial correlation maps [3, 4, 5, 6, 7, 88, 89]. The n-point statistics capture the microstructural information, and the amount of information increases with n. However, these statistics are vast and thus, getting useful information directly from them is challenging. Therefore, an effective strategy is to reduce the order of the system by extracting principal components from the statistics known as Principal Component Analysis (PCA) [90, 91, 9, 73, 10, 8, 92]. This exercise of using data science for microstructural quantification, dimensionality reduction and utilising sharing platforms comes under the purview of microstructural informatics [93].

In this work, we have utilised materials data science for building the PSP linkage in ternary OPVs. For a given blend ratio, the microstructure generation and the subsequent

1. INTRODUCTION

electronic property simulation is computationally expensive and takes days to complete on high-performance clusters. This necessitates us to derive a quantitative model using the simulated data to predict electronic properties without the need for running additional simulations for intermediate blend ratios. Thus, in order to create numerical correlations between the processing parameters and microstructure as well as structure and the property of interest, one has to represent the microstructure quantitatively. This mathematical representation of the microstructure is facilitated by using spatial n-point correlation maps of the phases; the simplest of these statistics are the 2-point correlations that are shown in Eq.(1.6) [94].

$$f^{hh'} = \frac{1}{S} \sum_{s=1}^S m_s^h m_{s+r}^{h'} \quad (1.6)$$

where m_s^h represents the volume fraction of local state, h present in spatial cell, s . $f^{hh'}$ denotes the probability of finding local state, h' at spatial vector r from local state h in the microstructure.

The calculation of a 2-point spatial correlating map is performed using discrete Fourier transforms (DFT) [5, 6, 8, 10, 9, 95]. The vectorized 2-point correlation map is further reduced by using Principal Component Analysis (PCA) to concisely capture the features that show maximum variance in the dataset [96, 97, 98, 99]. The principal components are calculated using Eq.(1.7) as,

$$f_r^{(k)} = \sum_{i=1}^{\min((K-1), R)} \alpha_i^{(k)} \varphi_{ir} + \bar{f}_r \quad (1.7)$$

where $\alpha_i^{(k)}$ are the weights of PC for the k^{th} element of ensemble; φ_{ir} represent the orthogonal components; \bar{f}_r is the ensemble average of the statistics.

Chapter 2

Literature review and motivation

In this chapter, a comprehensive review of the literature on topics covered in this thesis is presented. This is followed by the motivation for the work undertaken. Firstly, the literature pertaining to the understanding of morphology in binary OPVs and the modelling techniques that have been used for deciphering the PSP relationship are discussed. Thereafter, we review the literature on state-of-the-art ternary OPVs and data analytics techniques that have been used to design high-performance solar cells. Finally, the literature on evaporation induced phase-separation during spin-coating of OPVs has been surveyed.

2.1 Donor-Acceptor OPVs

OPVs have garnered much interest from the scientific community around the world for sustainable energy[100, 101, 102, 103, 104, 105]. Solution-processed Bulk-Heterojunction (BHJ) Organic Photovoltaics (OPVs) came into being in 1995 offering the advantages of low-cost processing, a higher interfacial area that aids in exciton dissociation and thicker photoactive layer leading to greater absorption of the incident light [31, 106]. OPV fabrication is in contrast to the energy-intensive production of their inorganic counterparts. Therefore, OPVs have the potential for high energy return on investment. Another advantage of organic materials is that they have a high optical absorption coefficient. Therefore thin films can capture sufficient solar energy, thus reducing material cost. However, these advantages are offset by the challenges faced due to low stability [40], low efficiency, and process sensitivity.

In one of the popular methods of device fabrication, i.e., spin-coating, the donor (D) and acceptor (A) are dissolved in a suitable solvent and then spin-coated onto the substrate. During spin-coating, the solvent evaporates resulting in the D-A materials spontaneously phase-

2. LITERATURE REVIEW AND MOTIVATION

transforming. This transformation leads to D and A domains within the active organic-semiconductor layer. The mechanism of phase-transformation is still not clear, some theories support crystallisation to be the cause of phase transformation while others contend spinodal decomposition. In the process-structure modeling framework that we have developed in this work, it has been assumed that spinodal decomposition is the mechanism of phase-transformation given the theoretical and experimental works by several groups [107, 108, 109, 110, 111, 112]. However, some groups have done in-situ studies on drop-cast samples and contend that the mechanism is nucleation and growth [113, 114]. It is important to note that the kinetics of phase-transformation change drastically upon spin-coating, as the thickness of the film reduces to 100 nm from 1 mm (as obtained by drop-casting), moreover, this confinement of the morphology inhibits phenyl-C₆₁-butyric acid methyl ester (PCBM) crystallisation. Therefore, the conclusions drawn from in-situ drop-casting studies about the mechanism of phase-transformation would differ if they were done while spin-coating. Instead of spinodal-decomposition, if crystallisation-induced phase-transformation is assumed, the morphology picture would be different. At low PCBM loadings, P3HT crystallites would form in an amorphous matrix of P3HT and PCBM. Owing to the lack of crystalline phases (and therefore paths for carriers to travel to electrodes), such devices would exhibit lower PCE. Intermediate PCBM loading would result in the formation of three phases: crystalline P3HT, crystalline PCBM and an amorphous phase consisting of intermixed P3HT and PCBM, these devices would exhibit the highest PCE. Higher PCBM loading tends to suppress P3HT crystallinity, and again the PCE would see a setback.

The principal process parameters that influence OPV performance includes the annealing time and temperature, blend ratio of the donor (D) to acceptor (A) material and nature of solvent [115, 116]. Padinger et al. [117] demonstrated that a post-production treatment involving applying an external electric field of magnitude greater than the open-circuit voltage along with thermal treatment on P3HT:PCBM solar cell resulted in higher power conversion efficiency. The higher PCE was achieved owing to the higher shunt resistance and carrier mobility. Li et al., [118] demonstrated the effect of solvent annealing on P3HT:PCBM device performance. They used a petri dish to contain the solvent evaporating from the active layer and thus ended up delaying the rate of film solidification. They found that solvent annealed devices performed better since they had more time for phase-transformation. The slower solidification of active layer resulted in the self-organisation of polymer in the blend. Further, thermal annealing resulted in drying up residual solvent, reduction in free volume and also better contact with electrodes. Yao et al., [115] investigated the effect of solvent mixtures on P3HT:PCBM active layer morphology. They blended P3HT and PCBM in a solvent mixture of 1,8-octanedithiol (OT) and dichlorobenzene (DCB). The devices performed significantly better than the ones

2. LITERATURE REVIEW AND MOTIVATION

prepared by using a single solvent. The improvement was attributed to the following model of phase-transformation proposed by them. During spin-coating, DCB rapidly evaporates, however, since the vapour pressure of OT is 200 times lower than DCB, it tends to stay back longer. Now, the semi-liquid blend consists of P3HT, PCBM and OT. Since PCBM has marginal solubility in OT, it precipitates out and forms its own clusters. Also, since PCBM molecules formed their own clusters, P3HT chains were able to self-organise, resulting in P3HT clusters. Therefore, upon completion of spin-coating, the active layer morphology consists of PCBM clusters and P3HT clusters. This results in a two-fold improvement in device characteristics. Firstly, PCBM forms its own percolating network thus improving electron transport properties instead of forming isolated clusters as in the case of only DCB solvent. Secondly, P3HT has been able to form a percolating network and thus improving hole transport properties.

Till now, the optimisation of OPVs has mostly been done on a trial and error basis. Another way of improving device performance is by a bottom-up approach wherein a theoretical framework is developed to understand the process-structure-property relationship that is then utilised for optimising the device performance. Negi et al., [107] have developed a phase-field model to simulate the microstructure evolution during spin-coating. Several theoretical structure-property models at the microscopic [119, 120, 121, 122, 123, 124, 125, 126, 127, 128, 129] and continuum scale [130, 131, 112, 132, 133, 134, 135, 136, 111] have been developed so far. In some of the models, the active layer or BHJ has been treated as a material having effective electron and hole properties such as mobility and carrier density. The kinetic Monte Carlo (kMC) method has been implemented by various groups [119, 137, 123, 124, 125, 127, 128, 138] for deriving structure-property correlations. In continuum models, Barker et al., [130] were the first ones to develop a numerical model to calculate the current-voltage characteristics for a bilayer all-polymer solar cell and were able to explain specific experimental trends and identify few design rules for OPVs. Their model incorporated various important phenomena occurring in solar cells such as drift, diffusion, injection and extraction of carriers at the cathode and the anode as well as space charge effects. Their model explained the linear relationship between photocurrent and intensity by considering that the bound polarons dissociate at the interface producing charge carriers. They were also able to explain how open-circuit voltage has a logarithmic dependence on light intensity. A quantitative model to simulate the current-voltage characteristics for polymer-fullerene BHJ solar cells considering the active layer to be comprised of a semiconductor having LUMO of acceptor as valence band edge and HOMO of the donor as conduction band edge was developed by Koster et al. [131]. Their model also incorporated drift, diffusion, space charge effects, bimolecular recombination as well as the effect of temperature on carrier generation. They compared the theoretical results with exper-

2. LITERATURE REVIEW AND MOTIVATION

imental data obtained for OC₁C₁₀-PPV:PCBM solar cell for a weight ratio 1:4. Using their model, they suggested two improvements that could significantly improve device performance. Firstly, increasing the polymer hole mobility (OC₁C₁₀-PPV) to match that of fullerene electron mobility. The unmatched electron and hole mobility result leads to obstruction for the holes to escape, and the accumulation of holes aids in bimolecular recombination. Secondly, modification of PCBM LUMO to 3.3 eV instead of the present value, i.e., 3.8 eV. Since, V_{oc} is a function of the HOMO-LUMO difference of donor and acceptor as described in the introduction (1.3), the change in LUMO of PCBM would reflect as higher V_{oc} and thus improved efficiency. They predicted that these two modifications would increase the power conversion efficiency to 5.5% from 2.5%. Buxton and Clarke [112] predicted structure-property correlation for diblock copolymer morphology using a two-dimensional model. Their model for the first time accounted for exciton diffusion and dissociation in BHJ morphology, and additionally the authors simulated the active layer microstructures using Cahn-Hilliard formulation with the polymer-free energy modeled by Flory-Huggins equation. The effect of surface-induced ordering, as well as electric-field-induced alignment on the device characteristics of BHJ morphology, was also investigated by them. Further, the optimisation of the device thickness and interfacial area for optimal device performance was done by Martin et al., [132] by solving the drift-diffusion model for a nanostructured-heterojunction. They examined the effect of recombination, light intensity and anode barrier height on the J-V characteristics and attributed the improvement in device performance due to the addition of Li[CF₃SO₂]₂N to the improvement in donor hole mobility. A two-dimensional optical and electrical model was formulated by Williams and Walker [133] for simulating the electrical characteristics of an interdigitated morphology. The BHJ morphology of all-polymer solar cell was simplified to an interdigitated one, and the length of interdigitated fingers was varied in their simulation. The formation of charge-transfer (CT) state while the exciton dissociates was also incorporated in the model. Kirchartz et al., [134] developed a one-dimensional electro-optical model for BHJ solar cells considering the active layer to be homogeneous material. They employed a commercial device simulation software - Advanced Semiconductor Analysis (ASA) developed by TU Delft [139]. The structure-property relationship for two-dimensional rod-coil block copolymers was determined by Shah and Ganesan [135]. They developed a self-consistent field theory (SCFT) model for generating rod-coil block copolymer morphologies. The anisotropy in charge transport, i.e., preferential intrachain carrier conduction in comparison to interchain (or hopping) conduction was also modeled by them. This was done by using the anisotropic hole and exciton mobility tensors. The effect of domain size and orientation, the extent of phase-separation on device performance was investigated in their work. Holst et al., [140] modeled the single-carrier cur-

2. LITERATURE REVIEW AND MOTIVATION

rent density in three-dimensional sandwich-type organic semiconductor devices. The effect of blend stoichiometry, carrier density, electric field, and disorder on charge transport in organic blends was explored by Koster [141] by solving the Pauli master equation [142]. Ray et al., [111] applied the model developed by Buxton and Clarke [112] to simulate the effect of annealing temperature and duration on the device performance for one particular blend ratio of donor and acceptor (1:1 wt ratio). They solved the drift-diffusion equation by finite difference method using the Scharfetter–Gummel’s discretization [143] and assumed a constant electric-field within the active layer. The carrier transport equations were solved only in percolating domains, and isolated domains were not accounted for in the simulations. The basis of this assumption is that only the percolating domains would contribute to device characteristics. Their model was able to answer some open questions in the OPV community such as the peak observed experimentally in J_{sc} while annealing, invariability of V_{oc} to annealing duration. Kodali and Ganapathysubramanian, [144] extended the formulation developed by Buxton and Clarke [145] and implemented a new formulation involving a transformation of variables for computing the net current density. They used the Finite Element Method for simulating device characteristics for 2D and 3D BHJ morphologies.

The above-mentioned models are sharp-interface ones, and they have certain shortcomings. Firstly, in order to solve for the electrostatic and electron, hole density fields across a one-dimensional heterogeneous junction consisting of two-phases, the Poisson’s equation and mass conservation equation are solved in a coupled manner in each of the bulk phases, while at the interface between the two phases, the continuity of electrostatic potential as well as the continuity of the fluxes is imposed, with which the steady-state electron-hole density profiles as well as the electrostatic potential field across the interfaces is derived. The complexity of this model increases as the Bulk-hetero-junction assumes complicated geometries as now the imposition of continuity of normal fluxes across the interface between a donor and acceptor domain requires the description of the shape of the interface. Secondly, since the thickness of active-layer is typically 100 nm which is about the same as that of the depletion width which is 60 nm [146], we can expect near-complete depletion, and thereby the concentration of carriers is low. This makes the mass conservation equation numerically stiff, requiring complex solution routines and possible refinement of meshes near regions of rapid concentration changes near the interface and in particular when the morphology comes in contact with the electrodes. In order to deal with complex morphologies and low concentration of carriers as is typical in organic-semiconductors (OS), we adopt the diffuse interface model, where we create a mathematically smeared interface of a fixed finite width, replacing the sharp-interface between the domains. Additionally, we transform the mass-conservation equation into an equation for the effective

2. LITERATURE REVIEW AND MOTIVATION

diffusion potential as we will see below. The additional requirement of refinement of meshes at interfaces is avoided in the diffuse-interface model by firstly resolving the interface with a sufficient number of points (10 in our case) and secondly, we solve for the diffusion potential, whose variation is orders of magnitude lesser than the corresponding concentration variations across interfaces. Therefore, this model does not specifically require variable mesh density at the interfaces. The formulation of this model is described in Chapter 4, and its application to Donor-Acceptor OPVs is detailed in Chapter 5.

2.2 Donor-Acceptor-Acceptor (DAA) OPVs

The first two decades of research in OPVs focussed on binary solar cells[37]. However, since they have limited absorption of the solar spectrum, the interest shifted to increasing the bandwidth of absorption [147]. The foray of tandem and ternary organic solar cells have resolved this problem of limited absorption bandwidth[42, 148, 149, 150, 151, 152]. Tandem solar cells are stacks of solar cells with complementary absorption spectrum. In this regard, ternary OPVs hold a higher potential as in addition to capturing a broader solar spectrum, they are also easier to fabricate, in contrast to their tandem counterpart [153]. Ternary OPVs have already achieved a Power Conversion Efficiency (PCE) of 17% [2]. The ternary BHJ comprised of PBDB-T-2F as the polymer donor, Y6 as the non-fullerene acceptor, and PC₇₁BM as the fullerene acceptor. Lin et al., [2] utilised transition metal disulfides as the hole-transport layer owing to their excellent uniformity upon deposition on ITO. The device architecture of their champion devices was ITO/MX₂/active-layer/PFN-Br/Al. The device exhibited 78% FF, 0.84V V_{oc} , 26 mA cm⁻² J_{sc} and PCE of 17%. This high efficiency has been possible since ternary OPVs have been able to simultaneously improve the photovoltaic parameters, i.e., short-circuit current density (J_{sc}), open-circuit potential (V_{oc}) and fill-factor (FF) [154, 155]. The simultaneous improvement in device characteristics is because firstly, owing to the broader capture of the solar spectrum; ternary OPVs naturally produce higher J_{sc} . Secondly, by making a cascade energy alignment, it has been possible to tune the open-circuit potential V_{oc} [156, 157]. In ternary OPVs, V_{oc} can be modified by ≈ 100 mV. This modification stems from the change in charge transfer complex state. It has been found that the change can be attributed to compositional and morphological effects. Thirdly, the issue of charge recombination and transport that has been plaguing OPVs gets resolved to an extent by the addition of the ternary component[158].

While ternary organic solar cells indeed provide a viable solution for increasing efficiencies, it is, however, important to control the structure of the bulk-hetero-junction(BHJs) which is the active layer of the solar cell. In this context, determination of Process–Structure–Property(PSP)

2. LITERATURE REVIEW AND MOTIVATION

correlations are important, that relate not only the composition and the fabrication process parameters to the structure of the BHJ, but also the corresponding electronic properties through structure–property correlations. The PSP relationships are however non-trivial as even in binary OPVs the parameter space is large [130, 131, 112, 132, 133, 134, 135, 140, 141, 111, 144] and adding another component further complicates this relationship[159]. A recent comprehensive review by Gasparini et al. [41] emphasised the effect of nanomorphology on device performance and described the nanomorphology models that govern their performance. The nanomorphologies in ternary OPVs are classified into the parallel-like model and alloy model. In the parallel-like model, the addition of the ternary component leads to the formation of two independent solar cells and the device performs similar to the tandem architecture. In the case of the alloy model, the resultant energy level of donor and acceptor materials behave as an electronic alloy. Since in real practical situations, the alloy and parallel-like nanomorphologies coexist, it becomes difficult to predict the photovoltaic response of a given active layer. Therefore, the effect of processing parameters on this resultant nanomorphology and its subsequent mapping to device performance remains elusive, particularly for experimental design. In this context, the utilization of theoretical models for deriving both the process–structure and the structure–property correlations become useful. Kipp et al.,[160] used a theoretical framework for optimizing ternary OPVs based on block-copolymer as the ternary component where they employed Single Chain in Mean Field (SCMF) simulations to explore various morphologies that arise for a system of polymer, fullerene and block-copolymer. Further, the authors utilized the kinetic Monte Carlo (KMC) method for predicting the efficiency of the simulated microstructures. In particular, the variation of the efficiency, short-circuit current, open-circuit potential and fill factor are related to simple geometrically motivated microstructural descriptors, and thereby optimal volume fractions are derived. It must be noted, that while a finite number of morphological descriptors maybe utilized to parameterize and correlate with the performance it is never possible to determine the complete set of descriptors for a given microstructure, and thereby the relation between the microstructure and the property may remain incomplete.

In this spirit of deriving complete PSP correlations, Wodo et al. [161], used the MapReduce paradigm to map the effect of processing conditions (such as interaction parameter, annealing time and blend ratio) to the microstructures. Further, using descriptors (such as domain fraction that absorbs the incident light, average distance between donor and donor-acceptor interface, tortuosity of the domains) the microstructures are classified into clusters, the microstructures within a cluster are then reduced to render a representative microstructure which is then mapped to the photovoltaic properties. Pokuri et al., [159] explored a data science approach to map the complex as well as the computationally expensive relationship between

2. LITERATURE REVIEW AND MOTIVATION

microstructure and J_{sc} in binary OPVs. Here, the authors have simulated morphologies using the Cahn-Hilliard approach for different binary blend compositions. The electronic properties of the simulated morphologies are derived by solving the drift-diffusion equations for holes and the electron, resulting in the determination of the photovoltaic parameters. Thereafter, the authors have utilised deep convolutional neural networks (CNN) to establish the structure-property relationship. However, since the data set required for establishing generalisable and interpretable neural networks is vast, they have considered only 2D microstructures of the binary system. Establishing CNN for three-phase 3D microstructures is computationally intensive, and there is a need to adopt dimensionality reduction techniques to attack the PSP correlation challenge in OPVs.

This sets the motivation for work done in Chapter 6, where we aim to determine the PSP linkages in ternary blends where the process-structure and structure–property correlations will be utilized for determining optimal compositions and microstructures. The system considered for this study consists of a polymer donor, fullerene acceptor and small molecule acceptor (abbreviated as DAA). For this system, we have spanned a generous portion of the three-phase space in the simplex for determining the range of morphologies, where we have utilized a formulation based on the Cahn–Hilliard theory, using the Flory Huggins free-energy density generalized for a ternary blend. For each of these simulated microstructures, we have applied the diffuse interface structure–property model to evaluate J-V characteristics.

For deriving the PSP linkages, we have first determined the statistics corresponding to the microstructures, where we have utilised spatial 2-point correlation maps of the phases to represent the microstructure mathematically. The vectorised 2-point correlation map is further reduced by using Principal Component Analysis (PCA) to concisely capture the features that show maximum variance in the dataset [96, 97, 98, 99]. Thereafter, the variation of the principal components (PCs) with composition as well as the properties are utilized for the determination of PSP linkages. As a result, we present a data analytics approach for deriving both the microstructures as well as the blend compositions that result in optimal efficiency.

2.3 Evaporation induced phase-separation during spin-coating

One of the primary reasons for the popularity of this third-generation solar technology has been their ease of fabrication [162, 163]. The organic semiconductor thin film referred to as the active layer can be deposited on the substrate by using a variety of coating and print-

2. LITERATURE REVIEW AND MOTIVATION

ing techniques [164]. While some of these techniques such as casting, spin-coating and ink-jet printing are commonly used at the lab-scale, others such as slot-die coating, gravure coating, spray coating and flexographic printing are roll-to-roll techniques and are used for large-scale production [165, 129]. Central to these various techniques is the evaporation of solvent during processing which in turn influences the active layer microstructure, and the resultant morphology strongly affects the device performance [166, 34, 167]. Therefore, it becomes imperative to understand the thermodynamics and kinetics of the morphology formation and then tailor it to optimise the device performance [168, 169].

In order to unravel the process-structure relationship in OPVs, several process-structure models [109, 170, 171, 172, 173, 174, 175] have been developed. In order to understand the effect of processing conditions such as evaporation rate of solvent, blend ratio, degree of polymerisation, substrate patterning on the final microstructure, Wodo and Ganapathysubramanian [109] formulated a 3D computational framework. Since evaporation-induced phase separation is a moving boundary problem, the authors used coordinate transformation to incorporate the changing domain size at every time iteration without needing to remesh repeatedly. Finite element method (FEM) was employed to solve the Cahn-Hilliard equations with the imposed solvent flux at the top boundary. Negi et al. [107], further augmented the simulation results using experimentally determined kinetic parameters and predicted the region of initiation and length-scale of phase-separation [107].

Pfeifer et al., [176] established PSP correlation in ternary OPVs using a 2D model. The authors simulated the effect of solvent evaporation rate and substrate patterning wavelength on the microstructure. The structure-property relationship was mapped using an approximate graph-based simulator using Bayesian optimisation. This optimisation routine relies on certain morphological traits such as light absorption efficiency of donor material, exciton dissociation efficiency of morphology and charge transport efficiency for predicting the short-circuit current density (J_{sc}). However, since the authors do not solve the drift-diffusion equation for calculating photovoltaic performance and these descriptors capture only some features of the complex BHJ morphology, the results are approximate.

In the spirit of completing the PSP relationship in 3D ternary OPVs involving polymer, fullerene and solvent, we have adopted a process-structure framework based on the Cahn-Hilliard theory, along with Flory-Huggins bulk free energy density to model the polymer blend free energy. The effect of two critical processing parameters, i.e., evaporation rate and blend ratio on the microstructure and subsequently on device performance has been explored in Chapter 7.

Chapter 3

Experimentation

In this chapter, the experimental protocol for OPV fabrication is described. A concise description of the fabrication techniques that have been used in this work is also presented. We performed experiments on binary and ternary OPVs in order to understand the effect of blend ratio and annealing time on device characteristics that set up the motivation for the modeling and simulation work that is described in the subsequent chapters. Further, we mention various techniques for OPV characterisation.

3.1 Experimental protocol

In this section, the fabrication protocol for organic solar cells is described. Since OPVs are multi-layer structures, the fabrication involves a series of steps to deposit each layer. We first mention the significance of each layer and the material that has been used for the same. Thereafter, the sequence of device fabrication is detailed. Finally, the characterisation techniques that have been used in this thesis are mentioned.

3.1.1 Materials used

The OPVs are multi-layer devices comprising of several materials such as the substrate, electrodes, hole transport layer, electron transport layer and the active layer consisting of the organic semiconductors.

3.1.1.1 Substrate and top-contact electrode

In all the experiments, ITO coated glass substrates have been used wherein ITO serves as the top-contact electrode for OPV device. The thickness of ITO films sputtered over a glass

3. EXPERIMENTATION

substrate is \approx 15-30 nm. The films have a sheet resistance of 20-30 Ω/sq . The purpose of the glass substrate is to provide mechanical stability and transparency. These substrates have been procured from Delta Technologies.

3.1.1.2 Hole Transport Layer (HTL)

HTL is used to selectively allow the conduction of holes and block electron conduction to the ITO electrode, thus reducing carrier recombination, which is reflected in the shunt resistance of the OPV device. In the case of binary devices, PEDOT:PSS was used as the HTL since it offers several advantages such as solution processability, transparency, high conductivity and smooth surface [177]. In this work CLEVIOS Al 4083 grade of PEDOT:PSS was used that had been procured from Heraeus. In the case of ternary OPVs, MoO₃ was used as the HTL.

3.1.1.3 Active layer

In this work, several donors and acceptors have been used for preparing the active layer corresponding to binary and ternary OPVs. For binary OPVs, we used P3HT as the donor and PC₆₀BM as the acceptor. P3HT was procured from Rieke metals (4002-EE) having a molecular weight of 52 kg/mol, polydispersity 2.4, and regio-regularity 91% while PC₆₀BM was procured from Nano-C. In order to fabricate ternary OPVs, PTB7-Th and COi8DFIC were purchased from Merck while PC₇₀BM was obtained from Nano-C. Donor-Acceptor-Acceptor ternary blends comprised PTB7-Th:COi8DFIC:PC₇₀BM.

3.1.1.4 Electron Transport Layer (ETL)

Analogous to HTL, ETL is used to selectively allow electron conduction and block hole conduction to the electron extracting electrode. In the case of binary OPVs, ETL was not used whereas for ternary OPVs, ZnO was used as the ETL. The ZnO precursor solution is prepared by mixing 1 part of diethyl zinc (DEZ) and 7 parts of tetrahydrofuran (THF) that were procured from Merck.

3.1.1.5 Bottom-contact electrode

We have used aluminium as the bottom-contact electrode for binary devices and silver for ternary devices.

3. EXPERIMENTATION

3.1.2 Device fabrication protocol

All the essential steps involved in fabricating organic photovoltaic devices are listed here in sequential order.

3.1.2.1 Solution preparation

Solution preparation is done one day prior to device fabrication. 500 μL of the solution is sufficient to prepare 3 devices. So, the blend is weighed accordingly. While optimising the fabrication protocol, around 4 devices are prepared to avoid wastage. For the binary blends, firstly P3HT is weighed since it is in the form of flakes and its weight is difficult to control. Then PC₆₀BM is weighed since it is in powdered form and its weight is easier to control and thus get the desired P3HT:PCBM ratio. The blend is then mixed with chlorobenzene, and the solution is stirred overnight (≈ 12 hrs). The concentration of the solution is always measured with respect to the polymer. This is because the polymer is more viscous, and thus its concentration governs the thickness of the spin-coated film. In the case of the ternary blends, all the components are weighed separately and then dissolved in chlorobenzene. The solutions containing the individual components are then stirred overnight (≈ 12 hrs). Post this, the blends are then mixed, and 1,8-diiodooctane (DIO) is added. The ternary blend with added surfactant DIO is then stirred for further 3 hrs. The DAA ternary blend used in this work corresponds to PTB7-Th, COi8DFIC and PC₇₀BM.

3.1.2.2 Substrate cleaning and treatment

The ITO-coated glass-substrates are numbered on the backside for reference. The substrates are ultrasonicated in soap water for 10 mins. After ultrasonication, the beaker and substrates are thoroughly washed with DI water to remove any left-over soap. Thereafter, the substrates are ultrasonicated in DI water, acetone, and isopropyl alcohol (IPA) for 10 mins respectively. The substrates are then dried using compressed air and kept in an oven maintained at 60°C overnight for evaporating the solvent. Post the drying, the substrates are UV-Ozone treated for 20 mins to improve their wettability.

3.1.2.3 Deposition of the transport layers

The ETL and HTL are then deposited onto the ITO coated glass substrate based on the device architecture. In the case of conventional device architecture, HTL is coated first, whereas, in the case of the inverted device architecture, ETL is coated first. For fabricating binary OPVs,

3. EXPERIMENTATION

we used conventional architecture and thus spin-coated 40 nm of PEDOT:PSS on the substrates whereas for ternary OPVs, we adopted inverted device architecture and spin-coated 30 nm of ZnO. Additionally, in ternary devices, 5 nm of MoO₃ HTL is thermally evaporated at $\leq 0.1 \text{ \AA/s}$ in $5.0 \cdot 10^{-6} \text{ mbar}$ vacuum.

3.1.2.4 Spin-coating the active layer

In order to spin-coat the active layer on top of the transport layer, 150 μL of the polymer blend is pipetted out and poured uniformly over the substrate starting from the centre. The spin-coating rpm is chosen according to the desired thickness of the film, with the film thickness being inversely proportional to spin-coating rpm. Post the deposition of active-layer, three sides of the film are scraped off using a blade resulting in two sides having just the ITO padding over which top-contact electrode is thermally evaporated whereas one side, either top or bottom, is meant for ITO contact (Fig.3.1).

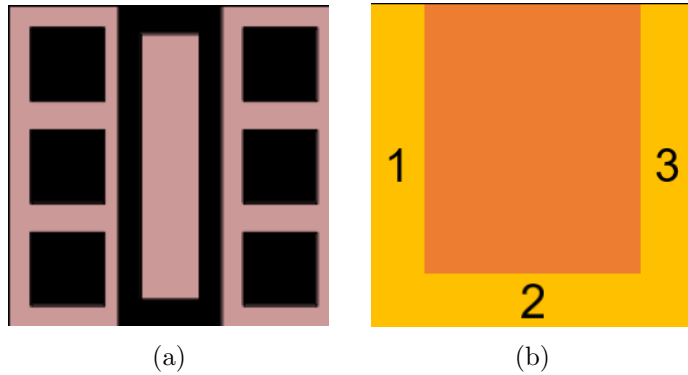


Figure 3.1: (a) Substrate with ITO coating shown in black and glass in pink. (b) Spin-coated substrate with three sides of the film scraped off, the active layer is depicted by orange color and the scraped off region by yellow color.

3.1.2.5 Evaporation of bottom-contact electrode

Prior to thermal evaporation, aluminium wire is placed in a tungsten coil. Thereafter, the coil is loaded in the evaporator chamber and then the turbopump is turned ON to generate vacuum. Once the vacuum reaches $\approx 5.0 \cdot 10^{-6} \text{ mbar}$, evaporation is started. On the film menu of the thermal evaporator GUI, appropriate material parameters are chosen, for example, density = 2.7 gm/cc and z-factor = 1.08. The power of thermal evaporator is increased in steps of 2% every 1.5 mins until power reaches 12%. Up to 30nm of aluminium deposition, the evaporation rate is maintained at $\leq 0.5 \text{ \AA/s}$ in order to prevent shorting of the active layer by the electrode.

3. EXPERIMENTATION

After 30nm of aluminium film has been deposited, the evaporation rate is increased to 1.5 Å/s. Once 100 nm of the aluminium film has been evaporated, the thermal evaporator power is brought down to zero. Figure 3.2 shows the six pixels prepared on one substrate.

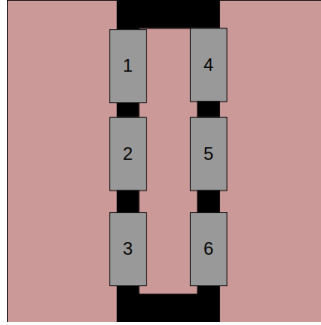


Figure 3.2: Six device pixels represented by the overlap between top-contact and bottom-contact electrode.

3.2 OPV characterisation

OPV devices are characterised for their opto-electronic properties, morphology and film thickness. A brief discussion of various characterisation techniques is provided in this section.

3.2.1 J-V characteristics

As soon as the device is fabricated, J-V characteristics of the device are determined by performing a voltage sweep and then observing the current density under both dark and light conditions. For examining the photovoltaic parameters, the voltage sweep is performed under a broadband illumination source (Sol3A Class AAA solar simulator manufactured by Newport) using a solar simulator that reproduces the AM1.5 solar spectrum. In this work, Keithley 4200 parametric analyzer has been used for the J-V characterisation. Prior to the characterisation, the broadband light source is calibrated using a standard silicon solar cell to the desired illumination intensity. Since in the dark, the solar cell behaves like a diode, the semi-log dark J-V characteristics (J plotted in log) provide useful information about ideality factor, series and shunt resistance.

3.2.2 Stylus profilometer

Stylus profilometers are used to measure the thickness of deposited layer on the substrate. Its working principle involves seaming a diamond stylus probe mechanically along a surface with

3. EXPERIMENTATION

a particular torque referred to as the setpoint. The movement of the probe is controlled by a feedback loop that ensures that the probe moves in z-direction such that the torque on the probe is maintained at the setpoint. We use Dektak XT stylus profilometer (contact-based profilometer having nm vertical resolution) with a tip size of 2 μm along with Vision 64 GUI (capable of 64-bit parallel processing). In order to measure film thickness, few scratches are made on the film using a blade, hills and valleys mode is selected using a Graphics User Interface (GUI) where the stylus tip size, force and scan rate are specified. The force selection is based on the surface rigidity of the film, where, for an active layer thickness, we typically use 3 mg force.

3.2.3 Atomic Force Microscope (AFM)

AFM works on the principle of Van der Waals force between the tip and the sample. The forces enable a 3D reconstruction of the sample topography amongst other measurements such as conductivity, phase-contrast, mechanical properties of biological samples by the use of appropriate tips. AFM works in three imaging modes: contact, non-contact and tapping.

In this work, the samples have been imaged using tapping mode. This mode is typically used for samples that are soft or not strongly bound to the substrate. Tapping mode involves intermittent tapping of the tip on the sample with the cantilever oscillated by a piezoelectric crystal at its resonant frequency of \approx 50,000 to 500,000 cycles per second with an amplitude of 20 nm. There is a feedback loop that ensures that the cantilever's oscillation amplitude is maintained and this, in turn, renders the surface features of the sample. For example, if there is a depression on the sample surface, the tip gets more room to oscillate thus increasing the oscillation amplitude, however, if there is a bulge in the sample, the tip gets crammed for room to oscillate, thus reducing the tip oscillation amplitude. This change in the oscillation amplitude is fed back to the controller, which in turn renders the topography of the sample. A laser detection system measures the tip deflection wherein the laser is incident on the flat, reflecting surface of the cantilever just above the tip. Upon reflection, the laser falls on the Position Sensitive Photo Diode (PSPD) that tracks the direction of cantilever motion. The phase-contrast imaging that is done in conjunction with tapping mode measures the phase lag between the oscillation signal sent to the cantilever and the actual oscillation in different phases.

In contact mode, the tip interacts with the sample surface in the repulsive force regime with forces of the order of nN . In this mode, the tip is maintained at a particular deflection; the change in this deflection due to surface features is imaged. To maintain the desired deflection, force is applied by the piezoelectric driver calculated using Hooke's law.

3. EXPERIMENTATION

In contrast to the contact mode, the non-contact method works in the attractive regime of sample-tip interaction. The attractive forces are long-ranged and include magnetic, electrostatic and capillary forces. This mode of imaging minimises the damage to the tip and sample.

3.2.4 Scanning Transmission X-ray Microscopy (STXM)

STXM is a technique to measure the x-ray intensity transmitted through the sample. This measurement can be done with respect to spatial coordinates or energy. When both the energy and spatial information is measured together, it is referred to as a stack. The transmitted signal is further processed to Optical Density (OD) in order to render information about the thickness, composition and density, the following equation is utilized,

$$OD = \ln \left(\frac{I_0}{I} \right) = \mu dt, \quad (3.1)$$

where I_0 is the incident x-ray flux; I is the transmitted x-ray flux; μ is the mass absorption coefficient; d is mass density and t is the thickness.

In order to process a stack, the first step is to load the stack in an image processing software, Analysis of X-ray Images and Spectra (aXis 2000). Once the stack is loaded, it is processed into a non-compiled browse (ncb) file. Thereafter, the stack is aligned using Jacobsen or Zimba method [178]. The next step is to find the incident X-ray flux, I_0 either by identifying a clear region in the stack or by extracting it using the histogram. Another method of obtaining I_0 is to use a previously used I_0 in the current analysis. Finally, the image is converted to OD and then analysed.

3.3 Binary OPVs

We have chosen P3HT:PCBM as the active layer for fabricating binary OPVs. The fabricated device architecture is ITO/PEDOT:PSS/ P3HT:PCBM/Al (see Fig. 3.3(a)). The devices have an active area of 6 mm². The device fabrication procedure is as follows: ITO-coated glass substrates are sonicated in soap water, DI water, acetone and then IPA for 10 min respectively. They are dried using compressed air and then treated by UV-ozone for 20 min. Immediately after the UV-ozone treatment, PEDOT:PSS is spin-coated at 4500 rpm for 1 min and then annealed at 150°C for 30 min. After that, the substrates are transferred to JACOMEX nitrogen glove-box, and the active layer is spin-coated at 1100 rpm for 1 min. P3HT obtained from Rieke

3. EXPERIMENTATION

metals (4002-EE) has a molecular weight of 52 kg/mol, polydispersity 2.4, and regio-regularity 91%. It is dissolved with PCBM (from Nano-C) at 60°C overnight in chlorobenzene (CB). The polymer concentration is 10 mg/ml. The substrates are then thermally annealed at 150°C for 10 min. 100 nm of Aluminum is evaporated at approx 1.5 Å/s using Angstrom engineering thermal evaporator. The devices are then characterised using a solar simulator. The effect of blend ratio on device efficiency is depicted in Fig. 3.3(c) wherein the lines have been drawn just to follow the points and have no physical significance. As can be seen, the maximum efficiency is obtained at 57 weight % of P3HT. It is also observed that J_{sc} achieves a maximum at a specified time during the post-annealing treatment at 150 °C, and beyond that, the J_{sc} decreases.

We also characterised the morphology of the active layer for 1:0.8 blend ratio of P3HT:PCBM using Fluid-AFM as shown in Figure 3.4.

3.4 Ternary OPVs

Experiments were done for Donor-Acceptor-Acceptor (DAA) ternary blend system comprising PTB7-Th, COi8DFIC, and PC₇₀BM. The fabricated device architecture is ITO/ZnO/active-layer/MoO_x/Ag (see Fig. 3.5(a)). The devices have an active area of 10 mm². The device fabrication procedure is as follows: ITO-coated glass substrates are sonicated in soap water, DI water, acetone and then IPA for 10 min respectively. They are dried using compressed air and then treated by UV-ozone for 20 min. The ZnO precursor solution is prepared by mixing 1 part of diethyl zinc (DEZ) and 7 parts of tetrahydrofuran (THF). Immediately after the UV-ozone treatment, freshly prepared ZnO is spin-coated at 5000 rpm for 1 min in the ambient atmosphere. After that, the substrates are transferred to the JACOMEX nitrogen glove-box. The substrates are then annealed at 120°C for 15 min. The ternary components are dissolved at 60°C overnight in chlorobenzene (CB). The polymer concentration for DAA blend is 7.2 mg/ml. 1% (volume fraction) DIO was added to the DAA blend. The DAA active layer is spin-coated at 1500 rpm for 60 secs. 5 nm of MoO_x and 100 nm of Ag are then sequentially thermally evaporated using Angstrom engineering thermal evaporator at a vacuum level of 5.0 10⁻⁶ mbar. The devices are then characterized using a solar simulator. The effect of ternary component's weight ratio on device efficiency for DAA blend is depicted in Fig. 3.5(c) wherein the lines have been drawn just to follow the points and have no physical significance.

We attempted to characterise the underlying BHJ morphology of the ternary blend using STXM, however since the domains were smaller than 30 nm (the resolution of STXM), we could not observe the microstructural features. The morphology for PTB7-Th:PC₇₀BM binary blend

3. EXPERIMENTATION

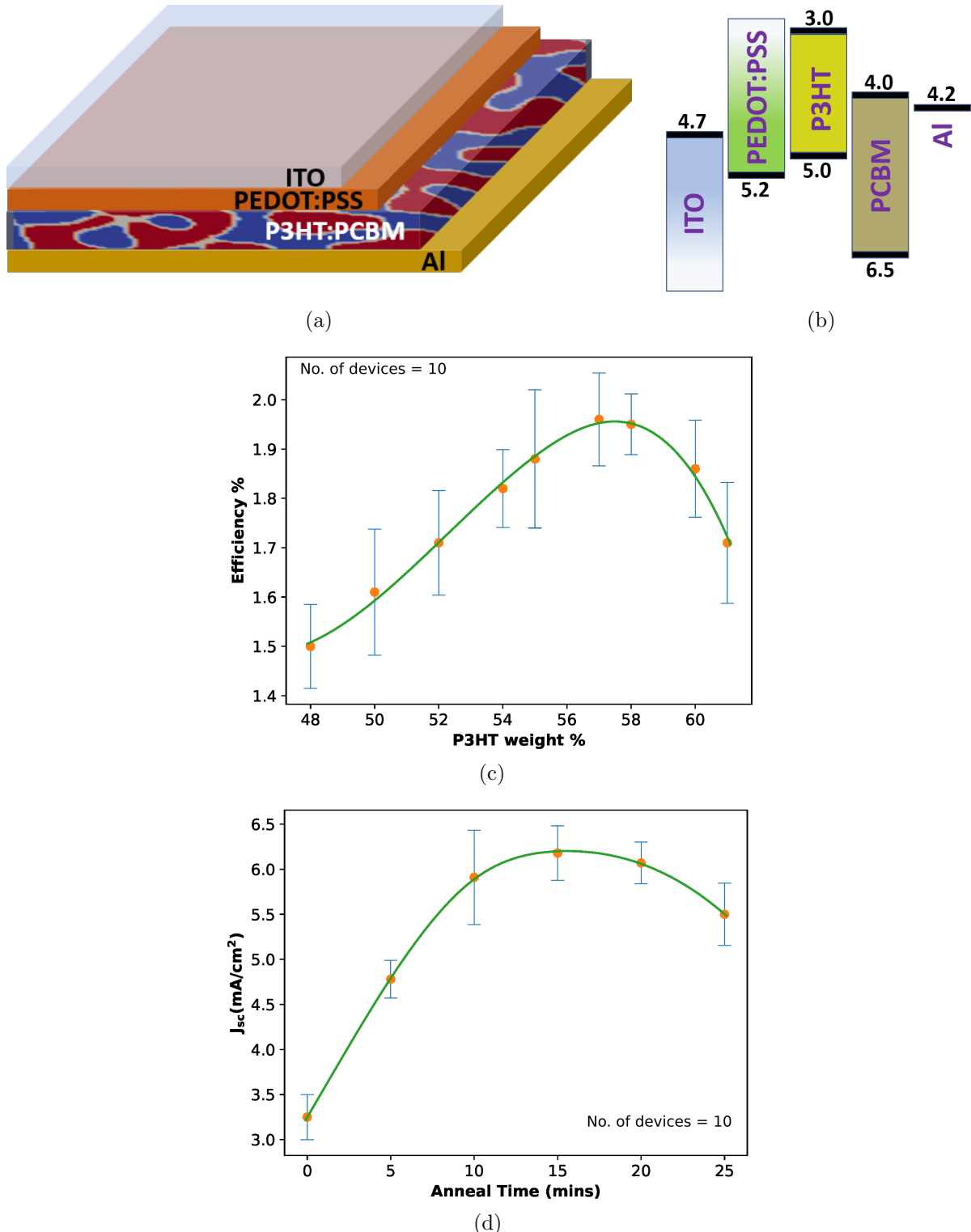


Figure 3.3: (a) Device architecture (b) energy band diagram (c) experimental efficiency vs weight % of PCBM (d) experimental J_{sc} vs annealing time
Note: The lines have been drawn using spline interpolation just to follow the points and have no physical significance.

3. EXPERIMENTATION

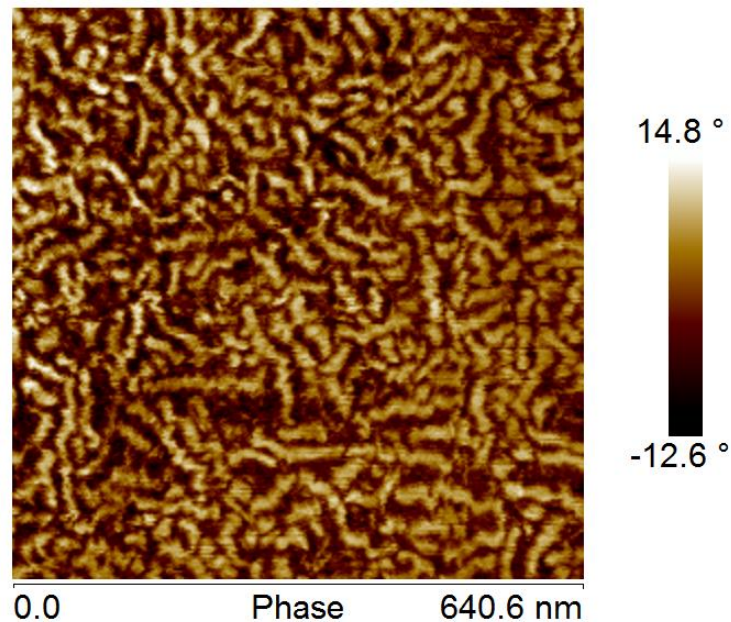


Figure 3.4: Phase contrast image of P3HT:PCBM active layer for 1:0.8 blend ratio. The light yellow phase corresponds to P3HT fibrils whereas dark brown phase corresponds to PCBM.

wherein the domains are 100 nm in size is shown in Figure 3.6.

In order to understand and quantify the features of morphology that influence device performance, we modeled the process-structure-property relationship in organic-semiconductors using the formulation that will be described in the next chapter.

3. EXPERIMENTATION

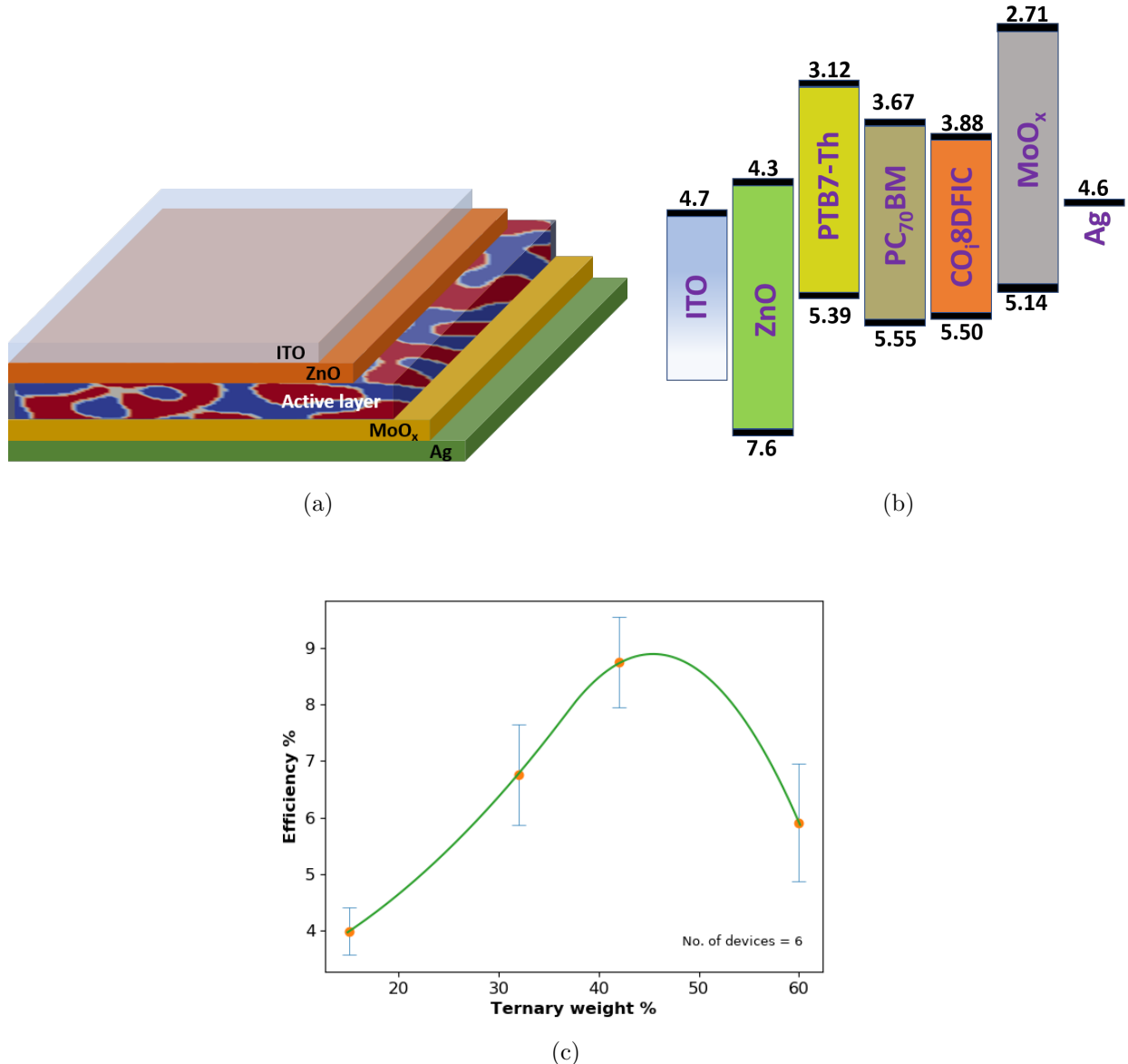


Figure 3.5: (a) Device architecture (b) energy band diagram (c) experimental efficiency vs weight % of ternary acceptor. Note: The lines have been drawn using spline interpolation just to follow the points and have no physical significance.

3. EXPERIMENTATION

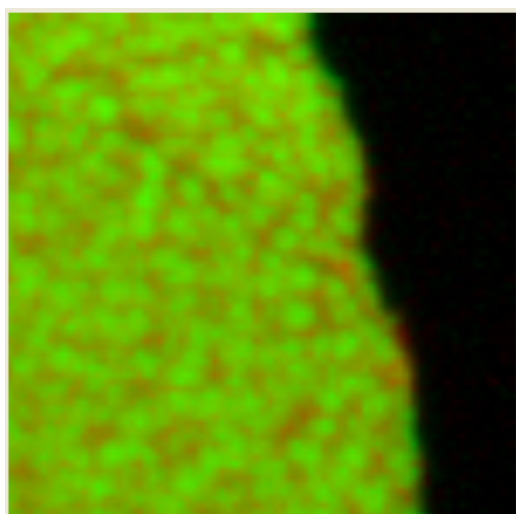


Figure 3.6: PC₇₀BM is depicted by green color and PTB7-Th by red. The domains size is around 100 nm.

Chapter 4

Formulation

In order to understand and quantify the morphological features that influence device performance, we modeled the process-structure-property relationship in organic-semiconductors. This chapter details the formulation for deriving process-structure and structure-property correlations. Further, since we propose a novel diffuse-interface method for modeling structure-property relationship, we have benchmarked the model against classical sharp interface analytical model for a bilayer device. Finally, the assumptions made while deriving these models are listed.

4.1 Process-structure model

For investigating the effect of processing parameters (blend ratio and annealing time) on the resulting microstructure, the phase-field model has been used since they are most appropriate for modeling microstructure evolution. This is because these models are robust as the evolution laws are derived in a thermodynamically consistent fashion, and their implementation is typically possible with more straightforward numerical methods than corresponding sharp-interface approaches. This is particularly true for the morphological evolution in the realm of materials science which often involves complex geometries with multiple curvatures that are handled conveniently with the diffuse-interface models. It has been assumed that the polymer-blend undergoes spinodal decomposition [112, 111, 109, 107]. The mathematical framework for generating process-structure correlations using the Cahn-Hilliard formulation has been described in this chapter. We have extended the formulation implemented by Bhattacharyya [179] to a ternary polymer blend.

The bulk thermodynamics of the ternary system have been captured using the Flory-Huggins

4. FORMULATION

free energy function(4.1) which reads,

$$f(\phi_a, \phi_b, \phi_c) = \chi_{ab}\phi_a\phi_b + \chi_{bc}\phi_b\phi_c + \chi_{ca}\phi_c\phi_a + \frac{RT}{V_m} \left(\frac{\phi_a}{N'_a} \log \phi_a + \frac{\phi_b}{N'_b} \log \phi_b + \frac{\phi_c}{N'_c} \log \phi_c \right), \quad (4.1)$$

where ϕ_i represents the volume fraction of the component a, b or c; V_m represents the reference molar volume; T is the temperature and R , the universal gas constant; N'_i , the relative size; χ_{ij} is the Flory interaction parameter between i and j species. Figure 4.1(a) shows a representative bulk free energy plot for a system with $\chi_{ab} = \chi_{bc} = \chi_{ca} = 3$, $N'_a = 5$, $N'_b = 1$ and $N'_c = 1$. An isothermal section of the phase diagram depicting the two-phase equilibrium between the ternary components is shown in Figure 4.1(b). The calculation of phase diagram is shown in Appendix A.

The interaction parameter χ_{ij} between species i and j is calculated as:

$$\chi_{ij} = \frac{Z_{ij}(2E_{ij} - E_{ii} - E_{jj})}{2k_B T} \quad (4.2)$$

where E_{ij} is the bond energy of nearest ij pair; Z_{ij} corresponds to the number of j neighbours of i^{th} species; k_B , the Boltzmann constant; T is the temperature.

4.1.1 Energy of a compositionally inhomogeneous system

The resultant Helmholtz free energy (F), of an isotropic ternary system with compositional inhomogeneities is represented by the Cahn-Hilliard free energy functional as:

$$F = \int \left[f(\phi_a, \phi_b, \phi_c) + \sum_{i=a,b,c} \kappa_i (\nabla \phi_i)^2 \right] dV, \quad (4.3)$$

where, f is the Flory-Huggins bulk free-energy density and κ_i is the gradient energy coefficient of a, b or c.

4. FORMULATION

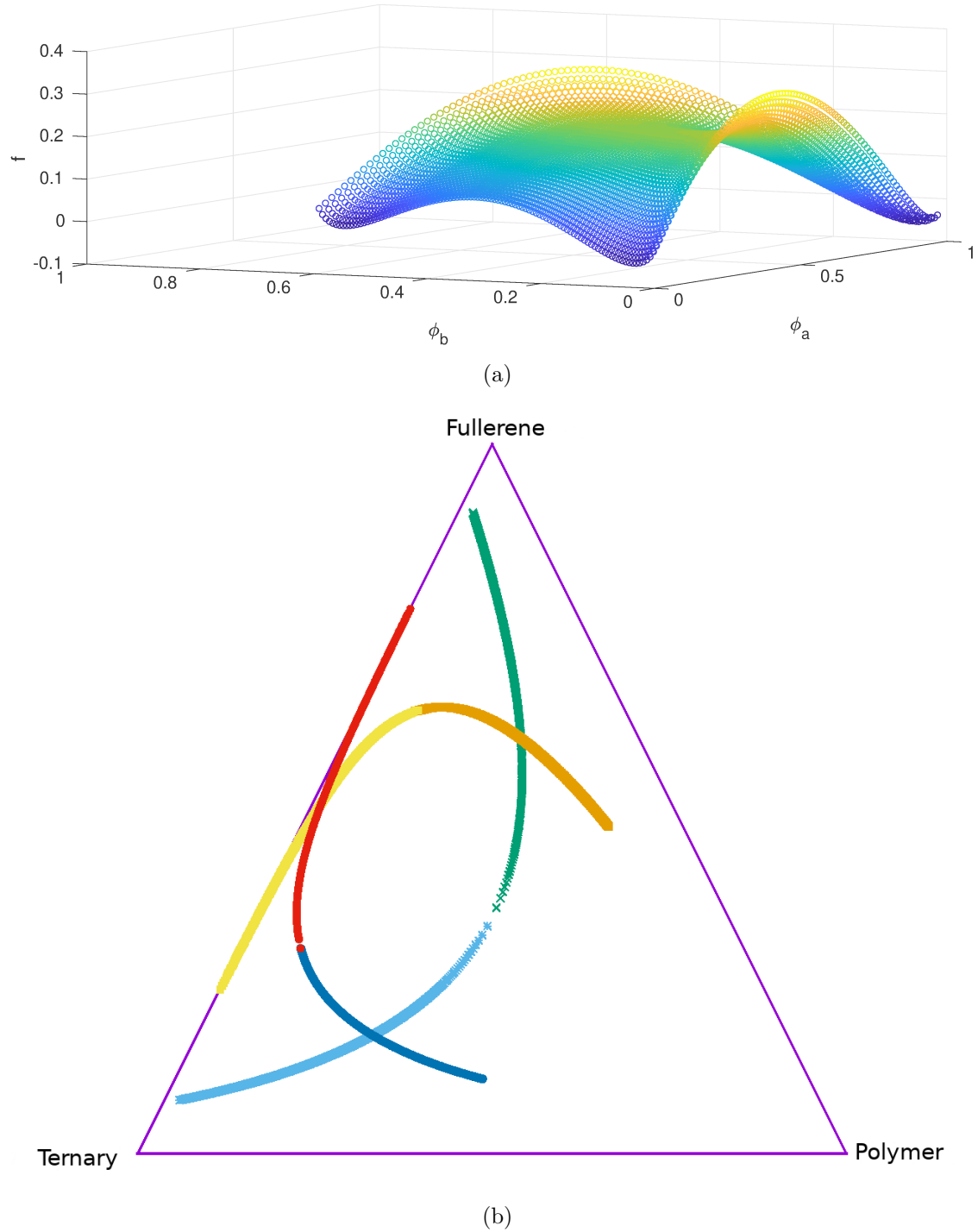


Figure 4.1: (a) Bulk free energy for a representative system (a, b and c represent polymer, fullerene and ternary component respectively) with $\chi_{ab} = \chi_{bc} = \chi_{ca} = 3$, $N'_a = 5$, $N'_b = 1$ and $N'_c = 1$. (b) Isothermal section of the phase diagram for polymer, fullerene and ternary component.

4. FORMULATION

4.1.2 Kinetics

The kinetics of evolution of the volume fraction fields ϕ_i are described in this section. The continuity equation reads as:

$$\frac{\partial \phi_i}{\partial t} = -\nabla \cdot \bar{J}_i, \quad (4.4)$$

where, \bar{J}_i represents the net flux density of i_{th} species relative to the frame of reference of the laboratory. \bar{J}_i is related to J_i (species flux measured with respect to local frame) by the relation:

$$\bar{J}_i = J_i - \sum_i \phi_i (J_a + J_b + J_c) \quad (4.5)$$

Further simplification of this equation for species a reads as:

$$\bar{J}_a = -(1 - \phi_a) \Lambda_a \nabla \mu'_a + \phi_a \Lambda_b \nabla \mu'_b + \phi_a \Lambda_c \nabla \mu'_c \quad (4.6)$$

where, it has been assumed that $J_i = -\Lambda_i \nabla \mu'_i$, implying that the local flux of i^{th} species is proportional to the chemical potential gradient ($\nabla \mu'_i$); Λ_i being the mobility of the atoms. Similarly,

$$\bar{J}_b = -(1 - \phi_b) \Lambda_b \nabla \mu'_b + \phi_b \Lambda_a \nabla \mu'_a + \phi_b \Lambda_c \nabla \mu'_c \quad (4.7)$$

$$\bar{J}_c = -(1 - \phi_c) \Lambda_c \nabla \mu'_c + \phi_c \Lambda_a \nabla \mu'_a + \phi_c \Lambda_b \nabla \mu'_b \quad (4.8)$$

Since $\sum_i \bar{J}_i = 0$, only two of the above mentioned flux expressions (with respect to laboratory reference frame) are independent. Henceforth, \bar{J}_a and \bar{J}_b will be used as the independent ones.

Since $\sum_i \phi_i = 1$, the Gibbs-Duhem equation, $\sum_i \phi_i \nabla \mu'_i = 0$ can also be rearranged to derive:

$$\nabla \mu'_c = -\phi_a \nabla \bar{\mu}_a - \phi_b \nabla \bar{\mu}_b. \quad (4.9)$$

4. FORMULATION

Further algebra results in:

$$\nabla \mu'_a = (1 - \phi_a) \nabla \bar{\mu}_a - \phi_b \nabla \bar{\mu}_b, \quad (4.10)$$

$$\nabla \mu'_b = (1 - \phi_b) \nabla \bar{\mu}_b - \phi_a \nabla \bar{\mu}_a, \quad (4.11)$$

where, $\nabla \bar{\mu}_a = \nabla(\mu'_a - \mu'_c)$ and $\nabla \bar{\mu}_b = \nabla(\mu'_b - \mu'_c)$ with $\bar{\mu}_i$ being the chemical diffusion potential. Using equations (4.10), (4.11) and (4.9) in equations (4.6) and (4.7) respectively, we have,

$$\begin{aligned} \bar{J}_a &= - [(1 - \phi_a)^2 \Lambda_a + \phi_a^2 (\Lambda_b + \Lambda_c)] \nabla \bar{\mu}_a \\ &\quad + [(1 - \phi_a)\phi_b \Lambda_a + (1 - \phi_b)\phi_a \Lambda_b - \phi_a \phi_b \Lambda_c] \nabla \bar{\mu}_b, \\ \bar{J}_b &= + [\phi_a(1 - \phi_b) \Lambda_b + (1 - \phi_a)\phi_b \Lambda_a - \phi_a \phi_b \Lambda_c] \nabla \bar{\mu}_a \\ &\quad - [(1 - \phi_b)^2 \Lambda_b + \phi_b^2 (\Lambda_a + \Lambda_c)] \nabla \bar{\mu}_b. \end{aligned} \quad (4.12)$$

Simplifying the above expressions further by using the following effective mobilities,

$$\begin{aligned} \Lambda_{aa} &= (1 - \phi_a)^2 \Lambda_a + \phi_a^2 (\Lambda_b + \Lambda_c), \\ \Lambda_{bb} &= (1 - \phi_b)^2 \Lambda_b + \phi_b^2 (\Lambda_a + \Lambda_c), \\ \Lambda_{ab} &= \Lambda_{ba} = (1 - \phi_a)\phi_b \Lambda_a + \phi_a(1 - \phi_b) \Lambda_b - \phi_a \phi_b \Lambda_c. \end{aligned} \quad (4.13)$$

Note that the effective mobilities are elements of a symmetric 2x2 mobility matrix.

Thus the flux equations may be rewritten in the simplified form as:

$$\begin{aligned} \bar{J}_a &= -\Lambda_{aa} \nabla \bar{\mu}_a + \Lambda_{ab} \nabla \bar{\mu}_b, \\ \bar{J}_b &= -\Lambda_{bb} \nabla \bar{\mu}_b + \Lambda_{ab} \nabla \bar{\mu}_a. \end{aligned} \quad (4.14)$$

In the Cahn-Hilliard simulations, a mobility matrix has been adopted such that its elements are constants independent of the local composition. For the same, the species mobility i.e., Λ_a , Λ_b and Λ_c wherein $\Lambda_a = \Lambda_b$ are the elementary quantities. The elements of the mobility matrix i.e., Λ_{aa} , Λ_{bb} and Λ_{ab} are calculated at equal volume fraction of $(\phi_a, \phi_b, \phi_c) = (1/3, 1/3, 1/3)$; this ensures that there is no bias with respect to composition. Thereafter, the mobility matrix elements are rescaled (since the matrix is symmetric in species a and b) such that $\Lambda_{aa} = \Lambda_{bb} = 1.0$.

4. FORMULATION

In case of bulk homogeneous ternary solutions, $\bar{\mu}_i$ ($i \in a, b$) is represented by:

$$\bar{\mu}_i = \frac{\partial f}{\partial \phi_i}. \quad (4.15)$$

In case of Cahn-Hilliard formulation, $\bar{\mu}_i$ is defined as the variational derivative of the total free energy with respect to volume fraction and is represented as:

$$\bar{\mu}_i = \frac{\delta F}{\delta \phi_i}. \quad (4.16)$$

Using the Euler-Lagrange equation for calculating the variational derivative:

$$\frac{\delta F}{\delta \phi_i} = \frac{\partial I}{\partial \phi_i} - \frac{\partial}{\partial x} \frac{\partial I}{\partial (\nabla \phi_i)}, \quad (4.17)$$

where, $I = f(\phi_a, \phi_b, \phi_c) + \sum_{i=a,b,c} \kappa_i (\nabla \phi_i)^2$

we get,

$$\begin{aligned} \bar{\mu}_a &= \frac{\partial f}{\partial \phi_a} - 2(\kappa_a + \kappa_c) \nabla^2 \phi_a - 2\kappa_c \nabla^2 \phi_b, \\ \bar{\mu}_b &= \frac{\partial f}{\partial \phi_b} - 2(\kappa_b + \kappa_c) \nabla^2 \phi_b - 2\kappa_c \nabla^2 \phi_a, \end{aligned} \quad (4.18)$$

where, upon substituting Eq.(4.18) into Eq.(4.14) and then subsequently Eq.(4.14) into the continuity equation (4.4), yields:

$$\begin{aligned} \frac{\partial \phi_a}{\partial t} &= \Lambda_{aa} \left[\nabla^2 \left(\frac{\partial f}{\partial \phi_a} \right) - 2(\kappa_a + \kappa_c) \nabla^4 \phi_a - 2\kappa_{ab} \nabla^4 \phi_b \right] \\ &\quad - \Lambda_{ab} \left[\nabla^2 \left(\frac{\partial f}{\partial \phi_b} \right) - 2(\kappa_b + \kappa_c) \nabla^4 \phi_b - 2\kappa_{ab} \nabla^4 \phi_a \right], \end{aligned} \quad (4.19)$$

$$\begin{aligned} \frac{\partial \phi_b}{\partial t} &= \Lambda_{bb} \left[\nabla^2 \left(\frac{\partial f}{\partial \phi_b} \right) - 2(\kappa_b + \kappa_c) \nabla^4 \phi_b - 2\kappa_{ab} \nabla^4 \phi_a \right] \\ &\quad - \Lambda_{ab} \left[\nabla^2 \left(\frac{\partial f}{\partial \phi_a} \right) - 2(\kappa_a + \kappa_c) \nabla^4 \phi_a - 2\kappa_{ab} \nabla^4 \phi_b \right]. \end{aligned} \quad (4.20)$$

We assume for the sake of convenience $\kappa_{aa} = \kappa_a + \kappa_c$, $\kappa_{bb} = \kappa_b + \kappa_c$ and $\kappa_{ab} = \kappa_{ba} = \kappa_c$. The above mentioned equations form a 2x2 matrix of gradient coefficients in a ternary component system.

4. FORMULATION

Thus, the simplified equations read as:

$$\begin{aligned} \frac{\partial \phi_a}{\partial t} &= \Lambda_{aa} \left[\nabla^2 \left(\frac{\partial f}{\partial \phi_a} \right) - 2\kappa_{aa} \nabla^4 \phi_a - 2\kappa_{ab} \nabla^4 \phi_b \right] \\ &\quad - \Lambda_{ab} \left[\nabla^2 \left(\frac{\partial f}{\partial \phi_b} \right) - 2\kappa_{bb} \nabla^4 \phi_b - 2\kappa_{ab} \nabla^4 \phi_a \right], \end{aligned} \quad (4.21)$$

$$\begin{aligned} \frac{\partial \phi_b}{\partial t} &= \Lambda_{bb} \left[\nabla^2 \left(\frac{\partial f}{\partial \phi_b} \right) - 2\kappa_{bb} \nabla^4 \phi_b - 2\kappa_{ab} \nabla^4 \phi_a \right] \\ &\quad - \Lambda_{ab} \left[\nabla^2 \left(\frac{\partial f}{\partial \phi_a} \right) - 2\kappa_{aa} \nabla^4 \phi_a - 2\kappa_{ab} \nabla^4 \phi_b \right]. \end{aligned} \quad (4.22)$$

The non-dimensionalisation scheme that has been adopted for the process-structure model is described in the following section.

4.1.3 Non-dimensionalization for process–structure model

We utilize the following scales for energy (f^*) = $\frac{RT^*}{V_m}$, length (l^*) = $\frac{\sigma^*}{f^*}$ and time (t^*) = $\frac{l^{*2}}{D^*}$ for non-dimensionalizing the free-energy density and the kinetic parameters. The typical scales of these parameters at $T^* = 298$ K for PCDTBT:PC₇₁BM solar cell are as follows [180, 181, 182, 109]:

V_m^{PC70BM} : 5.0×10^{-4} m³/mol; $\sigma^* = 25$ mN/m; $D^* = 5.0 \times 10^{-12}$ m²/s.

4.1.4 Numerical solution

Here, we extend the semi-implicit Fourier spectral formuation developed by Chen and Shen [183] to a ternary system. The Fourier transform of Eq.(4.21) and Eq.(4.22) reads as:

$$\begin{aligned} \frac{\partial \tilde{\phi}_a(k, t)}{\partial t} &= \Lambda_{aa} \left[-k^2 \tilde{g}_a(k) - 2\kappa_{aa} k^4 \tilde{\phi}_a - 2\kappa_{ab} k^4 \tilde{\phi}_b \right] \\ &\quad - \Lambda_{ab} \left[-k^2 \tilde{g}_b(k) - 2\kappa_{ab} k^4 \tilde{\phi}_a - 2\kappa_{bb} k^4 \tilde{\phi}_b \right], \end{aligned} \quad (4.23)$$

$$\begin{aligned} \frac{\partial \tilde{\phi}_b(k, t)}{\partial t} &= \Lambda_{bb} \left[-k^2 \tilde{g}_b(k) - 2\kappa_{bb} k^4 \tilde{\phi}_b - 2\kappa_{ab} k^4 \tilde{\phi}_a \right] \\ &\quad - \Lambda_{ab} \left[-k^2 \tilde{g}_a(k) - 2\kappa_{ab} k^4 \tilde{\phi}_b - 2\kappa_{aa} k^4 \tilde{\phi}_a \right], \end{aligned} \quad (4.24)$$

where $g_a = \frac{\partial f}{\partial \phi_a}$, $g_b = \frac{\partial f}{\partial \phi_b}$. \mathbf{k} is a vector in Fourier space and $k = |\mathbf{k}|$. $\tilde{\phi}_a(k, t)$ and $\tilde{\phi}_b(k, t)$ are the Fourier transforms of volume fraction in real space. Using the finite difference method

4. FORMULATION

for $\frac{\partial \tilde{\phi}_a}{\partial t}$ and $\frac{\partial \tilde{\phi}_b}{\partial t}$ we derive,

$$\frac{\partial \tilde{\phi}_i}{\partial t} = \left(\frac{\tilde{\phi}_i(k, t + \Delta t) - \tilde{\phi}_i(k, t)}{\Delta t} \right) \quad (4.25)$$

where $i = a, b$. The linear terms, $\tilde{\phi}_a$ and $\tilde{\phi}_b$ are treated implicitly and the non-linear terms, \tilde{g}_a and \tilde{g}_b are treated explicitly. The semi-implicit formulation yields the following equations that are solved iteratively for obtaining the microstructures:

$$\begin{bmatrix} Q_{11} & Q_{12} \\ Q_{21} & Q_{22} \end{bmatrix} \begin{bmatrix} \tilde{\phi}_a(t + \Delta t) \\ \tilde{\phi}_b(t + \Delta t) \end{bmatrix} = \begin{bmatrix} \tilde{\phi}_a(t) - \Lambda_{aa}k^2\tilde{g}_a\Delta t + \Lambda_{ab}k^2\tilde{g}_b\Delta t \\ \tilde{\phi}_b(t) - \Lambda_{bb}k^2\tilde{g}_b\Delta t + \Lambda_{ab}k^2\tilde{g}_a\Delta t \end{bmatrix} \quad (4.26)$$

where,

$$\begin{aligned} Q_{11} &= 1 + 2\Lambda_{aa}\kappa_{aa}k^4\Delta t - 2\Lambda_{ab}\kappa_{ab}k^4\Delta t, \\ Q_{12} &= 2(\Lambda_{aa}\kappa_{ab} - \Lambda_{ab}\kappa_{bb})k^4\Delta t, \\ Q_{21} &= 2(\Lambda_{bb}\kappa_{ab} - \Lambda_{ab}\kappa_{aa})k^4\Delta t, \\ Q_{22} &= 1 + 2\Lambda_{bb}\kappa_{bb}k^4\Delta t - 2\Lambda_{ab}\kappa_{ab}k^4\Delta t. \end{aligned} \quad (4.27)$$

The phase-field code has been written in CUDA C, and the governing equations have been numerically solved using the semi-implicit Fourier spectral formulation on the Tesla V100-SXM2 GPU card.

4.2 Structure-property model

In order to model the microstructure-property relationship, we begin with the discussion of basic semiconductor equations.

4.2.1 Semiconductor equations

The equations governing the carrier transport in a given phase α reads as,

$$\nabla \cdot (\epsilon^\alpha \nabla \xi) = - \left(\sum_i q_i c_i + q_i (N_D^\alpha - N_A^\alpha) \right) \quad (4.28)$$

$$J_i = -q_i D_i^\alpha \nabla c_i - \lambda_i^\alpha q_i c_i \nabla \xi \quad (4.29)$$

4. FORMULATION

$$\frac{\partial c_i}{\partial t} = \nabla \cdot (D_i^\alpha \nabla c_i + \lambda_i^\alpha c_i \nabla \xi) \quad (4.30)$$

where (4.28) represents the Poisson's equation and (4.29) represents the net current density of carriers due to drift and diffusion, i represents the charged species that is either electron or hole and α represents the semiconducting phase that is donor or acceptor; ϵ^α is the dielectric constant in the phase α ; ξ is the electrostatic potential; q_i is the charge density given by $z_i F$ with units Coulomb/mol, where z_i is the valence of the charge carrier; c_i corresponds to the carrier density, with units mol/m^3 ; N_A^α and N_D^α represent the acceptor and donor densities respectively, with units mol/m^3 ; J_i represents the net current density of carriers, with units Coloumb/ $m^2 s$; D_i^α represents the diffusivity of the i^{th} species in α phase; λ_i^α is the electronic mobility, where the mass conservation equation 4.30 is written in terms of the concentration field of the charged species. This is the classical sharp interface model. In order to solve for the electrostatic and electron, hole density fields across a one-dimensional heterogeneous junction consisting of two-phases, the equations 4.28 and 4.30 are solved in a coupled manner in each of the bulk phases, while at the interface between the two phases, the continuity of electrostatic potential as well as the continuity of the fluxes is imposed, with which the steady-state electron-hole density profiles as well as the electrostatic potential field across the interfaces is derived. The complexity of this model increases as the Bulk-hetero-junction assumes complicated geometries as now the imposition of continuity of normal fluxes across the interface between a donor and acceptor domain requires the description of the shape of the interface. Additionally, since the thickness of active-layer is typically 100 nm which is about the same as that of the depletion width which is 60 nm [146], we can expect near-complete depletion, and thereby the concentration of carriers is low. This makes the mass conservation equation 4.30 numerically stiff, requiring complex solution routines and possible refinement of meshes near regions of rapid concentration changes near the interface and in particular when the morphology comes in contact with the electrodes. In order to deal with complex morphologies and low concentration of carriers as is typical in organic-semiconductors (OS), we adopt the diffuse interface model, where we create a mathematically smeared interface of a fixed finite width, replacing the sharp-interface between the domains. Additionally, we transform the mass-conservation equation into an equation for the effective diffusion potential as we will see below. The additional requirement of refinement of meshes at interfaces is avoided in the diffuse-interface model by firstly resolving the interface with a sufficient number of points (10 in our case) and secondly, we solve for the diffusion potential, whose variation is orders of magnitude lesser than the corresponding concentration variations across interfaces. Therefore, this model does not specifically require variable mesh

4. FORMULATION

density at the interfaces. For the present situation, this involves the creation of three different indicator functions where each of them assumes a value of 1 only in regions occupied by one of the three-bulk phases while having a value of zero in the parts of the domain where the other bulk phases are present, as shown in Figure 4.2. The association of the domain morphology derived from the simulated microstructures with the indicator functions is performed by firstly assigning regions rich in composition A, B, C to indicator functions ψ_1 , ψ_2 and ψ_3 respectively. Thus $\psi_1 = 1$ where component A is rich while being zero everywhere else, similarly $\psi_2 = 1$, $\psi_3 = 1$ where components B and C respectively are in excess, while being zero elsewhere. This distribution of the indicator functions leads to domains with abrupt boundaries across which there is a rapid transition of the indicator functions (from 0 to 1 or vice-versa). The sharp interface like distribution of the domains is thereafter smoothed by using a multi-phase field model for a few time iterations that lead to the creation of interfaces with finite width replacing the sharp binary interfaces. Thus, on traversing normal to any binary interface, there will be a variation of two indicator functions between the values of 0 and 1, while the third indicator function remains zero. The variation from 0 to 1 of the respective indicator functions at each of the binary interfaces between the bulk phases, occurs smoothly over a finite width. Similarly, all three indicator functions exhibit smoothly varying non-zero values in the three-phase co-existence regions (diffuse triple-points).

With this diffuse-interface mapping, the electronic properties of the bulk phases may now be interpolated using the indicator functions that allow for a smooth variation of all the relevant properties in the entire domain. However, since there is no sharp demarcation between the phase-boundaries the driving forces for the diffusion currents may no longer be described by just the concentration gradients, but must be replaced by the chemical potential gradients as this is an intensive variable whose gradient unambiguously describes the diffusion current at any point in the domain. The linear superposition of the chemical potential and $q_i\xi$, i.e $\tilde{\mu}_i = \mu_i + q_i\xi$, is, therefore, a well defined thermodynamic quantity that is referred to as the electrochemical potential, whose gradients provides driving forces for electronic current (drift+diffusion) in the domain, and thereby the condition of zero/constant gradients in the electrostatic potential leads to the state of equilibrium/steady-state. Formulating the drift-diffusion equations in this manner, where the driving forces are written in terms of the gradients of the conjugate thermodynamic potentials has an additional numerical advantage, where, although the concentration sees variations differing by orders of magnitude, across the interface, the respective values of the chemical potential vary over a much smaller range, thereby making the numerical treatment much easier, compared to the use of concentrations. Therefore, in order to derive the electronic current equations in the diffuse-interface approach, in terms of electrochemical potential, we

4. FORMULATION

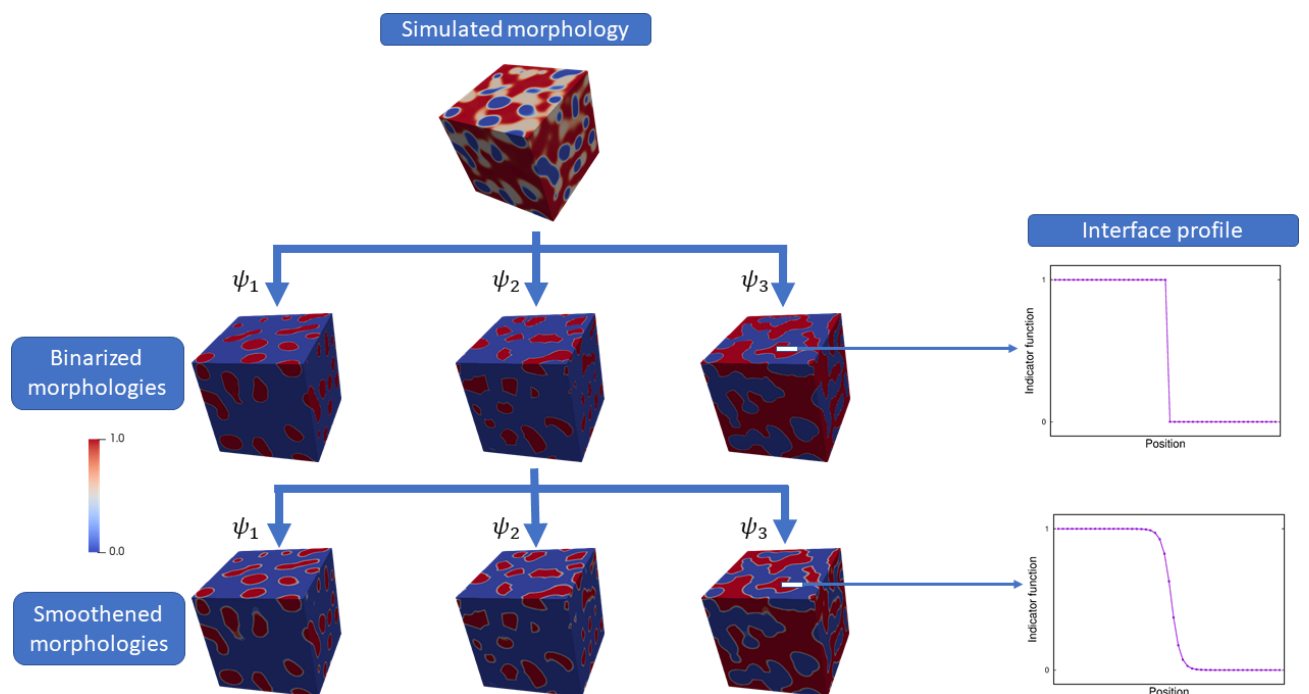


Figure 4.2: Surface profiles of the morphologies generated using the process-structure model that have been binarised and then smoothed for incorporation in the structure-property model.

4. FORMULATION

define the electronic free-energy of the system in the following section[65].

4.2.2 Free-Energy

The electronic free-energy of each phase in the system considering that electrons and holes are much lower in concentration than the host atoms may be written for one-mole of the phase as,

$$g^\alpha = \sum_i (E_i^\alpha x_i^\alpha + RT (x_i^\alpha \ln x_i^\alpha - x_i^\alpha) + q_i x_i^\alpha \xi) \quad (4.31)$$

where E_i^α represents the Fermi level of the hole and electron in the α -phase and x_i^α is the mole-fraction of the i^{th} species(electron or hole). Therefore, the electrochemical diffusion potential of i^{th} species (hole,electron), ($\tilde{\mu}_i$) turns out to be,

$$\tilde{\mu}_i = RT \ln x_i^\alpha + E_i^\alpha + q_i \xi, \quad (4.32)$$

where μ_i is the chemical part of the diffusion potential that reads, $\mu_i = RT \ln x_i^\alpha + E_i^\alpha$. Thus, the mole-fraction of the electron/hole species, may be expressed as,

$$x_i^\alpha = \exp \left(\frac{\mu_i - E_i^\alpha}{RT} \right). \quad (4.33)$$

4.2.3 Model Formulation

In this section, we derive an alternate form of the drift-diffusion model governing the transport of electrons and holes, wherein particular we present a modified version of the Eqn.4.30, using the gradients of electrochemical potential $\tilde{\mu}_i$ as the driving force for (drift + diffusion), while we solve for the chemical part of the diffusion potential μ_i . The above can be derived by noting that, the concentration c_i may be expressed as x_i^α / V_m^α , where V_m^α is the molar volume of the phase α .

$$\frac{\partial}{\partial t} \left(\frac{x_i}{V_m^\alpha} \right) = \nabla \cdot \left(D_i^\alpha \nabla \left(\frac{x_i}{V_m^\alpha} \right) + \lambda_i^\alpha \frac{x_i}{V_m^\alpha} \nabla \xi \right). \quad (4.34)$$

In the preceding relation the molar volume V_m^α is theoretically a function of the mole-fraction of the electron/hole. However, given the size of the electron and hole is much smaller compared to the other constituent species comprising the phases, their individual partial molar volume contribution to the total molar volume may be assumed to be negligible. Or in other words

4. FORMULATION

the variation of the total molar volume with change in the electron/hole mole-fraction $\frac{\partial V_m^\alpha}{\partial x_i}$ is assumed to be small. Because of this assumption, the preceding equation may be simplified to,

$$\frac{1}{V_m^\alpha} \frac{\partial x_i}{\partial t} = \nabla \cdot \left(\frac{D_i^\alpha}{V_m^\alpha} \nabla x_i + \lambda_i^\alpha \frac{x_i}{V_m^\alpha} \nabla \xi \right). \quad (4.35)$$

Using the Einstein relation, $D_i^\alpha = \frac{RT\lambda_i^\alpha}{q_i}$ and additionally introducing the chemical mobility of the atoms as $M_i^\alpha = \frac{D_i}{V_m^\alpha} \frac{\partial x_i}{\partial \mu_i} = \frac{D_i}{V_m^\alpha} \frac{x_i^\alpha}{RT}$, where the last equality derives from the Eqn.4.33, we can transform the preceding equation as,

$$\begin{aligned} \frac{1}{V_m^\alpha} \frac{\partial x_i}{\partial t} &= \nabla \cdot (M_i^\alpha \nabla (\mu_i + q_i \xi)) \\ &= \nabla \cdot (M_i^\alpha \nabla \tilde{\mu}_i). \end{aligned} \quad (4.36)$$

The preceding equation is a fundamental thermodynamic relation, where the change in the electron/hole densities occurs at any point in the domain because of the divergence of the gradients in the electrochemical potential $\tilde{\mu}_i$. Therefore, the condition of equilibrium/steady-state is immediately specified once the gradients vanish or the fluxes described by $-M_i^\alpha \nabla \tilde{\mu}_i$ become constant in the entire domain. While, the previous relation is valid for a given phase α , the equation can be made generic for a distribution of phases, like in a BHJ, by interpolating the chemical mobility using the indicator functions as, $M_i = \sum_\alpha \psi^\alpha M_i^\alpha$, where ψ^α is the α^{th} indicator function as described previously. Additionally, since we presented a motivation for deriving an evolution equation for the conjugate variable μ_i instead of c_i/x_i , because of the ease of numerical treatment, we again utilize the indicator functions for interpolating between the phase compositions as,

$$c_i = \sum_\alpha \frac{x_i^\alpha}{V_m^\alpha} \psi^\alpha, \quad (4.37)$$

which is motivated from the fact no mass is lost when smearing the sharp interface. Therefore, the change in electron/hole compositions can be derived through $\frac{\partial c_i}{\partial t} = \chi_i \frac{\partial \mu_i}{\partial t}$, where $\chi_i = \sum_\alpha \frac{\psi^\alpha}{V_m^\alpha} \frac{\partial x_i^\alpha}{\partial \mu_i}$ and the derivative may be evaluated using the Eqn.4.33. It is noteworthy, that here as well we have made the assumption that $\frac{\partial V_m^\alpha}{\partial x_i}$ is small for both the phases. Inserting

4. FORMULATION

this relation into the preceding equation, we derive,

$$\chi_i \frac{\partial \mu_i}{\partial t} = \nabla \cdot (M_i \nabla (\mu_i + q_i \xi)) . \quad (4.38)$$

Since, we are interested in photo-voltaic applications, there are generation and recombination events that occur along with drift and diffusion. These effects may be introduced as natural source terms in the previous equation as,

$$\chi_i \frac{\partial \mu_i}{\partial t} = \nabla \cdot (M_i \nabla (\mu_i + q_i \xi)) + \dot{G} - \dot{R}, \quad (4.39)$$

where, \dot{G} and \dot{R} represent the generation and recombination rate of carriers respectively; \dot{G} is given by $G_0(\sum_{\alpha}^{N=3}(h^{\alpha})')$ where, G_0 is the coefficient of generation rate of carriers and h^{α} is the interpolation function given by $h^{\alpha}(\psi) = (\psi^{\alpha})^2(3 - 2\psi^{\alpha}) + 2\psi^{\alpha}(\sum_{\beta < \gamma(\beta, \gamma \neq j)} \psi^{\beta}\psi^{\gamma})$. Here it is assumed that the dissociation probability of the excitons to be 1 at the interface, demarcated by the region where the derivative of the interpolation function, $(h^j)'$ is non-zero, thereby the exciton generation rate is directly the carrier generation rate. In this particular formulation, the diffusion of the excitons is also not considered. This is because the microstructural length scale is comparable to the typical exciton diffusion lengths. \dot{R} is modeled using the modified Langevin recombination model in low mobility materials given as,

$$\dot{R} = \gamma \left(\frac{x_e x_h - n_i^2}{V_m^2} \right), \quad (4.40)$$

where x_e and x_h represent the electron and hole mole-fractions respectively; n_i denotes intrinsic carrier mole-fraction, while the recombination coefficient γ is given by [184] that reads,

$$\gamma = \frac{q_i}{\epsilon} \min(M_i), \quad (4.41)$$

where $\min(M_i)$ corresponds to the minimum mobility in the domain of interest. The Poisson equation is also reformulated as,

$$\nabla(\epsilon \nabla \xi) = - \left(\sum_i q_i \left(\sum_{\alpha}^{N=3} \frac{x_i^{\alpha}(\mu_i)}{V_m^{\alpha}} \psi^{\alpha} \right) + F(N_D - N_A) \right), \quad (4.42)$$

where $x_i^{\alpha}(\mu)$ follows from Eqn.4.33, while N_A and N_D are interpolated using $N_A = \sum_{\alpha}^{N=3} \psi^{\alpha} N_A^{\alpha}$

4. FORMULATION

and $N_D = \sum_{\alpha}^{N=3} \psi^{\alpha} N_D^{\alpha}$. The Poisson equation in Eqn.4.42 along with Eqn.4.39 are solved in a coupled manner until steady-state or equilibrium is reached. The non-dimensionalisation scheme that has been adopted for the structure-property model is described in the following section.

4.2.4 Non-Dimensionalization for Structure-Property model

The charge density ρ is scaled by F/V_m^* . The electrostatic potential is normalised by (RT/F) . With this, the natural length scale of the problem derives from the Poisson-equation which is $l^* = \frac{(RT)^{1/2}(\epsilon^*)^{1/2}V_m^{*1/2}}{F}$, where ϵ^* is the scale of the permittivity of one of the semiconducting phases in the vacuum. Therefore, the scale for the current density becomes $\frac{F}{l^*}(M_e + M_h)(RT)$. The typical values of these parameters for PTB7-Th:PCBM solar cell are as follows [181, 185, 186, 187]:

V_m^{PC70BM} : $5.0 \times 10^{-4} \text{ m}^3/\text{mol}$; M : $1.1 \times 10^{-11} \text{ mol}^2\text{s}/\text{kgm}^3$; ϵ : $3.1 \times 10^{-11} \text{ F/m}$; W (Depletion-width): $60 \times 10^{-9} \text{ m}$

4.2.5 System Initialization

For the structure-property predictions, we consider a configuration, as shown in Figure 4.3, where an Electron Transport Layer (ETL) and a Hole Transport Layer (HTL) are placed on either side of the BHJ morphology for conducting simulations that will reveal the current-voltage characteristics and thereby the relevant electronic properties such as the efficiency, fill-factor and the short-circuit current. The ETL and HTL are essential for the selective carrier(electron/hole) conduction to the respective electrodes. In this system, electrodes have been considered in the y-direction and therefore since the imposed current flow is in the same direction, the length of the device in this direction has been optimised as per V_{bi} (keeping the doping densities fixed) such that the length of the device is greater than depletion width. For a V_{bi} of 5 as chosen in this study, the required length of the system corresponds to at least 512, and therefore we have used 512 grid-points in the y-direction.

The simulation is set-up by initialising the composition field of charge carriers (using Eq. 4.37) and doping densities throughout the domain, where the composition at the interface is interpolated using the indicator functions. In order to derive the Fermi-levels (E_i^{α}) of a phase, such that the system is in equilibrium for the given choice of compositions, we equate the electrochemical potential (Eq.(4.32)) of each species in various phases i.e, $\tilde{\mu}_i^{\alpha} = \tilde{\mu}_i^{\beta} = \tilde{\mu}_i^{\gamma} = \dots = \tilde{\mu}_i^N$. For simplicity, consider a two-phase system with electrons and holes as the carriers, then the

4. FORMULATION

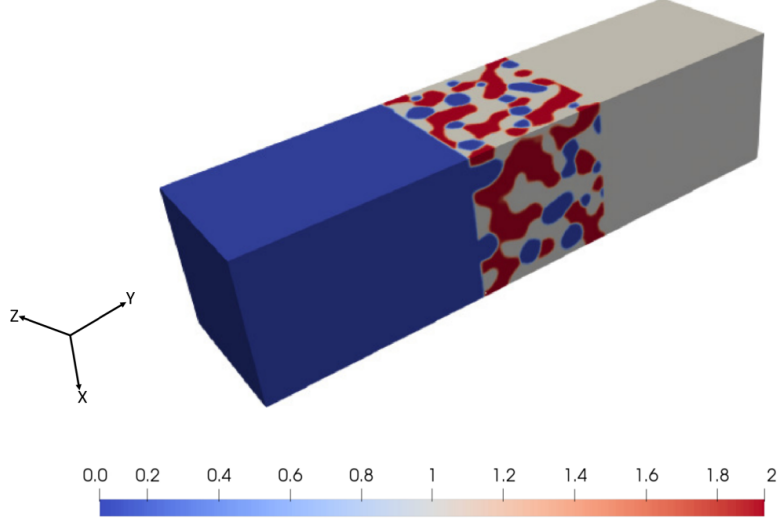


Figure 4.3: Device with a representative BHJ morphology sandwiched between the electron and hole transport layers. The HTL is represented by blue color whereas ETL by grey color. On the color bar, 0 corresponds to the polymer-rich phase, 1 corresponds to fullerene rich phase, and 2 corresponds to ternary component rich phase

Fermi-levels can be determined by equating $\tilde{\mu}_i^\alpha = \tilde{\mu}_i^\beta$ that results in the following,

$$E_i^\alpha = E_i^\beta + RT \ln \frac{x_i^\beta}{x_i^\alpha} + q_i V_{bi}^{\alpha\beta}, \quad (4.43)$$

where, the built-in potential is given by $V_{bi}^{\alpha\beta} = (\xi^\beta - \xi^\alpha)_{eq}$. Therefore, given the built-in potential, initial carrier compositions and upon pinning E_i^β to zero, E_i^α can be computed.

Thereafter, the chemical diffusion potential (μ_i) is calculated in the bulk phases, since the mass conservation equation is described in its terms. In the bulk phase, μ_i is initialised using $\mu_i = RT \ln x_i^\alpha + E_i^\alpha$, however, at the interface the composition distribution follows Eqn.4.37. In order to solve for the chemical diffusion potential distribution that satisfies Eqn.4.37, we substitute for the phase compositions in terms of μ_i using Eqn.4.33 and solve for μ_i using a Newton-Raphson method where iterations are performed until convergence is obtained for a tolerance of 1e-10. With this, the initial distribution of the chemical diffusion potentials in the domain is derived corresponding to the chosen composition distribution.

For the derivation of the current-voltage characteristics, we have thereafter solved for Eqn.4.42 and Eqn.4.39, for different imposed current densities and evaluated the developed potential difference across the electrodes. Dirichlet boundary condition (corresponding to the value in bulk) is imposed on chemical diffusion potential at the bottom of HTL and top of

4. FORMULATION

ETL. In case of electrostatic potential, Dirichlet boundary condition (fixed at 0) is imposed at the top of ETL and at the bottom of HTL, the gradient is fixed corresponding to the imposed current density on the device. For both chemical diffusion potential and electrostatic potential, the zero-flux condition is imposed at the sides of the device. Since the problem is reasonably computationally intensive (involving a 3D microstructure of domain size 128x512x128 along with 3 phases including phase-dependent electronic properties), we have used the OpenFOAM software that is preloaded with efficient multigrid solvers [188]. We have also implemented adaptive time-stepping based on solution residuals. It has been possible to get a considerable time-step ramp-up in our simulations since as the steady-state approaches, the flux of carriers drops down substantially.

We would like to mention that in order to derive a precise solution of transport problems while using diffuse-interface models, the tensorial representation of the mobility can be adopted [189, 190]. This allows for appropriate treatment of the effective resistivities for currents that flow perpendicular as well as parallel to the interface. Scalar interpolations do not provide this freedom, and thereby errors are introduced in the effective boundary conditions, which scale with the interface width as well as with the contrast of the transport coefficients between the phases. However, since we have similar diffusivities among the three phases and since the error scales with this variation, it is still possible to assume scalar interpolation of the mobility coefficients without introducing significant errors. Additionally, we have found that the interface width needs to be much smaller than the depletion width (lower than 6%) such that the open-circuit potential drops across the interfaces both in dark and light conditions are retrieved. Since, the error due to incorrect interpolation scales with the interface width, this additional restriction further reduces the error due to the scalar interpolation method. Therefore, the scalar interpolation method has been adopted as it allows for a computationally efficient implementation.

4.2.6 Benchmarking structure-property model

In this section, the structure-property diffuse interface model has been benchmarked against analytical results obtained from the classical sharp interface model. Thereafter, BHJ device characteristics have been simulated using the model described in the preceding section.

We simulated a bilayer device, i.e., one consisting of p-type and n-type semiconductors sandwiched between electrodes (see Fig. 4.4) to verify whether the model is capturing the device physics.

In order to benchmark the model, the electrostatic potential and charge density profile as

4. FORMULATION

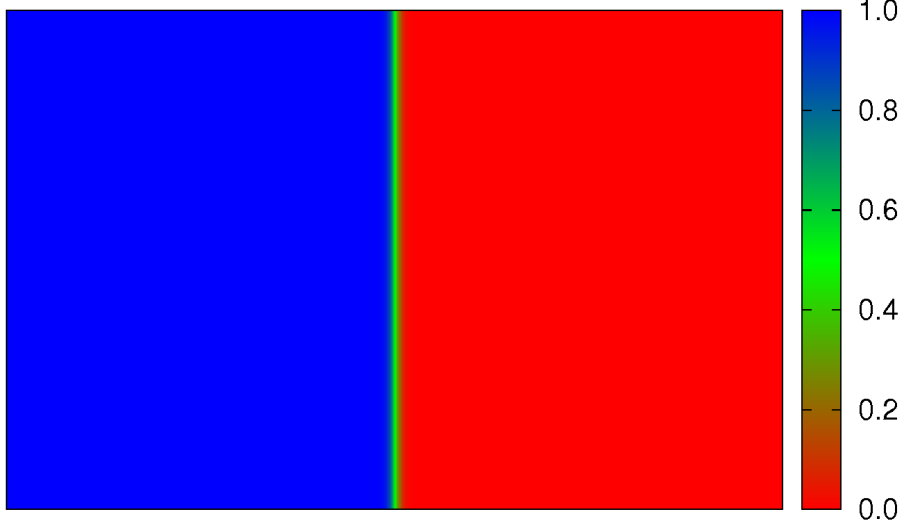


Figure 4.4: Morphology of bilayer device. 1 represents p-type Organic Semiconductor (OS), and 0 represents n-type OS with junction having a diffuse profile.

obtained from the numerical model and analytically were compared against each other in the open-circuit condition. Excellent agreement between the two is observed (Fig. 4.5(a), 4.5(b)). As the p and n-type semiconductors are brought in contact, the holes flow from the p-type to the n-type semiconductor as governed by the chemical potential gradient whereas the electrons flow in the opposite direction. The holes from the p-type semiconductor recombine with the electrons in the n-type semiconductor resulting in exposed positive charge at the n-side of the device due to donor atoms (the mobile carriers were previously shielding this charge). Simultaneously electrons from the n-type semiconductor recombine with the holes in the p-type semiconductor resulting in exposed negative charge at the p side of the device due to acceptor atoms. This diffusion of carriers leads to an electrostatic potential build-up (known as built-in potential V_{bi}) across the PN junction such that it opposes the driving force due to the chemical potential gradient. Equilibrium is reached when the electrostatic potential gradient opposes the chemical potential gradient. In case of charge density as depicted in Fig.4.5(b), the analytical results and that of the model match well except at the PN junction, this is because the analytical equation considers a sharp interface where there is naturally a discontinuity in the charge density whereas the variation is continuous in the diffuse-interface model. Thereafter, the device is simulated in forward and reverse bias in order to observe the variation in depletion width with bias (Fig. 4.5(c)). In the case of forward bias, the electrostatic potential gradient aids the chemical potential gradient resulting in the reduction in depletion width. In contrast, in reverse bias, the electrostatic potential gradient opposes the chemical potential gradient resulting in the

4. FORMULATION

majority carriers flowing away from the PN junction, thereby, increasing the width of the depletion region. It should be noted that all the above profiles have a diffuse interface. The advantage of adopting the diffuse interface approach is that the boundary conditions at the interface are imposed implicitly by the model, thus allowing an easier computational treatment of complex geometries as in the case of BHJ OPVs. Thereafter, the J-V characteristics for the bilayer device under dark and light conditions were simulated. Non-linear J-V characteristics were observed as is typical of semiconductor devices. The nonlinearity arises from the fact that the number of mobile carriers is a function of the applied bias, that increases with the magnitude of the forward bias and vice-versa in reverse bias. The effect of light intensity on this bilayer device was also simulated (see Fig. 4.6(b)). As expected, with increasing light intensity, the maximum current density that can be drawn from the device and the open-circuit voltage increases.

4.2.7 BHJ-Morphology

Having benchmarked the model for a simple bilayer device, we further went on to simulate the J-V characteristics for a complex BHJ morphology. In the present morphology (see Fig. 4.7), the blend ratio is 1:2.5 (p-type:n-type OS). In order to model the device characteristics, the active layer (polymer-fullerene blend) is placed between the buffer layers as is typical in OPVs. The buffer layer aids in allowing the transport of only one charge carrier (i.e., electron or hole), blocking the other one. For the same, the p-type semiconducting buffer layer is placed near the electrode responsible for extracting holes, and the n-type semiconducting buffer layer is placed near the electrode responsible for collecting electrons. J-V characteristics of this morphology in dark and light are shown in Fig. 4.8.

4.3 Assumptions

In this formulation comprising process-structure and structure-property models, we investigate the effect of blend composition on morphology, and its subsequent impact on photovoltaic parameters such as J_{sc} , V_{oc} , FF and η . This allows us to establish PSP correlation in BHJ OPVs, however, some assumptions have been made while deriving the models, and they are listed below:

First, in the process-structure modelling framework, it has been assumed that spinodal decomposition is the mechanism of phase-transformation. This assumption is supported by several experimental and theoretical studies [191, 192, 193, 107, 108, 109]. Collins et al., [192] attempted

4. FORMULATION

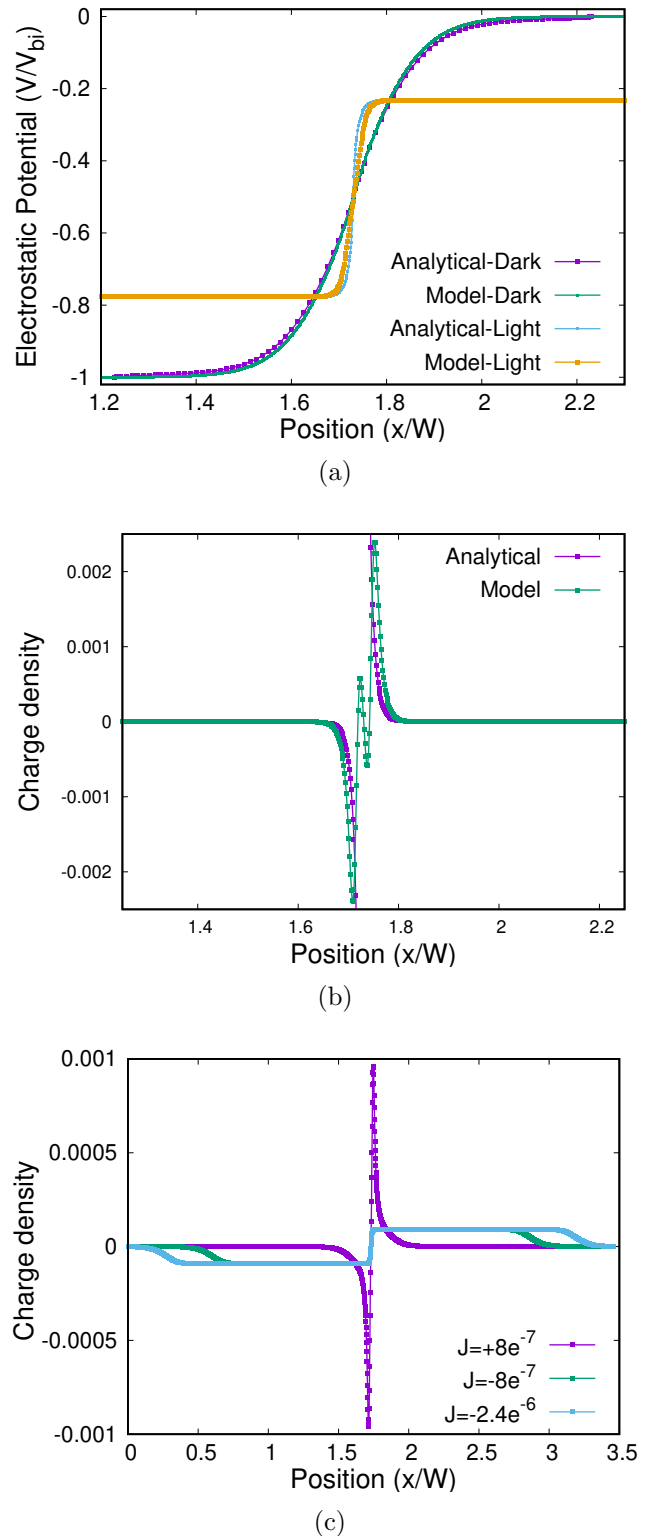
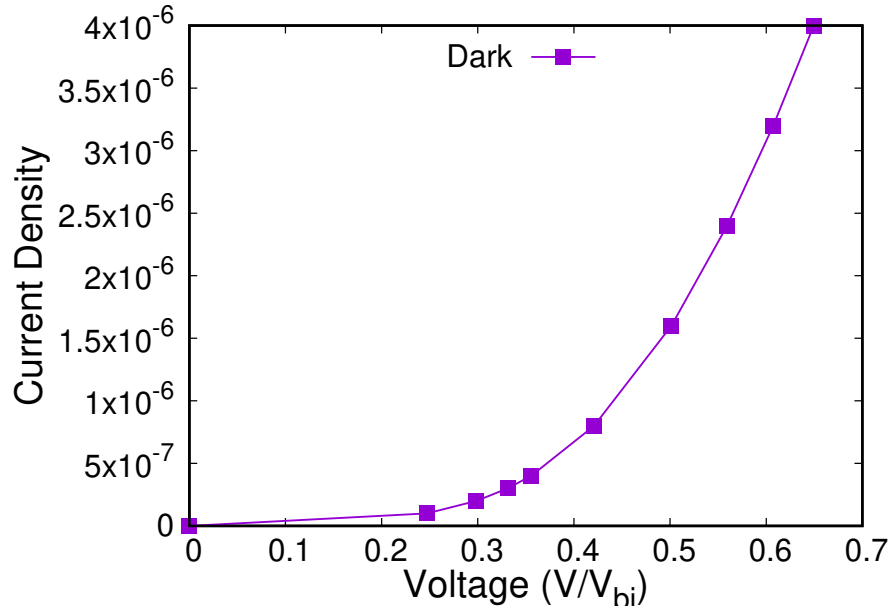
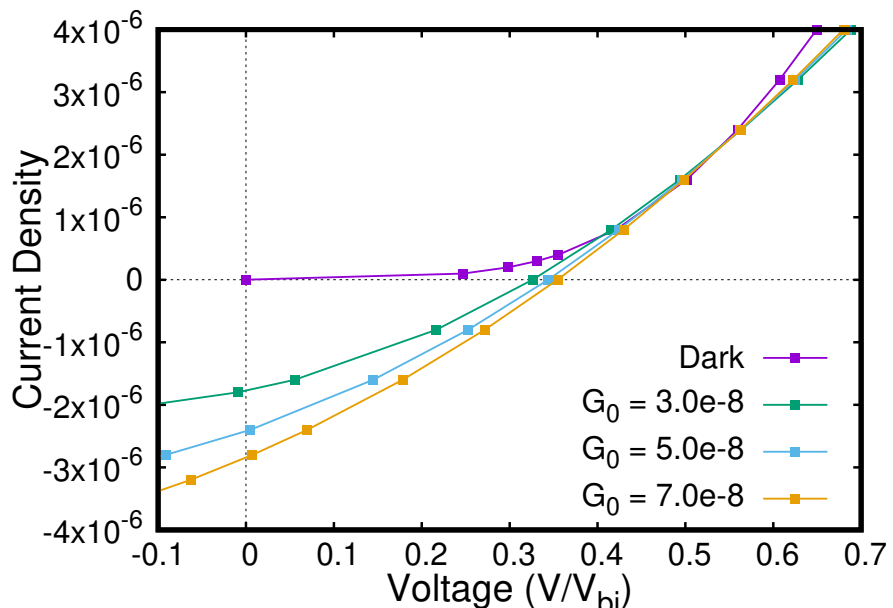


Figure 4.5: Simulation results depicting (a) electrostatic potential profile (b) charge density profile (c) variation in depletion width with bias.

4. FORMULATION



(a)



(b)

Figure 4.6: Simulation results depicting (a) dark J-V characteristics (b) effect of light intensity on device characteristics, G_o is the coefficient of generation rate of carriers.

4. FORMULATION

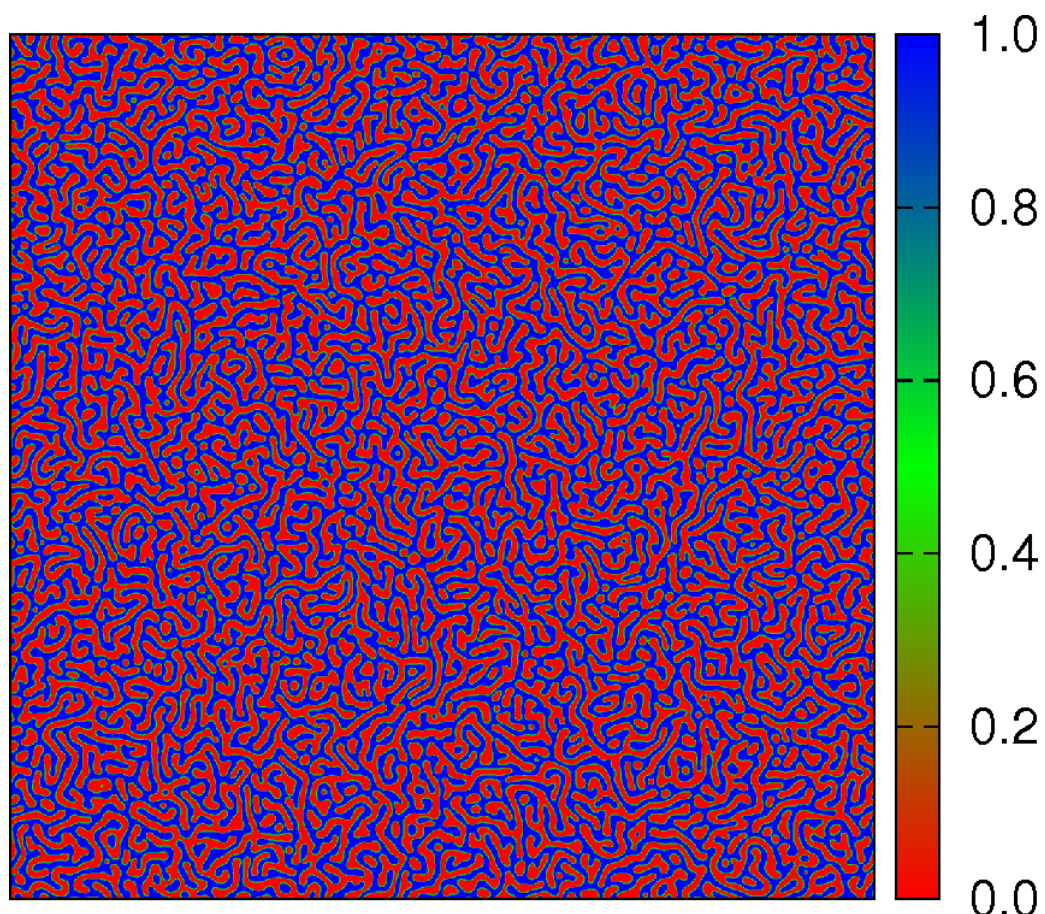


Figure 4.7: BHJ morphology with blend ratio 1:2.5.

4. FORMULATION

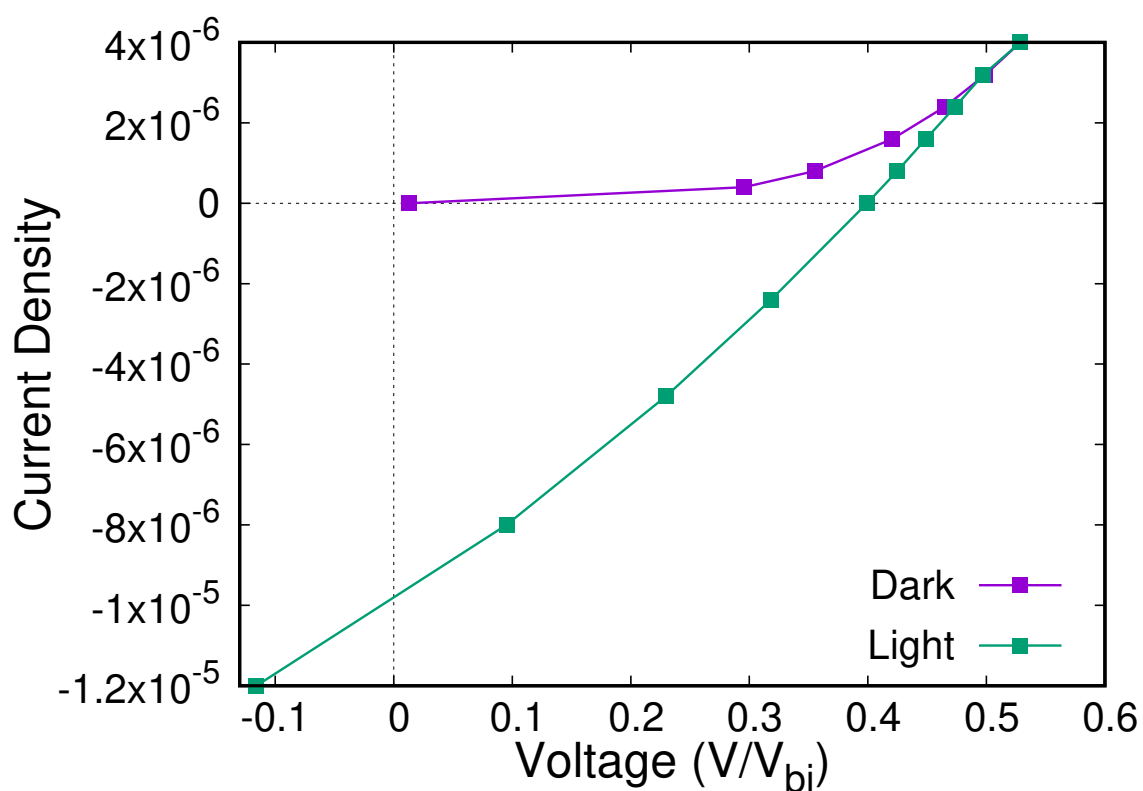


Figure 4.8: Simulation results depicting dark and light J-V characteristics of device with BHJ morphology of active layer.

4. FORMULATION

to decipher the mechanism of phase-transformation in PTB7:PC₇₁BM blend by observing the microstructure of spin-coated films. In order to characterise the underlying microstructure, the authors used Resonant soft X-ray scattering (R-SoXS) coupled with X-ray spectromicroscopy and further substantiated the results using Energy-Filtered Transmission Electron Microscopy (EFTEM) tomography measurements. They found that the spin-coated films primarily consisted of two phases: an amorphous fullerene and PTB7 rich phase formed as a result of spinodal decomposition. However, since the characterisation of dried films cannot completely ascertain the mechanism, Van et al.,[193] carried out in-situ characterisation of morphology during spin-coating for a range of polymer systems using optical techniques. The authors found evaporation induced spinodal decomposition to be responsible for initiating phase-transformation in a variety of polymer-fullerene blends. However, some studies [113, 114] contend that the mechanism of phase-transformation is nucleation and growth based on in-situ studies on drop-cast blends. It is noteworthy to mention that the kinetics of phase-transformation change rapidly (especially for fullerene phase) based on the processing technique and therefore, the mechanism ascertained during drop-casting, and spin-coating differs. In the present study, we have chosen to mimic morphologies arising out of spin-coating instead of drop-casting. Therefore we adopt spinodal decomposition as the mechanism for phase-transformation. Instead, if nucleation and growth is assumed to be the mechanism, then the blend morphology would be more variegated consisting of additional phases other than polymer, fullerene and ternary component rich phases. This is certainly a motivation for a challenging future work.

Second, while we have simulated various microstructures arising from phase-separation pertaining to different blend compositions, the phase-transformation is actually evaporation induced. As the solvent evaporates, the blend composition enters the spinodal regime and then undergoes spinodal decomposition. This constraint will be relaxed in Chapter 7 wherein we investigate the effect of evaporation rate and blend composition on device performance.

Third, in the present study, we have not considered exciton diffusion in our model. This is justified by the fact that the microstructural length scale is comparable to the excitonic diffusion length ($\approx 20\text{ nm}$) and therefore, we have adopted a constant exciton density in the entire morphology. However, this additional feature can be incorporated in a future exercise.

Fourth, while transitioning from the process-structure model to the structure-property model, the morphology was binarised. After that, electronic properties corresponding to pure donor and acceptor phases was ascribed in the bulk phases. While this is a reasonable assumption, the model can be made more realistic by considering phases with semiconducting properties dependent on the phase composition. However, this would require further information on the relation between the blend composition and semiconducting properties. The incorporation of

4. FORMULATION

this additional complexity is certainly an exciting future work and would render more pragmatic insights on the effect of blend composition on photovoltaic properties.

Fifth, in the structure-property model, we have assumed scalar mobility while a tensorial representation leads to a more accurate solution, particularly for situations where there is a large mismatch between the transport coefficients. The basis of this assumption is that the diffusivities of the phases are very similar, which results in insignificant errors due to scalar interpolation of the mobilities. Therefore, in the interest of increasing computational efficiency, we have not adopted the more accurate tensorial interpolation approach. This, however, may be scope for future work.

Chapter 5

Donor-Acceptor OPVs

In this chapter, the novel diffuse interface approach for executing process-structure and structure-property simulations is applied on two-phase OPVs comprising ternary components: P3HT (donor polymer), PCBM (fullerene acceptor) and chlorobenzene solvent. The effect of blend ratio and annealing time on the morphologies simulated using the Cahn-Hilliard formulation described in Section 4.1 is investigated. The photovoltaic properties such as short-circuit current density (J_{sc}), open-circuit potential (V_{oc}), and PCE of the simulated morphologies are then calculated using the structure-property model described in Section 4.2. In order to establish PSP correlations, the simulated morphologies are then characterised by metrics such as interfacial area, percolation fraction and have been correlated with the photovoltaic properties.

5.1 Model parameters

5.1.1 Process-structure relationship

The following set of non-dimensional parameters (see Table 5.1) have been utilized for simulating the microstructures as a result of spinodal decomposition for a ternary system comprising polymer (p), fullerene (f) and solvent (s), while the phase diagram is depicted in Figure 5.1(a). In order to generate a range of morphologies corresponding to compositions that range from

Param	χ_{pf}	$\kappa_{p,f,s}$	A_{aa}	A_{bb}	A_{ab}	N_p	N_f	N_s
Value	0.15	0.1	1.0	1.0	0.3	100	10	1

Table 5.1: Process-Structure model parameter table for Donor-Acceptor system.

P3HT rich to PCBM rich, one particular tie-line in the phase-diagram of P3HT, solvent, and

5. DONOR-ACCEPTOR OPVS

PCBM ternary blend has been chosen (see Fig. 5.1(a)), and morphologies corresponding to various blend ratios of P3HT and PCBM have been generated (see Figs.5.1(b)–5.1(f)).

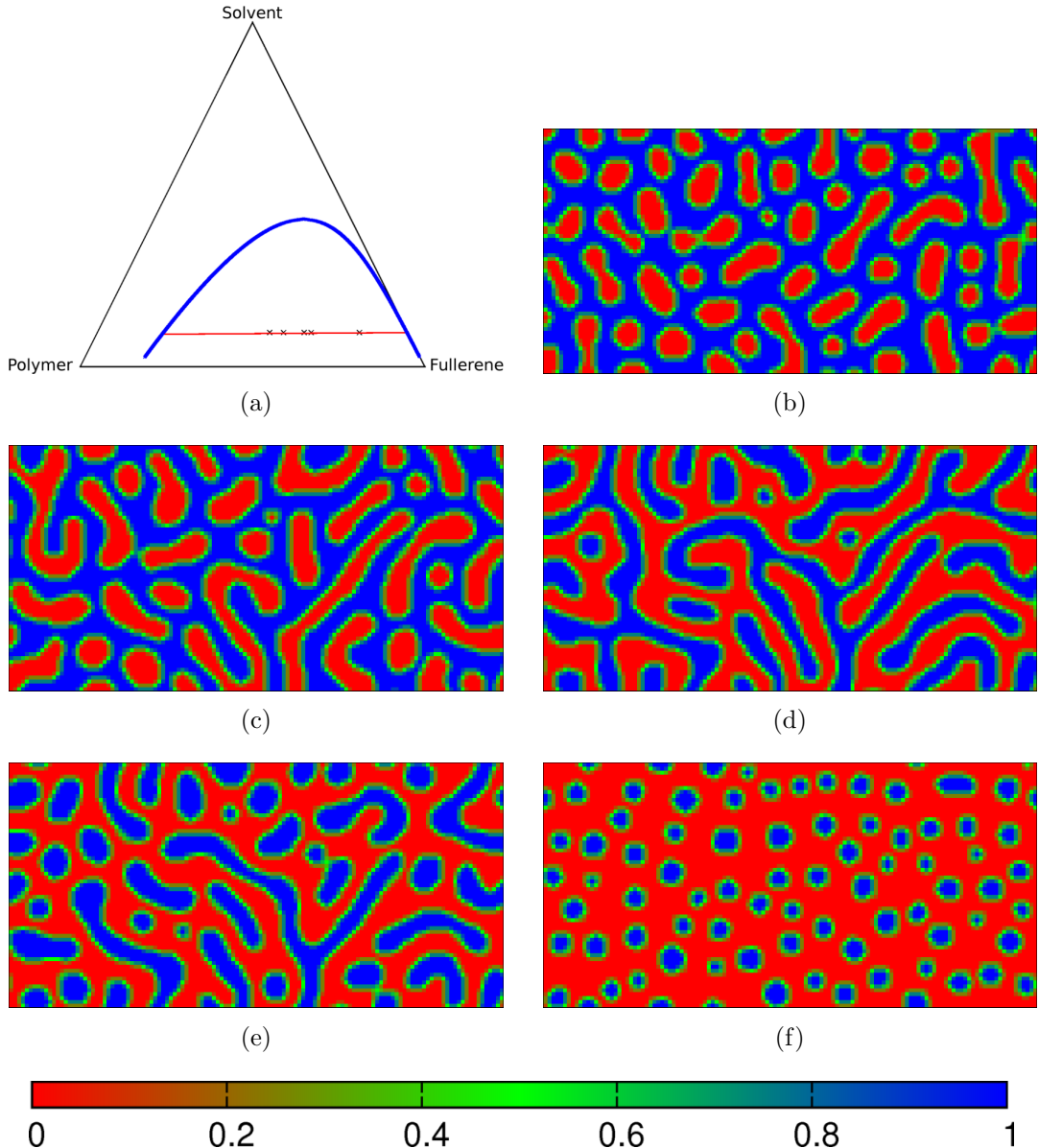


Figure 5.1: (a) Isothermal section of the phase diagram of P3HT, PCBM and CB. BHJ morphology with blend ratio (b) 1:1.25 (c) 1:1.5 (d) 1:2.0 (e) 1:2.2 (f) 1:5.4 On the color bar, 0 corresponds to PCBM rich phase whereas 1 corresponds to P3HT rich phase

5. DONOR-ACCEPTOR OPVS

5.1.2 Structure-property relationship

The formulation adopted for investigating the structure-property relationship is described in Section 4.2. The non-dimensional model parameters that have been used in our simulations are shown in Table 5.2

Parameter	Value
D_e^{P3HT}	10
D_e^{PCBM}	15
D_h^{P3HT}	15
D_h^{PCBM}	10
x_e^{P3HT}	5e-5
x_e^{PCBM}	5e-3
x_h^{P3HT}	5e-3
x_h^{PCBM}	5e-5
G_0	5e-6
N_D	4.95e-3
N_A	4.95e-3
V_{bi}	5
ϵ	1
V_m	1

Table 5.2: Structure-Property model parameter table for Donor-Acceptor OPVs.

5.2 Numerically optimal blend ratio for device fabrication

Since 3D microstructures give a more realistic understanding of the structure-property correlation, the device characteristics for the same were simulated. The 3D microstructures are shown in Fig. 5.2. In order to derive the effect of morphology on device characteristics, the J-V characteristics for the morphologies in Fig. 5.2 were simulated (see Fig. 5.3(a)). Using these characteristics, the Power Conversion Efficiency (PCE) of each device was calculated and the variation of efficiency with the volume fraction of the donor phase can be seen in Fig. 5.3(b).

5. DONOR-ACCEPTOR OPVS

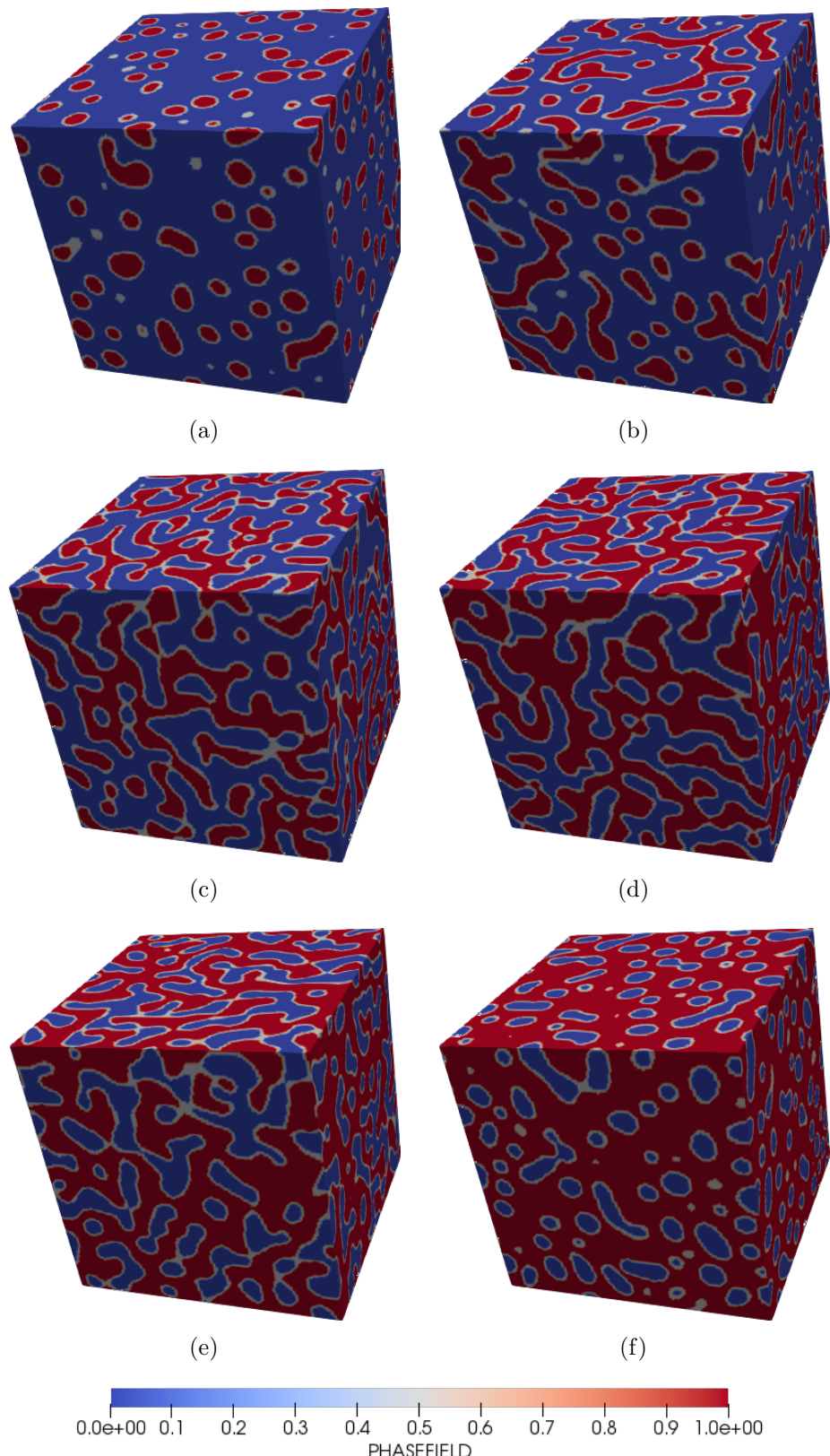
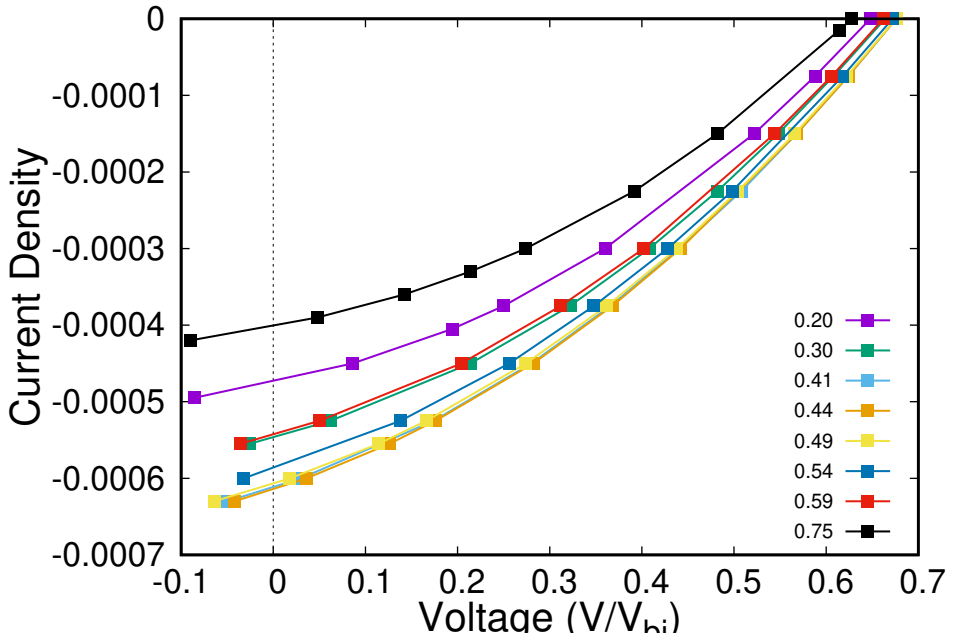
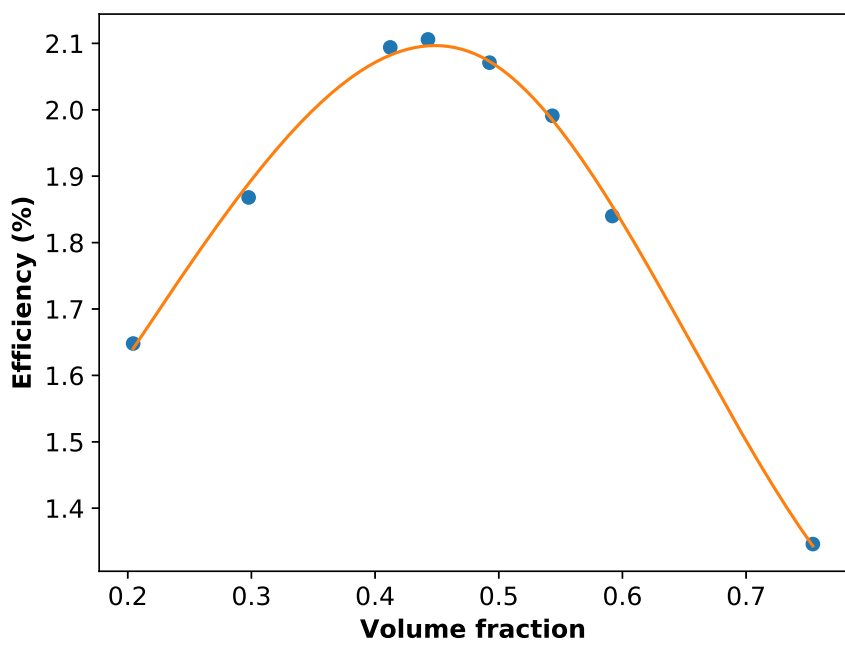


Figure 5.2: BHJ morphology with blend ratio (a) 1:5.4 (b) 1:3.5 (c) 1:2.0 (d) 1:1.5 (e) 1:1.25 (f) 1:0.8

5. DONOR-ACCEPTOR OPVS



(a)



(b)

Figure 5.3: Simulation results depicting (a) J-V characteristics of morphologies with different volume fractions of P3HT (b) efficiency vs volume fraction. Note: The lines have been drawn using spline interpolation just to follow the points and have no physical significance.

5. DONOR-ACCEPTOR OPVS

5.3 Analysis

5.3.1 Effect of blend-ratio

As was explained in the working of OPV, the key to efficient solar cell performance is to maximise exciton dissociation and carrier conduction through the morphology to the respective electrodes. In other words, we would want to maximise the interfacial area (since excitons dissociate at the interface) while having percolating channels to the respective electrodes. In order to investigate the variation of the J_{sc} , V_{oc} , and PCE and derive any possible correlations with changes in the morphology, the interfacial area and percolation of the various simulated microstructures were calculated and compared with their device performance. The percolation of a phase is determined as follows. Firstly, Hoshen-Kopelman algorithm [194] has been employed to identify clusters corresponding to the phases in the morphology. Secondly, among the identified clusters corresponding to a phase, those percolating the morphology in the direction of electrodes are screened out. Subsequently, percolation fraction is calculated by first computing the volume of the percolating clusters of a given phase (V_α^{pc}) divided by the total volume of the clusters of that phase ($\sum_c V_\alpha^c$), where V_α^c is the volume of any α phase cluster. Thus, two different fractions will be derived for the two phases. The percolation fraction of the morphology is thereafter derived by summing these individual fractions and dividing them by the total number of phases as shown below,

$$P = \frac{1}{2} \sum_{\alpha}^{N=2} \frac{V_\alpha^{pc}}{\sum_c V_\alpha^c}, \quad (5.1)$$

where P denotes the percolation fraction of the morphology. A higher connectivity/percolation fraction will lead to an improved PCE. Quantitatively, if either the p-type (donor) or n-type (acceptor) semiconductor is completely percolating, the percolation fraction would be 0.5. In contrast, if both the semiconductors are completely percolating, the percolation fraction would be 1. The device performance of semi-percolating morphologies, i.e., either P3HT rich (volume fraction - 0.75) or PCBM rich (volume fraction - 0.20) is found to be poor (volume fractions are of P3HT). All other morphologies are bi-continuous, thereby implying that the device performance is controlled by exciton dissociation. This is precisely what is observed, i.e., J_{sc} and V_{oc} for different morphologies follows the same trend as that of the interfacial area (see Fig. 5.4). It can be noted here that the variation in V_{oc} is relatively small, as is observed experimentally in organic photovoltaics. The correlation in the trend can be explained by the fact that since

5. DONOR-ACCEPTOR OPVS

the morphologies corresponding to the volume fraction of 0.30, 0.41, 0.44, 0.49, 0.54, 0.59 are completely percolating, charge carrier conduction to electrodes will not be a limiting factor; therefore, if the interfacial area increases, the generation of carriers becomes larger, resulting in a higher J_{sc} and V_{oc} .

5.3.2 Effect of Annealing

It was experimentally observed that initially during annealing, J_{sc} increases and then decreases, thus resulting in an optimal annealing time (see Fig. 3.3(d)). The initial increase in J_{sc} corresponds to the existence of a better interface between the electrode and active layer due to post-production annealing of the device [195]. The improvement in the interface is evident from the fact that there is an enhancement in the fill factor. Better interface naturally leads to an enhancement in carrier collection at the electrodes. The reduction in J_{sc} upon further annealing stems from coarsening of the morphology, resulting in lower exciton dissociation. The simulation results indicate that as the morphology is annealed, due to coarsening (resulting in lower interfacial area), the J_{sc} decreases (see Fig. 5.5).

5.4 Summary

In this work, we have for the first time developed a diffuse-interface framework for deriving both the structure-property and process-structure relationships, that provides for an elegant methodology for deriving PSP linkages. The theoretical PSP linkage in OPVs was established, and we were able to get guidelines on the processing parameters for optimising BHJ morphology and subsequently, electronic properties. This linkage is found to be in qualitative agreement with our experimental results. We find that the necessary condition for fabricating an efficient OPV device is the existence of a bi-continuous network of donor and acceptor phases as this leads to percolating channels for electrons and holes to their respective electrodes. Amongst the percolating morphologies, the ones with a higher interfacial area lead to higher short circuit current density (J_{sc}) and eventually to higher efficiency since the open-circuit potential (V_{oc}) is a weak function of the morphology. Therefore, the key to an efficient solar cell is the optimisation of the two critical processes involved in the working mechanism of OPV, i.e., exciton dissociation and carrier conduction through the morphology to the respective electrodes. The interfacial area governs exciton dissociation. Efficient carrier conduction results from the transportation of the electron and hole to their respective electrode via a well-connected network of phases with minimal leakage of current and recombination of charge carriers. Hence, efficient carrier

5. DONOR-ACCEPTOR OPVS

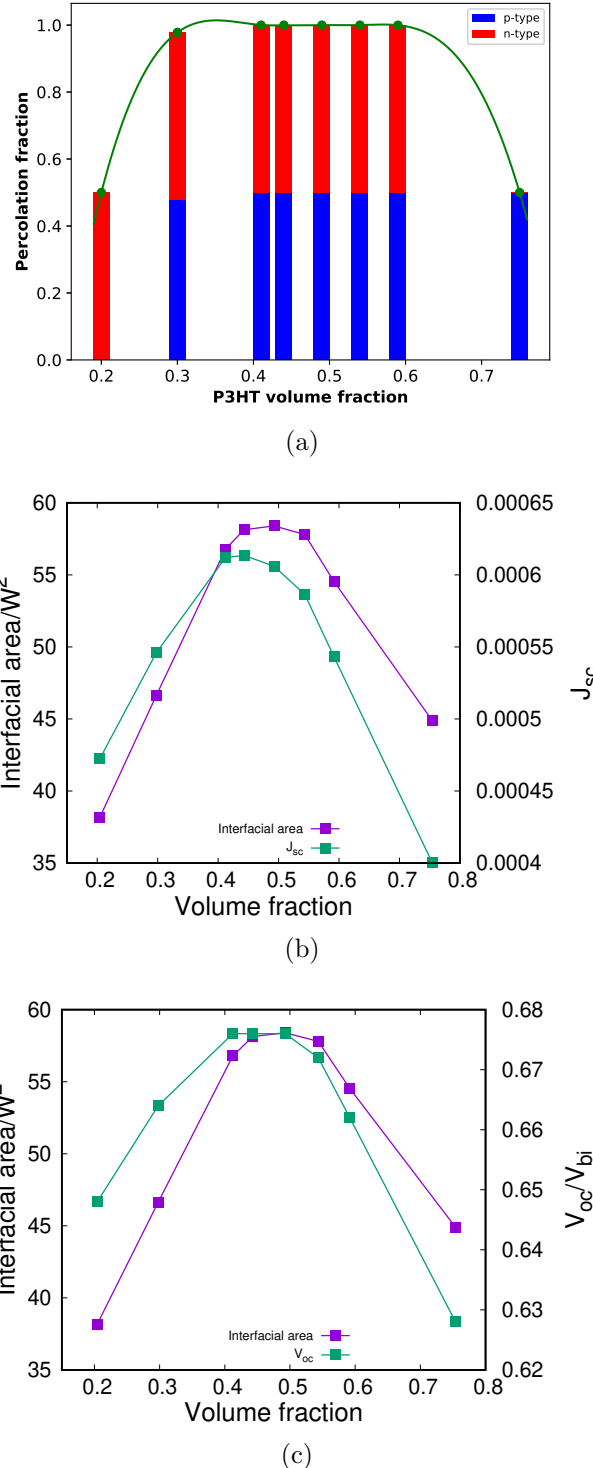


Figure 5.4: Simulation results depicting (a) percolation fraction vs volume fraction (b) J_{sc} and interfacial area vs volume fraction (c) V_{oc} and interfacial area vs volume fraction. Note: The lines have been drawn using spline interpolation just to follow the points and have no physical significance.

5. DONOR-ACCEPTOR OPVS

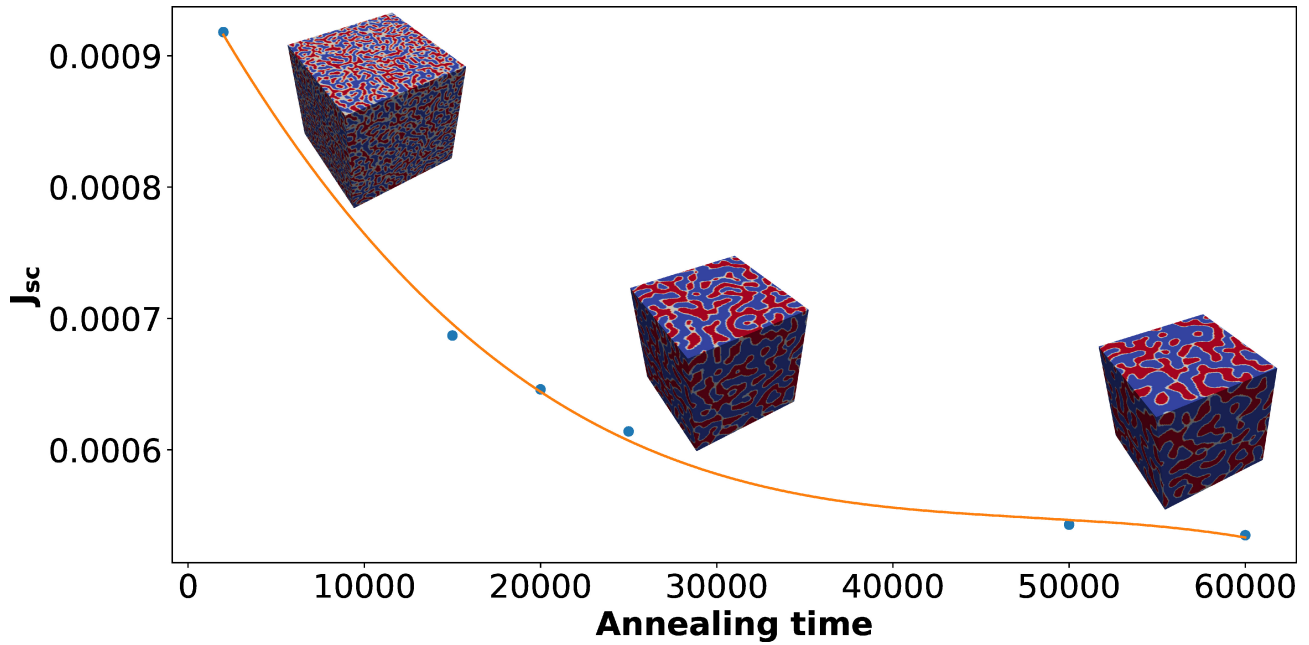


Figure 5.5: Simulation results depicting the effect of annealing on J_{sc} . Note: The lines have been drawn using spline interpolation just to follow the points and have no physical significance.

conduction is governed by a higher percolation fraction of the morphology. Another essential step during device fabrication is annealing the device after production. It is experimentally observed that initially during annealing, J_{sc} increases and then decreases, thus resulting in an optimal anneal time. The initial increase in J_{sc} corresponds to the existence of a better interface between the electrode and the active layer. The reduction in J_{sc} stems from the coarsening of morphology, resulting in lower exciton dissociation that has been verified numerically in the simulations.

Chapter 6

Donor-Acceptor-Acceptor OPVs

In this chapter, we model the PSP relationship in state-of-the-art ternary OPVs comprising a polymer, fullerene and ternary acceptor. Herein, we derive process-structure correlations using phase-field simulations based on the Cahn-Hilliard formalism, for modeling phase-separation in ternary systems where a third component that acts as an acceptor is added to a binary OPV. This leads to structures that can be classified as Donor-Acceptor-Acceptor (DAA). In order to derive the structure-property correlations for the three-phase simulated microstructures (comprising the active layer of the OPV device), we employ the diffuse-interface approach. Using the above approach, we determine the electronic properties such as efficiency, fill-factor, short-circuit current, and open-circuit voltage. Further, in order to expedite the theoretical prediction, a robust and elegant data analytics model is built using dimensionality reduction techniques.

6.1 Model parameters

6.1.1 Process-structure relationship

The formulation used for executing process-structure simulations is described in Section 4.1. It is noteworthy to mention that while processing a ternary OPV blend (comprising donors and acceptors), a solvent is necessary to blend the ternary components. This results in a quarternary blend comprising donors, acceptors, and the solvent. However, in the present study, we have considered a ternary blend comprising the donors and acceptors for simplification. Consequently, the process-structure-property analysis is performed along an iso-concentration section for the solvent molecules. The parameters used in Flory-Huggins bulk free energy density as well as the mobilities for polymer (p), fullerene (f) and ternary (t) components are

6. DONOR-ACCEPTOR-ACCEPTOR OPVS

mentioned in the following Table 6.1, while the resulting isothermal section of phase-diagram is plotted in Figure 6.1(a).

The curves shown in Figure 6.1(a) within the Gibbs triangle correspond to the two-phase binodals (polymer-fullerene, fullerene-ternary and ternary-polymer). A range of morphologies spanning the coexistent three-phase spinodal region within the union of these two-phase binodals has been generated (see Figure 6.1(a)), where the compositions for which the simulations have been performed are highlighted in Figure 6.1(a). The choice of this region is made with the objective of generating various three-phase morphologies pertaining to the DAA system.

Parameter	χ_{pf}	χ_{ft}	χ_{pt}	$\kappa_{p,f,t}$	Λ_{aa}	Λ_{bb}	Λ_{ab}	N_p	N_f	N_t
Value	3	3	3	1	1.0	1.0	0.3	5	1	1

Table 6.1: Process-Structure model parameter table for Donor-Acceptor-Acceptor system.

6.1.2 Structure-property relationship

The structure-property simulations for DAA system are initialised with the non-dimensional parameters listed in Table 6.3. In this work, two species (electron and hole) and three phases (polymer, fullerene and ternary acceptor) have been considered, therefore, we have 6 unknown Fermi-levels provided polymer-fullerene and polymer-ternary phase built-in potentials (V_{bi}^{pf} and V_{bi}^{pt}) are specified, which are assumed in this model for adjusting the difference in the Fermi levels. The built-in potentials have been chosen such that a cascaded alignment of Fermi levels is obtained, with the Fermi-level of ternary phase intermediate to donor and fullerene phases. The fullerene Fermi-levels ($E_e^{Fullerene}$ and $E_h^{Fullerene}$) have been pinned to zero and the remaining 4 unknown Fermi-levels ($E_e^{Polymer}$, $E_e^{Ternary}$, $E_h^{Polymer}$ and $E_h^{Ternary}$) have been derived by solving,

$$\begin{aligned}
 \tilde{\mu}_e^{Polymer} &= \tilde{\mu}_e^{Fullerene} \\
 \tilde{\mu}_e^{Ternary} &= \tilde{\mu}_e^{Polymer} \\
 \tilde{\mu}_h^{Polymer} &= \tilde{\mu}_h^{Fullerene} \\
 \tilde{\mu}_h^{Ternary} &= \tilde{\mu}_h^{Polymer}.
 \end{aligned} \tag{6.1}$$

The calculation of Fermi levels is shown in Appendix B and their values are tabulated in Table 6.2.

6. DONOR-ACCEPTOR-ACCEPTOR OPVS

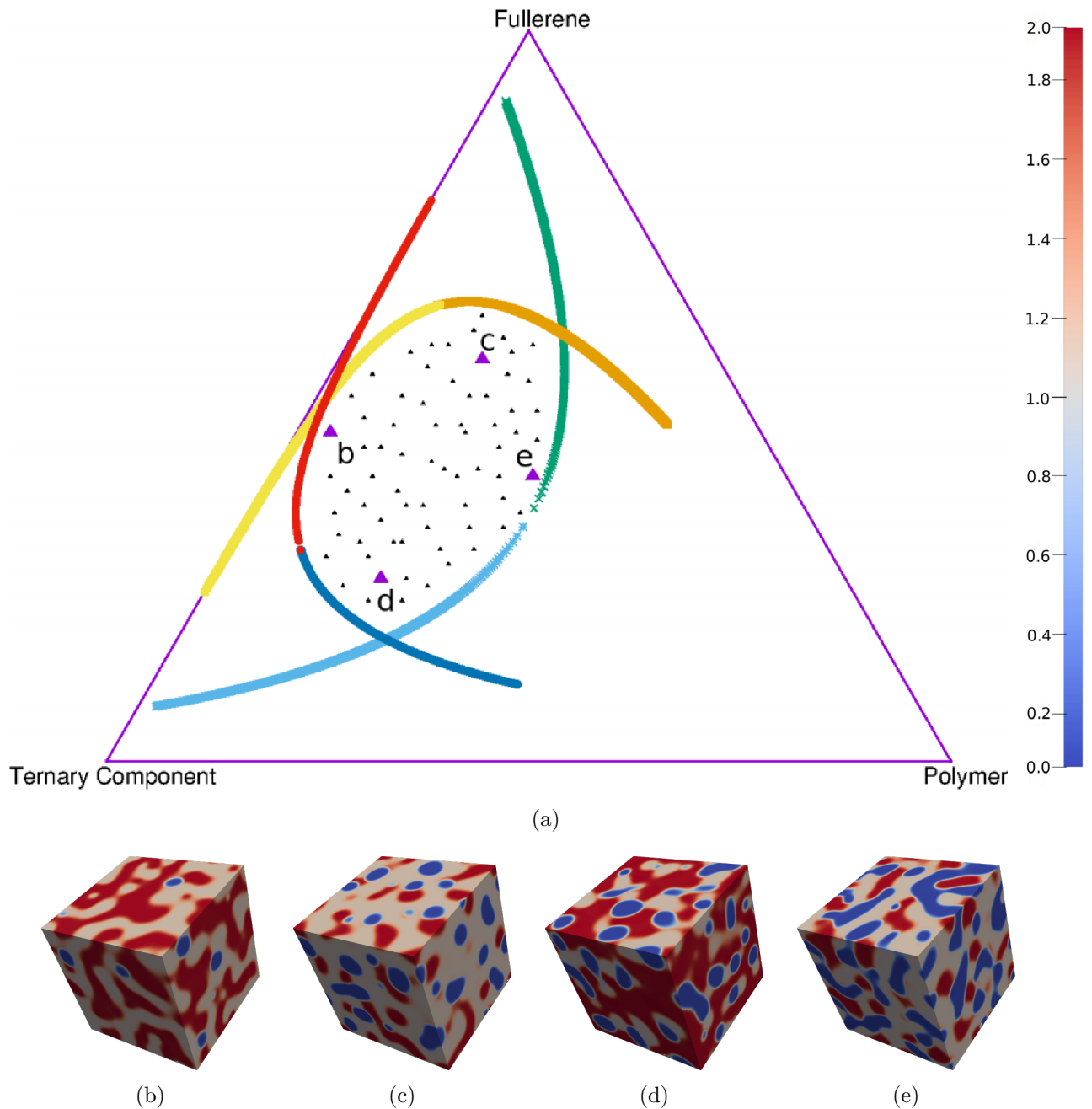


Figure 6.1: (a) Isothermal section of the phase diagram for polymer, fullerene and ternary component. BHJ morphologies with volume fraction of polymer, fullerene and ternary component (b) 0.04:0.45:0.51 (c) 0.17:0.55:0.28 (d) 0.20:0.25:0.55 (e) 0.31:0.39:0.30 On the color bar, 0 corresponds to polymer rich phase, 1 corresponds to fullerene rich phase and 2 corresponds to ternary component rich phase

6. DONOR-ACCEPTOR-ACCEPTOR OPVS

Fermi energy	Value
$E_e^{Polymer}$	-0.4
$E_e^{Ternary}$	-0.2
$E_e^{Fullerene}$	0
$E_h^{Polymer}$	0.4
$E_h^{Ternary}$	0.2
$E_h^{Fullerene}$	0

Table 6.2: Fermi energy levels of electron and hole for polymer, fullerene and ternary component rich phases.

In the next section, we explore the results obtained using the PSP simulation framework described in this section.

6.2 Results

The current-voltage characteristics of devices with the morphologies corresponding to the simplex shown in Figure 6.1(a) were simulated using the diffuse interface structure-property model. The device simulations were done for the DAA system wherein the ternary component is an acceptor. The simulated J-V curve for the device with one of the morphologies corresponding to blend composition- 0.32:0.34:0.34 is shown in Figure 6.2.

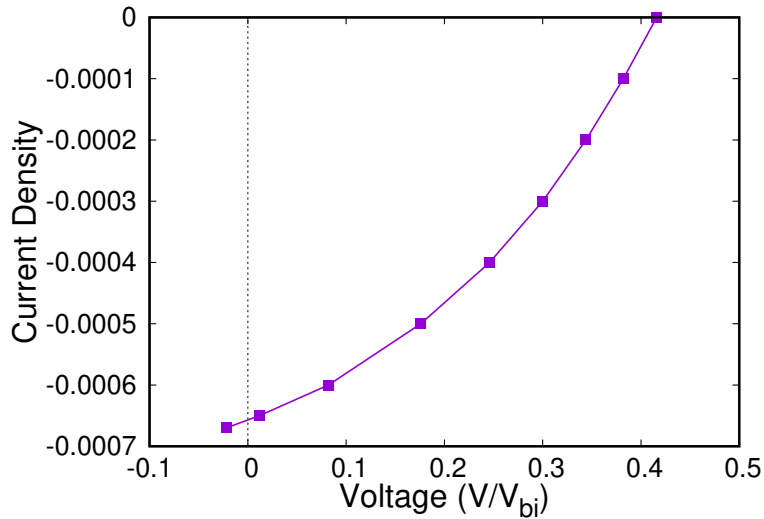


Figure 6.2: Simulated J-V characteristics of a device with blend composition 0.32:0.34:0.34. These characteristics have been further processed to extract photovoltaic parameters i.e., J_{sc} , V_{oc} and FF .

6. DONOR-ACCEPTOR-ACCEPTOR OPVS

Parameter	Value
$D_e^{Polymer}$	10
$D_e^{Fullerene}$	15
$D_e^{Ternary}$	15
$D_h^{Polymer}$	15
$D_h^{Fullerene}$	10
$D_h^{Ternary}$	10
$x_e^{Polymer}$	5e-5
$x_e^{Fullerene}$	5e-3
$x_e^{Ternary}$	5e-3
$x_h^{Polymer}$	5e-3
$x_h^{Fullerene}$	5e-5
$x_h^{Ternary}$	5e-5
N_D	4.95e-3
N_A	4.95e-3
G_0	3e-7
V_{bi}^{pf}	5.0
V_{bi}^{pt}	4.8
ϵ	1
V_m	1

Table 6.3: Structure-Property model parameter table for DAA system.

Before we embark upon the comparison between the PCE of the different morphologies, it is important first to characterize the variation of the PCEs with phase decomposition time, as the PCE is bound to be a function of both the extent of phase decomposition as well as the blend composition. For this, we compared two representative composition blends (0.25:0.43:0.32) and (0.14:0.42:0.44), where the variation of the efficiency as a function of phase decomposition time is plotted in Figure 6.4(a). We see that for both compositions, the PCE saturates beyond a certain time. The changes in the PCE at earlier times occur as a result of the rapid microstructural changes. In order to correlate the PCE with the change in the microstructure, we have chosen a set of microstructural descriptors which have a natural influence on the PCE. For example, the interface area naturally correlates with the generation of carriers, and a higher value would result in a larger short circuit current J_{sc} and thereby increased efficiency. Similarly, two other descriptors are the percolation fraction and tortuosity. Quantitatively, a percolation fraction ≥ 0.66 represents tri-percolating morphologies (wherein all the polymer donor, fullerene acceptor and ternary acceptor phases are percolating), the morphologies with percolation fraction between 0.33 and 0.66 are bi-percolating (wherein two of the phases are percolating), and the

6. DONOR-ACCEPTOR-ACCEPTOR OPVS

mono-percolating morphologies are the ones with percolation fraction ≤ 0.33 . The percolation fraction, therefore, delivers a measure of the extent of through connectivity between the electrodes. While percolation fraction quantifies the existence of available pathways for the carriers that are generated, however, we use an additional descriptor that quantifies the effective resistivity of the system, which is captured by the length of the available pathways. We classify this as the effective tortuosity τ_e , which is calculated as,

$$\frac{1}{\tau_e} = \sum_{\alpha}^{N=3} \frac{\phi'_{\alpha}}{\tau_e^{\alpha}}, \quad (6.2)$$

where $\tau_e^{\alpha} = \frac{l^{\alpha}}{n_{perc}^{\alpha} l_s}$, with l^{α} is the total length of the percolating clusters of a phase α , n_{perc}^{α} the number of percolating clusters of α , l_s shortest path between the two electrodes and ϕ'_{α} is the volume fraction of the percolating clusters that belong to phase α . Since the percolating clusters do not follow a straight line and instead take a curved path, the length of the percolating cluster has been calculated as follows: the electrodes are along Y-direction, therefore, we start at Y=1, find the centroid of the percolating cluster along the corresponding XZ plane, then for Y=2, we go to the corresponding XZ plane and calculate the centroid of the cluster. This exercise is continued until we approach Y=128, which is the domain size of morphology. Finally, the distance between the centroids of the clusters from Y=1 to Y=128 by summing over the discrete line segments joining the centroids, rendering the percolation lengths as shown in Fig.6.3.

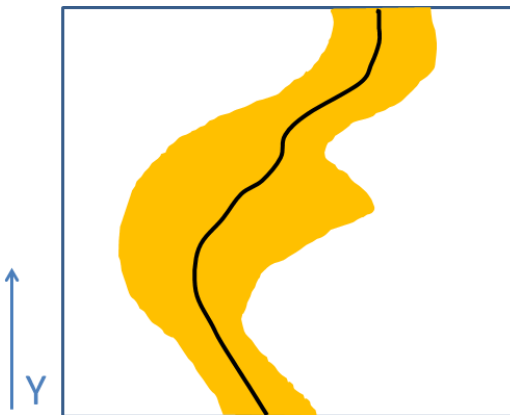


Figure 6.3: Schematic depicting the calculation of the length of the percolating cluster. In yellow is shown the percolating cluster and the black line represents the path traced by the centroid of the cluster at each XZ plane.

Figure 6.4(c) plots the percolation fraction, while the effective tortuosity and interface area is depicted in Figures 6.4(d) and 6.4(b) respectively for the two blend compositions mentioned

6. DONOR-ACCEPTOR-ACCEPTOR OPVS

above. The blend composition (0.25:0.43:0.32) corresponds to a tri-percolating morphology whereas the composition (0.14:0.42:0.44) is a bi-percolating morphology. It can be noted that all the microstructural descriptors saturate with time. The efficiency follows the same trend

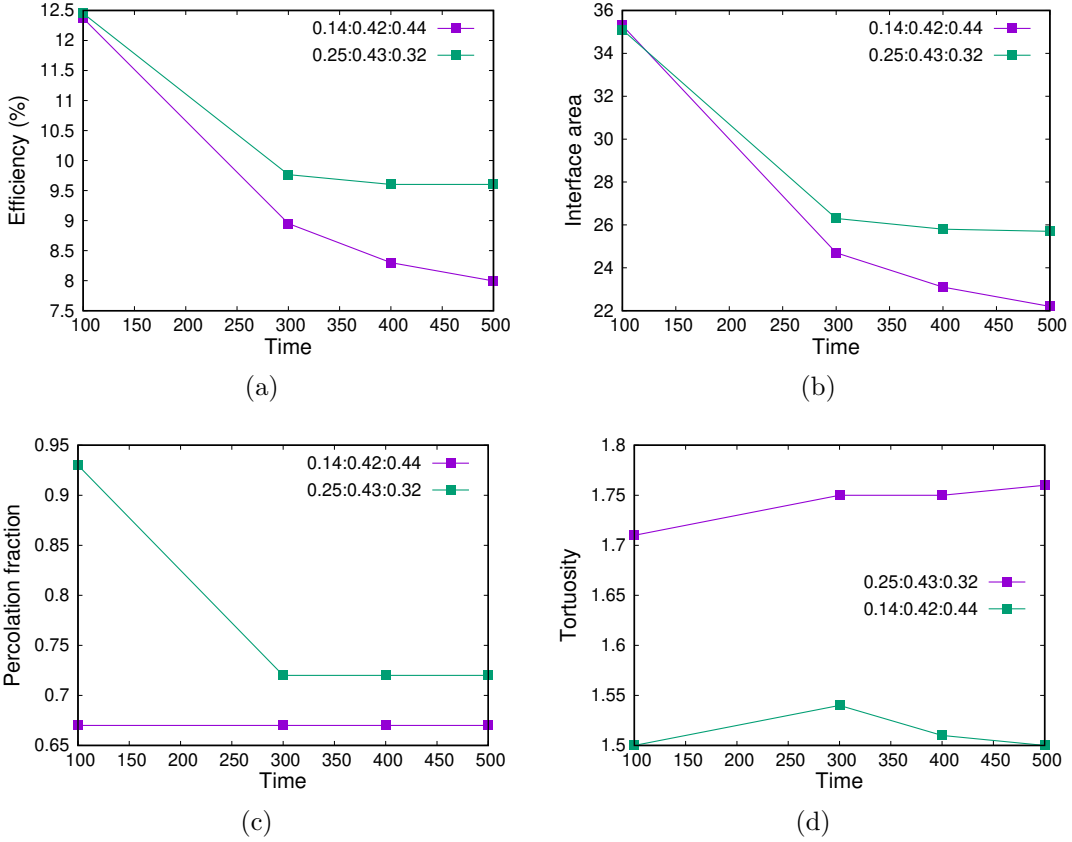


Figure 6.4: Simulation results depicting the variation of (a) efficiency (PCE), (b) total interface area, (c) percolation fraction and (d) tortuosity with time.

as that of the microstructural descriptors, i.e., interfacial area and percolation fraction. Since the blend composition (0.25:0.43:0.32) has a higher percolation fraction and interfacial area, it exhibits higher PCE. The range of variation of tortuosity seems to be too narrow for affecting a significant impact on the efficiency of the device. Further, we note that a wide variation of the device performance with microstructural evolution is certainly something that is not desirable and thereby in the next sections, we compare microstructures that are near stationary with respect to the efficiency and the microstructural descriptors. We find this stage is approximately reached uniformly across all microstructures for simulation times greater than 400 and thereby all of the further analysis that compares the performance of the devices with composition is performed for a simulation time of 500.

6. DONOR-ACCEPTOR-ACCEPTOR OPVS

Structure-property calculations were performed for 30 out of the 70 morphologies that have been simulated using the process-structure model shown in Figure 6.1(a), by initializing electronic properties corresponding to the DAA system according to Table 6.3. The morphologies for doing structure-property simulations have been chosen such that the trends in the variation of efficiency with morphology are sufficiently captured. The PCE of these devices is shown in Figure 6.5(a). It can be observed that morphologies pertaining to particular regions within this simplex perform better than others. In order to understand the reason behind some morphologies outperforming others in terms of PCE, we further characterized these morphologies for identifying the different percolating natures (mono, bi and tri percolating), tortuosities and total interface area (representative of the extent of exciton dissociation) to determine the effect of these descriptors on efficiency as shown in Figure 6.5. It can be observed in Figure 6.5(c) that the tri-percolating morphologies are located on the centre of the simplex, the bi-percolating morphologies are situated closer to fullerene-ternary, ternary-polymer and polymer-fullerene binary edge whereas the mono-percolating morphologies lie closer to fullerene and ternary vertex. We found that the champion device with PCE of 10% corresponded to a tri-percolating morphology with a percolation fraction of 1.0. The morphology of the DAA device exhibiting highest and lowest efficiency is shown in Figure 6.6. It can be inferred from the structure-property calculations that percolation fraction and interface area have a strong influence upon the power conversion efficiency. Therefore, the blends corresponding to tri-percolating morphologies along with higher interfacial area outperform others. Among these two morphological descriptors (i.e., interface area and percolation fraction), it can be noted that interfacial area has a higher correlation with efficiency since bi-percolating morphologies with the lower interfacial area have lower efficiencies than mono-percolating morphologies with the relatively higher interfacial area. The influence of tortuosity on PCE cannot be directly ascertained and seems to have a complicated relationship with efficiency.

Since, the efficiency is also dependent on the related electronic properties such as the short-circuit (J_{sc}), open-circuit potential (V_{oc}) and the fill-factor (FF) it is quite instructive to follow their variation with the microstructures in the simplex, which is plotted in Figure 6.7. We see that there is a clear correlation between the variation of the interfacial area in Figure 6.5(b) and the short-circuit current, J_{sc} in Figure 6.7(a) and the open-circuit potential in Figure 6.7(c). The correlation of the fill-factor with the microstructural features is less trivial. It appears that for tri-percolating morphologies, the tortuosity has a correlation with the fill-factor whereas, for lower percolating microstructures (for example towards the fullerene-ternary component edge of the simplex), it is the percolation fraction that correlates well with the fill-factor. However, the relative change in the fill-factor across the composition space is minor ($\approx 4\%$) compared to the

6. DONOR-ACCEPTOR-ACCEPTOR OPVS

J_{sc} ($\approx 30\%$) and the V_{oc} ($\approx 8\%$). So, it is the relative change in these two latter characteristics with the microstructural changes that principally reflects in the influence on the PCE.

These results further underline the complex interplay of various morphological factors on device performance. While, in the preceding analysis, the variation of the few geometric descriptors of the microstructure has been used to correlate with device performance, in the following, we adopt a statistical description of the microstructures using spatial correlations and utilize dimensionality reduction techniques in order to relate the device performance and the microstructure. Thus using quantitative PSP correlations, we further search the composition space for determining for the most efficient device as well as the corresponding morphology.

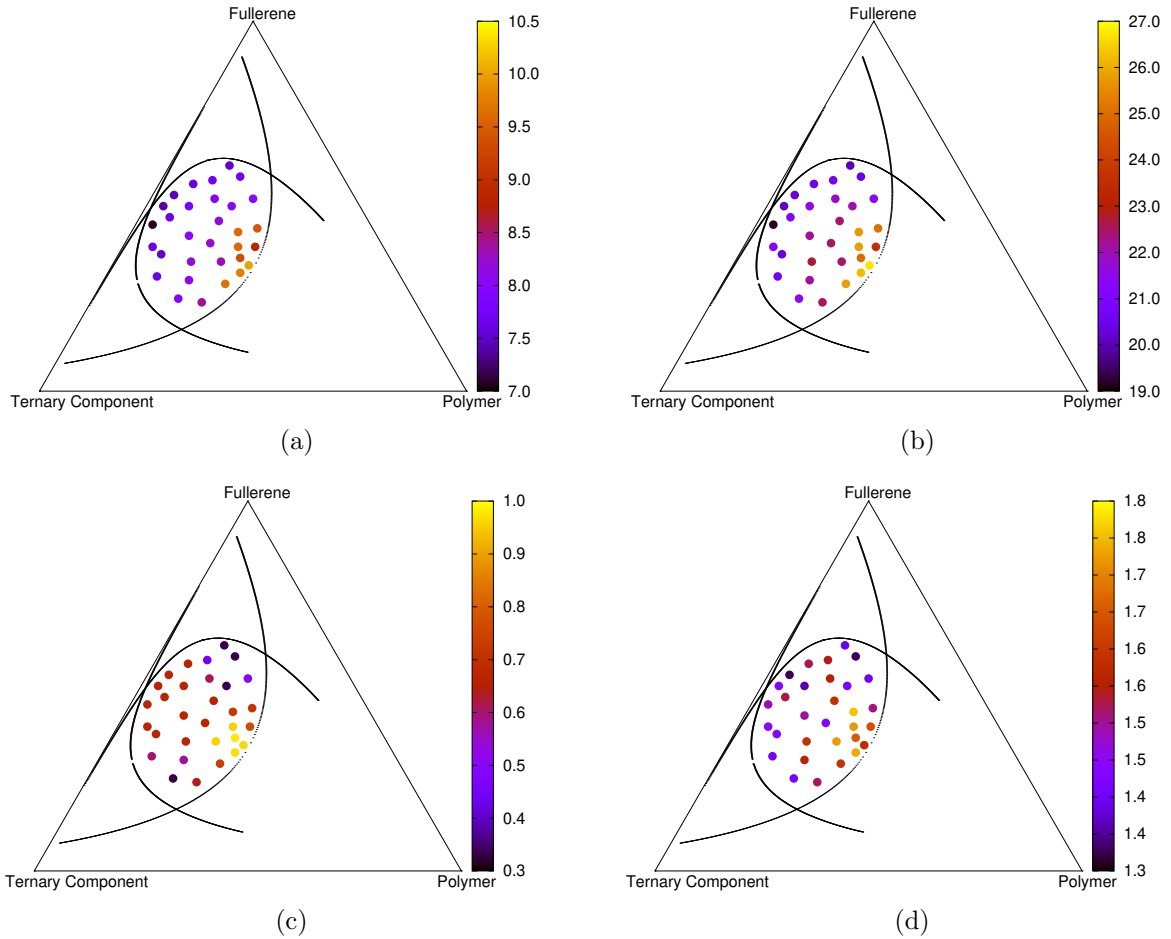


Figure 6.5: (a) Efficiency, (b) total interface area, (c) percolation fraction and (d) tortuosity maps on simplex depicting the variation of PCE and morphological descriptors with blend ratio as obtained using simulations. The tri-percolating morphologies have been found to exhibit highest efficiencies.

6. DONOR-ACCEPTOR-ACCEPTOR OPVS

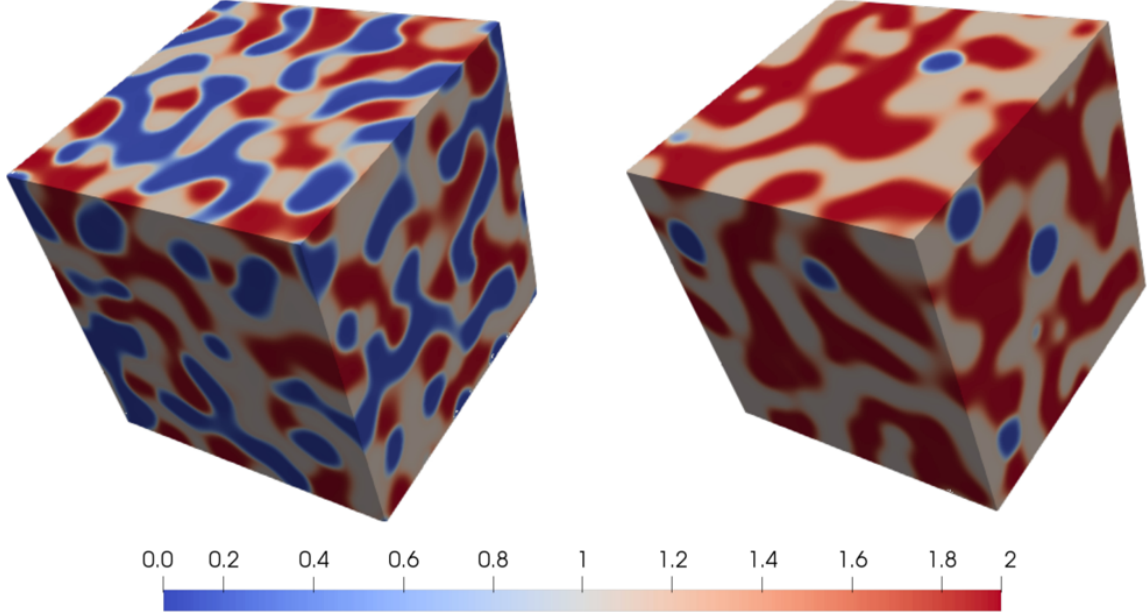


Figure 6.6: Morphology of device exhibiting highest efficiency (blend composition: 0.32:0.34:0.34) on the left and lowest efficiency (blend composition: 0.04:0.45:0.51) on the right for DAA system. On the color bar, 0 corresponds to polymer rich phase, 1 corresponds to fullerene rich phase and 2 corresponds to ternary component rich phase.

6.3 Quantitative Microstructure Characterization

The simulated microstructures in the previous section span a generous portion of the ternary spinodal, as shown in Figure 6.1(a). The properties of interest like the current density J_{sc} and the efficiency η depends primarily upon the microstructure. For a given blend ratio, the microstructure generation and the subsequent electronic property simulation is computationally expensive and take days to complete on high-performance clusters. This necessitates us to derive a quantitative model using the simulated data to predict electronic properties without the need for running additional simulations for intermediate blend ratios. Thus, in order to create numerical correlations between structure and the property of interest, one has to represent the microstructure quantitatively [3]. This mathematical representation of the microstructure is facilitated by using spatial 2-point correlation maps of the phases [4, 5, 6, 7]. The vectorised 2-point correlation map is further reduced by using Principal Component Analysis (PCA) to concisely capture the features that show maximum variance in the dataset [8, 9, 10].

The dataset selected for our analyses are the coarsened microstructures with various blend ratios for DAA system. For comprehensively representing the 3 phase microstructure, we take the self-correlation between phase 1 and the cross-correlation between phases 1 and 2 as the in-

6. DONOR-ACCEPTOR-ACCEPTOR OPVS

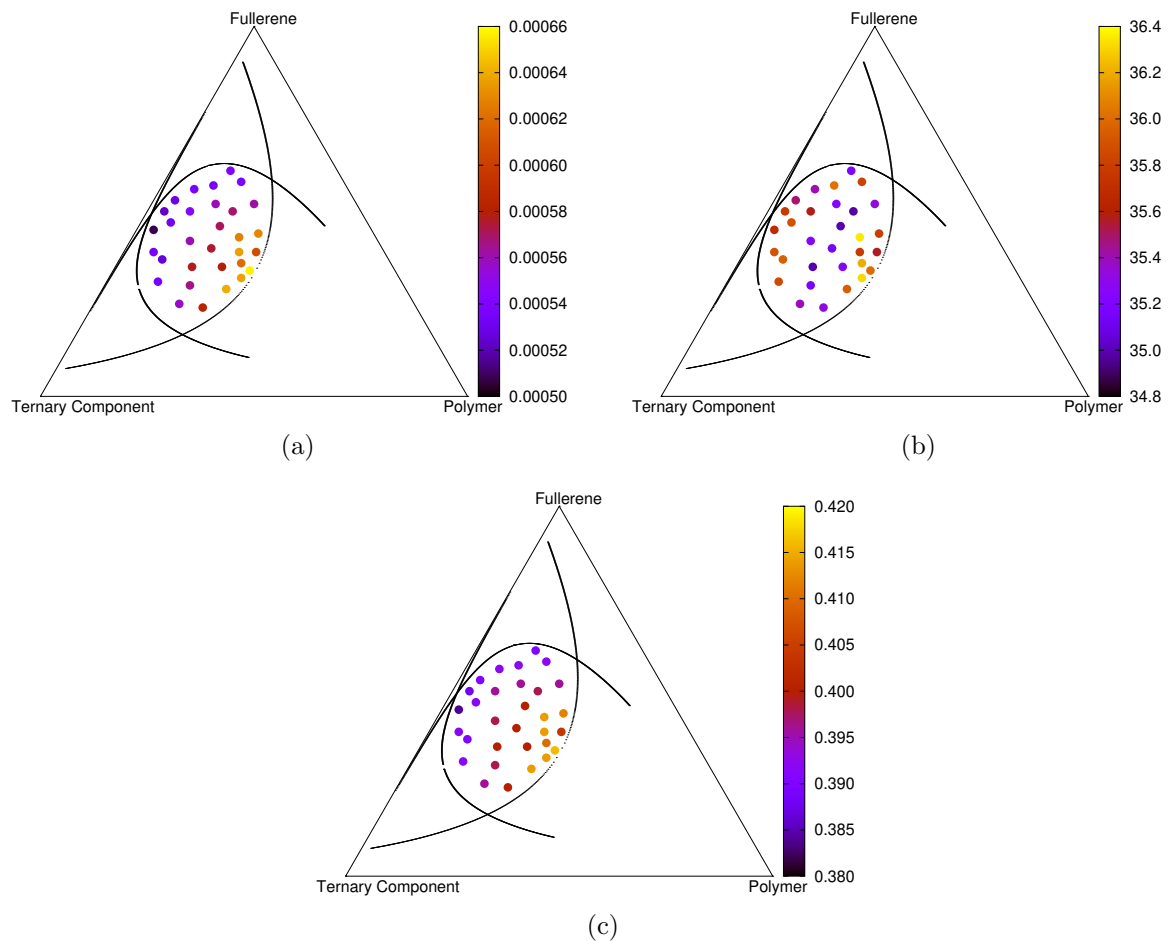


Figure 6.7: Maps of photovoltaic parameters (a) J_{sc} , (b) FF and (c) V_{oc} extracted from the simulation data on simplex depicting their variation as a function of blend composition.

6. DONOR-ACCEPTOR-ACCEPTOR OPVS

dependent ones to describe the microstructure. Upon dimensional reduction of the correlations using PCA, the top two Principal Component (PC) vectors explain $\approx 95\% = (57\% + 38\%)$ respectively of the variance in the dataset.

In order to expedite the prediction of process-structure relationship, we fitted the PC 's with respect to the volume fractions of polymer donor and fullerene acceptor. The idea is to minimise the number of process-structure simulations required to achieve the optimal blend ratio. A second degree polynomial in ϕ_p and ϕ_f , given by $PC_i(\phi_p, \phi_f) = (p00)^i + (p10)^i(\phi_p) + (p01)^i(\phi_f) + (p20)^i(\phi_p^2) + (p11)^i(\phi_p\phi_f) + (p02)^i(\phi_f^2)$ has been employed. The fits of PC_0 , PC_1 and PC_2 are shown in Figure 6.8 with $r^2 \approx 0.994$, $r^2 \approx 0.998$ and $r^2 \approx 0.85$ respectively. The coefficients used in the fitting equation are shown in Table 6.4.

Coefficient	$p00$	$p10$	$p01$	$p20$	$p11$	$p02$
PC_0	-1679	7390	2420	-5619	-1.068e+04	1813
PC_1	3281	-7086	-1.321e+04	3552	1.386e+04	1.281e+04
PC_2	74.02	-369.3	-94.12	197.9	346.4	30.16

Table 6.4: Coefficients of the second order equation fitting PC.

We build a multivariable linear regression model to predict the current density J_{sc} and efficiency η from the PC scores for the DAA system. The mathematical relation describing the linear regression of J_{sc} is given by: $J_{sc} = a_1(\phi_p) + b_1(PC_1) + c_1(PC_2) + d_1$ and that of η is given by: $\eta = a_2(\phi_p) + b_2(PC_1) + c_2(PC_2) + d_2$. Table 6.5 lists the coefficients of the multivariable linear regression equation. The predicted vs actual plot is shown in Figure 6.9 with an $r^2 \approx 0.93$ for J_{sc} and $r^2 \approx 0.88$ for η respectively considering only ϕ_p , PC_1 and PC_2 as the independent variables. Also evident is the decreasing trend of J_{sc} and η with increasing PC_1 and PC_2 values in Figure 6.10. This strong dependence is expected as the PC_1 , and subsequent higher components ($2, 3, \dots$) predominantly capture microstructural intricacies which makes the microstructures distinct, whereas PC_0 represents essential features which are uniform across the microstructures. Thus, whereas PC_0 strongly represented the microstructure (explained variance $\approx 57\%$), its contribution in capturing a derived microstructural property like J_{sc} is negligible.

Moreover, in Figure 6.10, we have classified the microstructures depending upon the number of spatially connected phases as mono-percolating, bi-percolating and tri-percolating. We observe clustering of the microstructures into three regions in the $PC_1 - PC_2$ space: mono-percolating with the least J_{sc} and η to the right, bi-percolating at the top and centre, and tri-percolating at the bottom left. Thus the PC vectors have implicitly captured complex fea-

6. DONOR-ACCEPTOR-ACCEPTOR OPVS

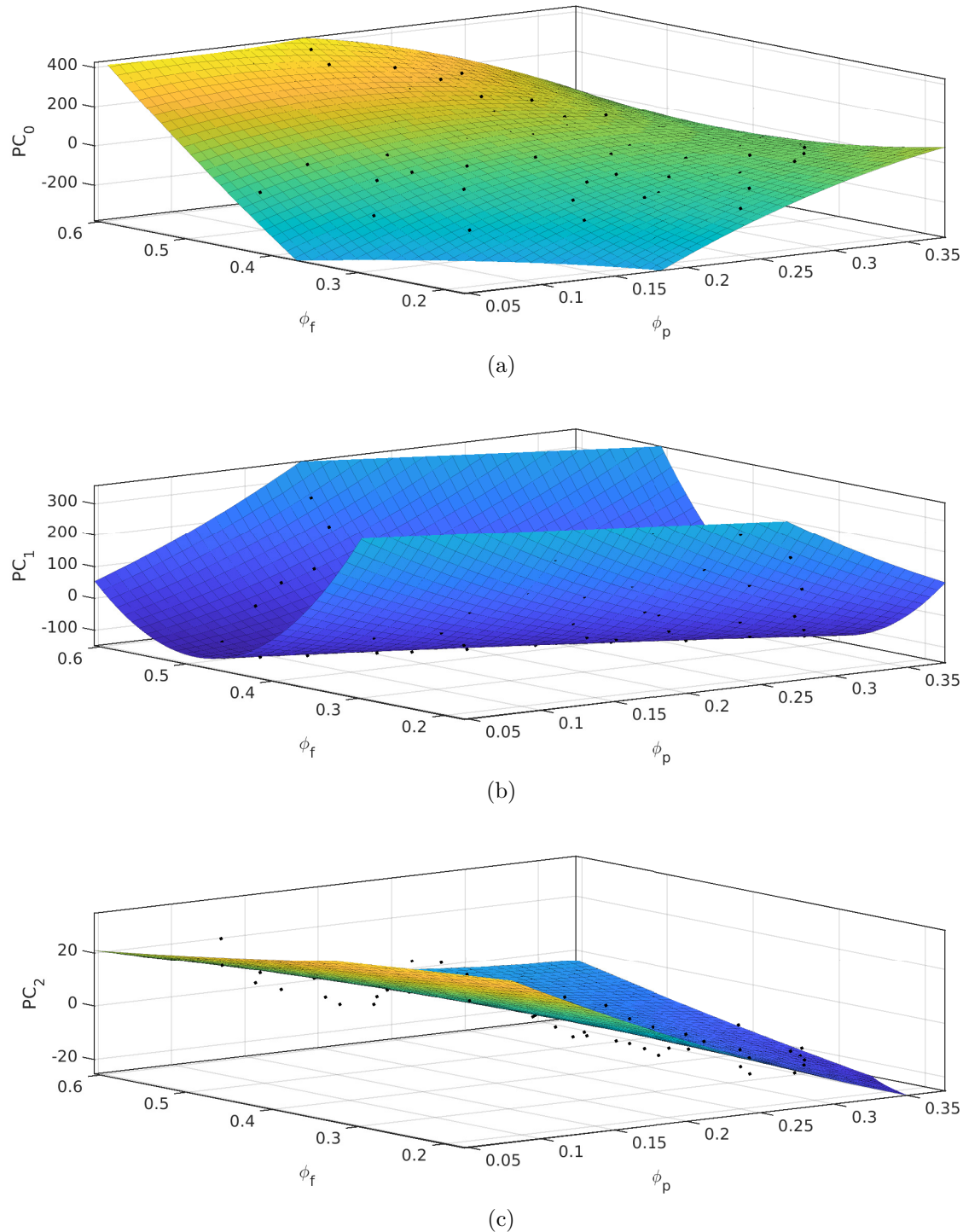


Figure 6.8: PC 's fitted with ϕ_p and ϕ_f (a) PC_0 (b) PC_1 and (c) PC_2 with $r^2 \approx 0.994$, $r^2 \approx 0.998$ and $r^2 \approx 0.85$ respectively.

6. DONOR-ACCEPTOR-ACCEPTOR OPVS

Coefficient	a_1	b_1	c_1	d_1	a_2	b_2	c_2	d_2
DAA	2.7e-04	-1.0e-07	-9.9e-07	5.2e-04	4.8	-2.2e-03	-2.1e-02	7.3

Table 6.5: Coefficients of the multivariable linear regression model to predict the J_{sc} and η from the PC scores for DAA system.

tures like microstructural connectivity. Although we know that the relationship between the microstructure and the electronic property is complicated and naturally involves some non-linearity, the fact that our linear model obtains an $r^2 \approx 0.88$ for η and $r^2 \approx 0.93$ for J_{sc} shows that the principal vectors have captured much of the essential non-linear characteristics.

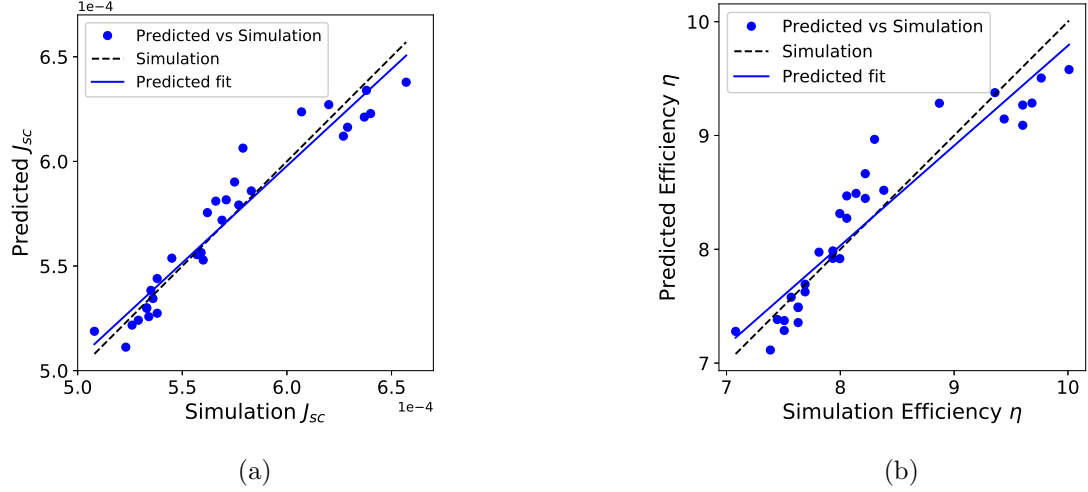


Figure 6.9: Predicted J_{sc} and η values using linear regression with PC_1 , PC_2 and ϕ_p as independent variables against the simulated J_{sc} and η . (a) J_{sc} , $r^2 = 0.93$ (b) η , $r^2 = 0.88$. The dashed line mathematically represents $y = x$ and solid line depicts fit of the predicted data.

Since we have the simulated dataset consisting of η for various blend ratios of polymer, fullerene and ternary component, a natural corollary is to predict the blend ratio that corresponds to the highest η without having to execute further simulations and thus close the PSP loop. Principally, η can be optimised directly with respect to ϕ_p and ϕ_f ; however, in order to derive the morphology corresponding to the highest efficiency, the process-structure simulation that is computationally intensive (takes ≈ 44 hrs for one blend composition on Tesla V100-SXM2 GPU card) will have to be executed. In order to bypass the time-consuming process-structure simulations, we utilise the PCs for expediting the process-structure prediction. Using the mathematical relation expressing PC_i as a function of ϕ_p and ϕ_f as well as the relation between η and PC_i , we performed a maximisation of η . The plot depicting η as a

6. DONOR-ACCEPTOR-ACCEPTOR OPVS

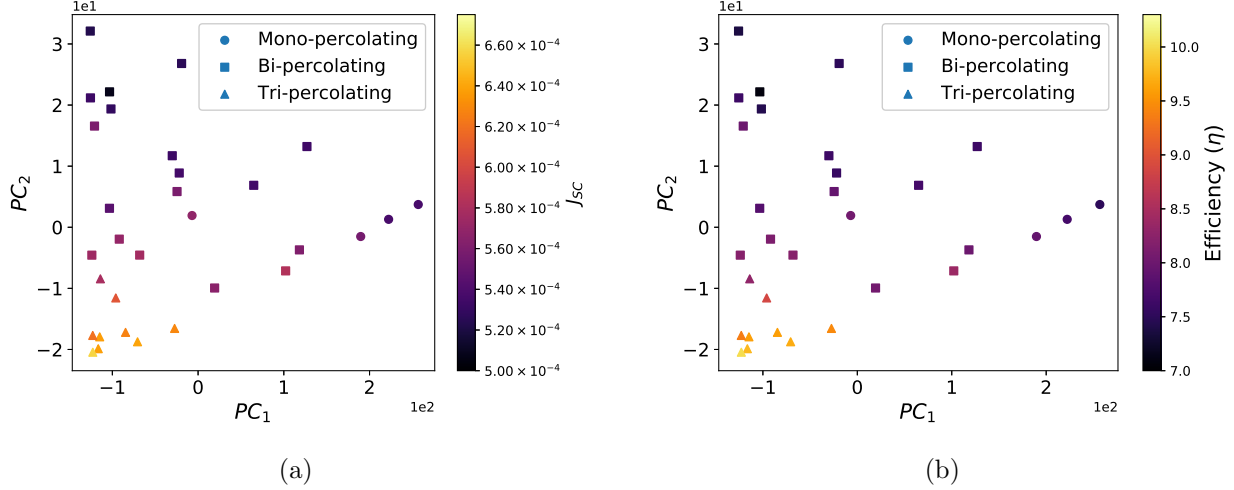


Figure 6.10: Simulated (a) J_{sc} and (b) η values in color plotted against the PC_1 and PC_2 scores. It can be noted that J_{sc} and η vary inversely with PC_1 and PC_2 scores.

function of ϕ_p and ϕ_f is shown in Figure 6.11. The highest efficiency was achieved for the blend composition - 0.34:0.32:0.34, that had not been explored by the structure-property simulations.

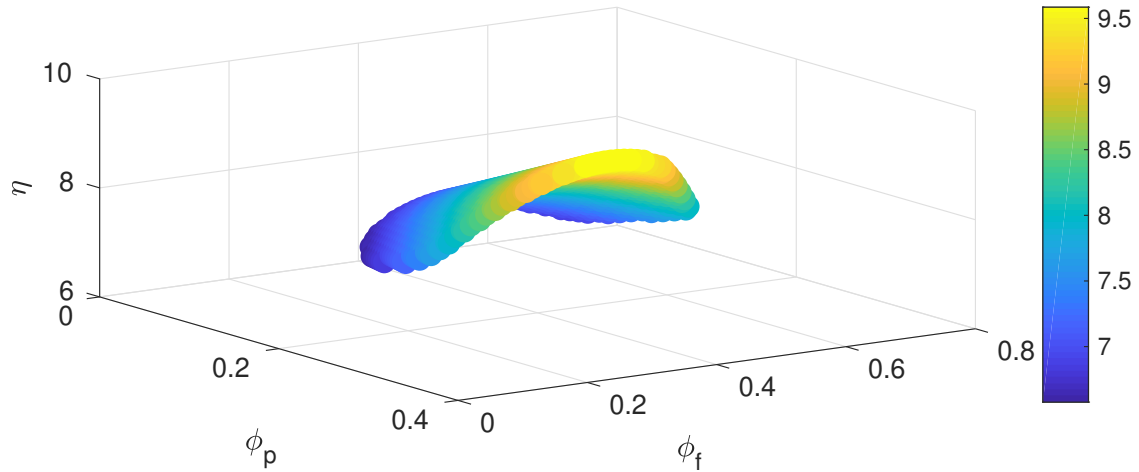


Figure 6.11: Plot depicting η as a function of ϕ_p and ϕ_f . The maximum η is obtained for the blend composition 0.34:0.32:0.34 with respect to polymer, fullerene and ternary acceptor.

6. DONOR-ACCEPTOR-ACCEPTOR OPVS

6.4 Summary

We have been able to establish the PSP correlation in DAA ternary OPVs using the diffuse interface approach. In order to develop structure-property correlations, we used geometrical descriptors of morphology such as interface area, tortuosity and percolation fraction to analyse the variation of the simulated microstructure with photovoltaic properties such as J_{sc} , V_{oc} , FF and PCE. It has been found that the percolation fraction and interface area have a strong influence on the device performance. Amongst these two morphological metrics, interface area has a higher correlation with J_{sc} , V_{oc} and thus on PCE. Using the process-structure and structure-property simulation, the highest PCE for DAA system has been obtained for a tri-percolating morphology. Since these finite geometrical descriptors capture only some features of the morphology, the theoretical PSP prediction has been further complemented by the data analytics model that aids in expediting the identification of optimal morphology. In the data analytics model, a statistical representation of the microstructure using spatial correlation maps and dimensionality reduction techniques has been adopted. Thereafter, a maximisation of PCE has been performed in order to identify the corresponding blend ratio, which had not been explored using the structure-property simulations. Therefore, given the donors and acceptors for fabricating ternary OPVs, the morphologies resulting in sub-optimal device performance can be screened out, and the probable blend ratios for maximal device performance can be identified. This *in silico* framework comprising physics-based and data science approach would accelerate the optimisation of ternary blend morphology for device fabrication. Since quaternary OPVs show great promise [196, 197, 198, 199] and considering that the parameter space becomes even larger; it will be an exciting exercise to optimise their blend morphology using the combined diffuse interface and data science approach.

Chapter 7

Evaporation induced phase-separation in Donor-Acceptor OPVs

In the last chapter of this thesis, we explore the effect of the solvent evaporation rate and the Donor-Acceptor blend composition on the active-layer morphology and subsequently on the device performance. The active-layer deposition involves two processes, i.e., evaporation of the solvent and the phase-separation of the Donor-Acceptor blend. The relative rates of the two processes, i.e., solvent evaporation rate at the top surface and diffusion rate of the donor (polymer) and acceptor (fullerene) molecules within the film is represented by the Mass Biot number (Bi_m) which influences the resulting microstructure, particularly along the thickness of the film and eventually the photovoltaic properties namely J_{sc} , V_{oc} , FF and PCE. The variation of the microstructure along the thickness of the active layer and its evolution with time for various Bi_m and blend compositions has been investigated using the process-structure model (Section 4.1) and further mapped to the photovoltaic parameters using the structure-property model (Section 4.2). This is essential since if the top region of the organic semiconductor film (active layer) exhibits optimal performance, whereas the bottom region exhibits sub-optimal performance, the effective electronic properties of the device are adversely affected. The theoretical framework for modeling evaporation induced phase-separation and its subsequent influence on photovoltaic properties is analysed in this chapter.

7.1 Introduction

Spin-coating is an essential step during device fabrication (Fig. 7.1(a)). Prior to spin-coating, the polymer blend consisting of donor and acceptor organic semiconductor is dissolved in a

7. EVAPORATION INDUCED PHASE-SEPARATION IN DONOR-ACCEPTOR OPVS

common solvent overnight. The polymer blend is then spin-coated onto a substrate at a particular speed depending on the desired thickness of the active layer film. While spin-coating, firstly, the thickness of the film reduces from microns to a couple of hundred nanometers since the solution gets thrown off due to centrifugal force. In the remaining solution, the solvent starts evaporating that leads to the blend phase-separating into donor-rich and acceptor-rich domains [200, 107] (Fig. 7.1). In this next section, we describe the formulation adopted for modeling evaporation-induced phase-separation.

7.2 Modeling

7.2.1 Evaporation model

The mathematical formulation for modeling the evaporation-induced phase-separation in a ternary polymer blend is described in this section [109]. The final polymer blend morphology is a result of simultaneous solvent evaporation and spinodal decomposition. In this work, we have simplified the model for understanding this process by first investigating the effect of solvent evaporation on polymer and fullerene composition fields and then incorporating this information in spinodal decomposition model. Therefore, firstly we model the evaporation in a ternary blend system in 1D assuming solvent is the only species that evaporates. The solvent flux is proportional to the volume fraction of the solvent at the top surface of the blend film and is expressed as $V_m^s J_s = k\phi_s$, where V_m^s is the molar volume of solvent, J_s represents solvent flux, k represents the evaporation rate constant and ϕ_s represents the solvent volume fraction. The evaporation of solvent results in an enrichment of the volume fraction of polymer and fullerene accompanied by a reduction in the height of polymer blend film. Therefore, we solve only for the polymer and fullerene volume fraction, the reduction of solvent volume fraction is incorporated into the evaporation model by a commensurate increase in the volume fraction of polymer and fullerene, i.e., the flux at the top of the film for polymer and fullerene is derived using $J_{i \neq s} = -J_s \phi_{i \neq s}$, where J_i is the flux and ϕ_i is the volume fraction of i^{th} species. This is achieved by imposing an appropriate flux at the top of the film, whereas a zero-flux boundary condition is imposed at the bottom surface. Equation (7.1) governs the polymer and fullerene flux. The change in the volume fraction of polymer and fullerene as a result of solvent evaporation is calculated by solving for the coupled continuity (7.3) and the rate of change of

7. EVAPORATION INDUCED PHASE-SEPARATION IN DONOR-ACCEPTOR OPVS

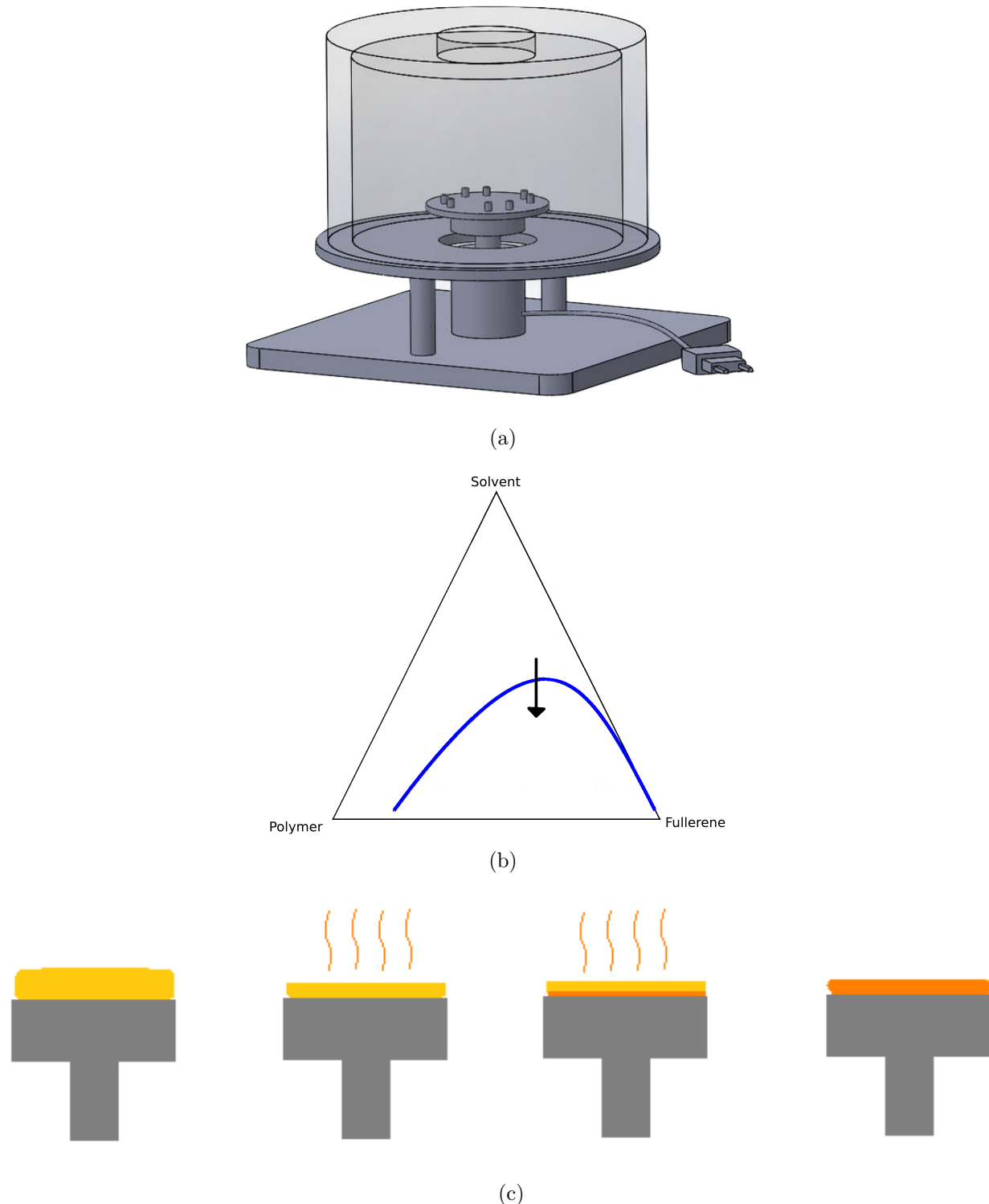


Figure 7.1: Evaporation induced phase-separation (a) CAD model of spin-coater. (b) Simplex representing the evaporation of solvent pushing the system to spinodal regime. (c) Schematic representing the stages of film formation during spin-coating.

7. EVAPORATION INDUCED PHASE-SEPARATION IN DONOR-ACCEPTOR OPVS

height (7.4) equations.

$$\begin{aligned} J_p &= -\Lambda_{aa}\nabla\bar{\mu}_p + \Lambda_{ab}\nabla\bar{\mu}_f \\ J_f &= -\Lambda_{bb}\nabla\bar{\mu}_f + \Lambda_{ab}\nabla\bar{\mu}_p, \end{aligned} \quad (7.1)$$

where Λ_{aa} , Λ_{bb} and Λ_{ab} are effective mobilities; $\bar{\mu}_p$ and $\bar{\mu}_f$ are polymer and fullerene diffusion potentials.

The effective mobilities are given by,

$$\begin{aligned} \Lambda_{aa} &= (1 - \phi_p)^2 \Lambda_p + \phi_p^2 (\Lambda_f + \Lambda_s), \\ \Lambda_{bb} &= (1 - \phi_f)^2 \Lambda_f + \phi_f^2 (\Lambda_p + \Lambda_s), \\ \Lambda_{ab} &= (1 - \phi_p)\phi_f \Lambda_p + \phi_p \Lambda_f (1 - \phi_f) - \phi_p \phi_f \Lambda_s, \end{aligned} \quad (7.2)$$

where Λ_p , Λ_f and Λ_s represent the chemical mobility of polymer, fullerene, and solvent respectively.

$$\frac{\partial\phi_i}{\partial t} = -\nabla \cdot J_i, \quad (7.3)$$

$$\frac{dz}{dt} = -V_m^s J_s. \quad (7.4)$$

where z represents the film height and the index i runs over the polymer and fullerene components. In order to incorporate the change in the height of the film with the same number of grid-points, the resolution of the domain is adjusted corresponding to the change in the height of the film for every time iteration.

Since we want to understand the effect of solvent evaporation on blend morphology, we have divided the domain within the 1D film (used in the evaporation model) into four equally spaced elements and have tracked the variation of average polymer and fullerene volume fractions within these elements with time as shown in Figure 7.2. The spatio-temporal volume fraction data for polymer and fullerene derived from these representative elements is then incorporated in the phase-field model used for simulating morphology evolution.

7. EVAPORATION INDUCED PHASE-SEPARATION IN DONOR-ACCEPTOR OPVS

7.2.2 Process-structure relationship

The polymer and fullerene volume fractions derived from the evaporation model are fitted to determine the mathematical expression for the rate of change of volume fraction and these are then incorporated as a source term in the spinodal-decomposition phase-field model to determine the microstructure as a result of solvent evaporation(Equations (7.5) and (7.6)).

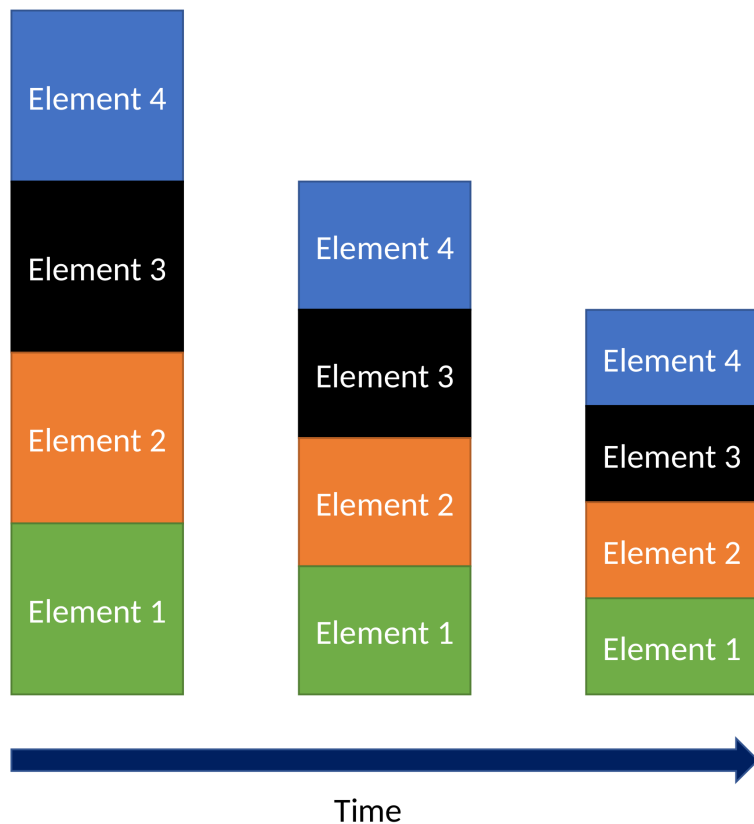


Figure 7.2: Schematic depicting the representative elements that are tracked for polymer and fullerene volume fraction and the decrease in their heights with time.

$$\begin{aligned} \frac{\partial \phi_p}{\partial t} = & \Lambda_{aa} \left[\nabla^2 \left(\frac{\partial f}{\partial \phi_p} \right) - 2(\kappa_p + \kappa_s) \nabla^4 \phi_p - 2\kappa_s \nabla^4 \phi_f \right] \\ & + \Lambda_{ab} \left[\nabla^2 \left(\frac{\partial f}{\partial \phi_f} \right) - 2(\kappa_f + \kappa_s) \nabla^4 \phi_f - 2\kappa_s \nabla^4 \phi_p \right] + \dot{E}_p, \end{aligned} \quad (7.5)$$

$$\frac{\partial \phi_f}{\partial t} = \Lambda_{bb} \left[\nabla^2 \left(\frac{\partial f}{\partial \phi_f} \right) - 2(\kappa_f + \kappa_s) \nabla^4 \phi_f - 2\kappa_s \nabla^4 \phi_p \right]$$

7. EVAPORATION INDUCED PHASE-SEPARATION IN DONOR-ACCEPTOR OPVS

$$+ \Lambda_{ab} \left[\nabla^2 \left(\frac{\partial f}{\partial \phi_p} \right) - 2(\kappa_p + \kappa_s) \nabla^4 \phi_p - 2\kappa_s \nabla^4 \phi_f \right] + \dot{E}_f, \quad (7.6)$$

where \dot{E}_p and \dot{E}_f are the source terms representing the rate of change in the volume fraction of polymer and fullerene respectively due to evaporation.

The following set of non-dimensional parameters (see Table 7.1) have been utilized for simulating the microstructures for polymer (p), fullerene (f) and solvent (s) during spinodal decomposition, while the phase diagram is depicted in Fig.7.9.

Param	χ_{pf}	$\kappa_{p,f,s}$	Λ_{aa}	Λ_{bb}	Λ_{ab}	N_p	N_f	N_s
Value	0.15	0.1	1.0	1.0	0.5	100	10	1

Table 7.1: Process-Structure model parameter table for polymer, fullerene and solvent system.

7.2.3 Structure-property relationship

The photovoltaic performance of the morphologies generated as a result of different processing condition is evaluated using the diffuse-interface structure-property model described in Section 4.2. The model parameters that have been used in our simulations are shown in Table 7.2

Parameter	Value
$D_e^{Polymer}$	10
$D_e^{Fullerene}$	15
$D_h^{Polymer}$	15
$D_h^{Fullerene}$	10
$x_e^{Polymer}$	5e-5
$x_e^{Fullerene}$	5e-3
$x_h^{Polymer}$	5e-3
$x_h^{Fullerene}$	5e-5
N_D	4.95e-3
N_A	4.95e-3
G_0	2e-7
V_{bi}^{pf}	5.0
ϵ	1
V_m	1

Table 7.2: Structure-Property model parameter table for polymer, fullerene and solvent system.

7. EVAPORATION INDUCED PHASE-SEPARATION IN DONOR-ACCEPTOR OPVS

7.3 Results

In this section, the results obtained using the PSP formulation described above will be presented and analysed. The variation of polymer and fullerene volume fraction within the 1D domain is depicted in Figure 7.3. The system domain is then classified into four elements, and the average polymer and fullerene volume fractions in the elements are tracked and subsequently fitted and fed in the process-structure model for deriving the microstructure as a result of evaporation-induced phase-separation. Figure 7.4 depicts the volume fraction profiles for polymer and fullerene in various elements as a function of time for initial blend composition ($\phi_p : \phi_f : \phi_s = 0.10:0.45:0.45$) derived using the evaporation model. The evaporation simulations have been carried out until the volume fraction of the residual solvent is ≤ 0.05 . The resulting morphology evolution for various elements with time is shown in Figure 7.5. The active-layer deposition involves two processes, i.e., evaporation of the solvent and the phase-separation of the Donor-Acceptor blend. The relative rates of the two processes, i.e., solvent evaporation rate at the top surface (represented by k) and diffusion rate of the donor (polymer) and acceptor (fullerene) molecules within the film (represented by $\Lambda f/H$, where Λ represents the mobility and in all the simulations, we have adopted equal mobilities, i.e., $\Lambda_p = \Lambda_f = \Lambda_s = \Lambda$; f , the energy scale given by $f = \frac{RT}{V_m}$ and H represents the scaled height of the film) is given by mass Biot number (Bi_m) which influences the resulting microstructure, particularly along the thickness of the film and eventually the photovoltaic properties namely J_{sc} , V_{oc} , FF and PCE. The variation of the microstructure along the thickness of the active layer and its evolution with time for various Bi_m and blend compositions has been investigated using the process-structure model and further mapped to the photovoltaic parameters using the structure-property model. This is essential since if the top region of the organic semiconductor film (active layer) exhibits optimal performance, whereas the bottom region exhibits sub-optimal performance, the effective electronic properties of the device are adversely affected. For the blend composition 0.10:0.45:0.45, simulations were done for various Bi_m in the range of 0.01 to 1.66, morphologies corresponding to the extremes i.e., $Bi_m = 1.66$ and $Bi_m = 0.01$ are shown in Figure 7.6. It was observed that at high Bi_m (i.e., when evaporation rate dominates the diffusion rate), the microstructure possesses fine domains whereas, at low Bi_m (i.e., when diffusion rate dominates the evaporation rate), a coarse microstructure is rendered. The following arguments explain this variation in microstructural length scale in both cases. Spinodal decomposition occurs as a result of spatially correlated perturbations with different wavelengths. Amongst these perturbations, the wave with the fastest growth rate sets the microstructural length scale. Upon doing the Linear Stability Analysis (LSA) of ternary Cahn-Hilliard equation in

7. EVAPORATION INDUCED PHASE-SEPARATION IN DONOR-ACCEPTOR OPVS

1D, it is found that the maximally growing wavelength (fastest growing wavelength) is given by $\lambda_m = 2\pi\sqrt{-4\kappa/B}$, where $B = a_{11} + a_{22} - \sqrt{a_{11}^2 + 4a_{12}^2 - 2a_{11}a_{22} + a_{22}^2}$, and $a_{ij} = \frac{\partial^2 f}{\partial \phi_i \partial \phi_j}$, with f being the Flory-Huggins free energy density [108]. Therefore, it can be seen that the microstructural length scale is inversely proportional to the $\sqrt{-B}$, which is a function of the free energy curvature. In case of high Bi_m , due to faster solvent evaporation, the blend composition quickly approaches and phase-separates in the interior of the spinodal regime where the magnitude of B is high (Figure 7.7), thus resulting in a fine microstructure. In contrast, in the case of low Bi_m , due to slower solvent evaporation, the blend phase-separates close to the periphery of spinodal regime wherein the magnitude of B is low (Figure 7.7), thus resulting in the coarser microstructure. Besides, there exists a threshold Bi_m (that varies based on the initial blend composition) below which the bottom elements do not enter the spinodal regime and thus do not undergo phase-separation as shown in Figure 7.8. Further, in order to complete the process-structure correlation and study the effect of evaporation rate and initial blend composition on microstructure, simulations were done for three blend compositions shown in Figure 7.9. The blend compositions have been chosen such that the broad trend in variation of morphology with volume fraction is captured, therefore, one blend composition (label b in Figure 7.9) is symmetric with respect to the miscibility gap whereas the other two compositions (label a and c in Figure 7.9) are located towards polymer and fullerene rich sides respectively.

We further characterised these microstructures using simple geometrical descriptors such as percolation fraction, interfacial area and tortuosity since it is well-known [160, 201, 202] that these descriptors influence photovoltaic performance. The characterisation of morphology corresponding to blend labelled ‘b’ revealed that the percolation fraction is insensitive to Bi_m , with the percolation fraction being 1.0 for all mass Biot numbers, whereas it was found that Bi_m has a significant influence on the interfacial area. The variation of interfacial area and tortuosity is shown in Figure 7.10.

Thereafter, structure-property simulations were carried out to close the PSP loop in donor-acceptor OPVs. The J-V characteristics of element 4 for the blend composition 0.10:0.45:0.45 is shown in Figure 7.11. We had found in our previous work [201] that high Power Conversion Efficiency (PCE) results from bi-continuous morphologies and higher interfacial area. Amongst the bi-continuous morphologies, PCE, J_{sc} and V_{oc} are strongly correlated with the interfacial area. Figure 7.12 shows that morphologies resulting from $Bi_m = 1.66$ for blend composition 0.10:0.45:0.45 exhibit higher PCE owing to higher interfacial area as a consequence of a finer microstructure (see Figure 7.10). Further, the variation in tortuosity among the elements seems too low to significantly affect the device performance. Since morphologies produced by Bi_m below the threshold also lead to elements that do not phase separate and eventually to sub-

7. EVAPORATION INDUCED PHASE-SEPARATION IN DONOR-ACCEPTOR OPVS

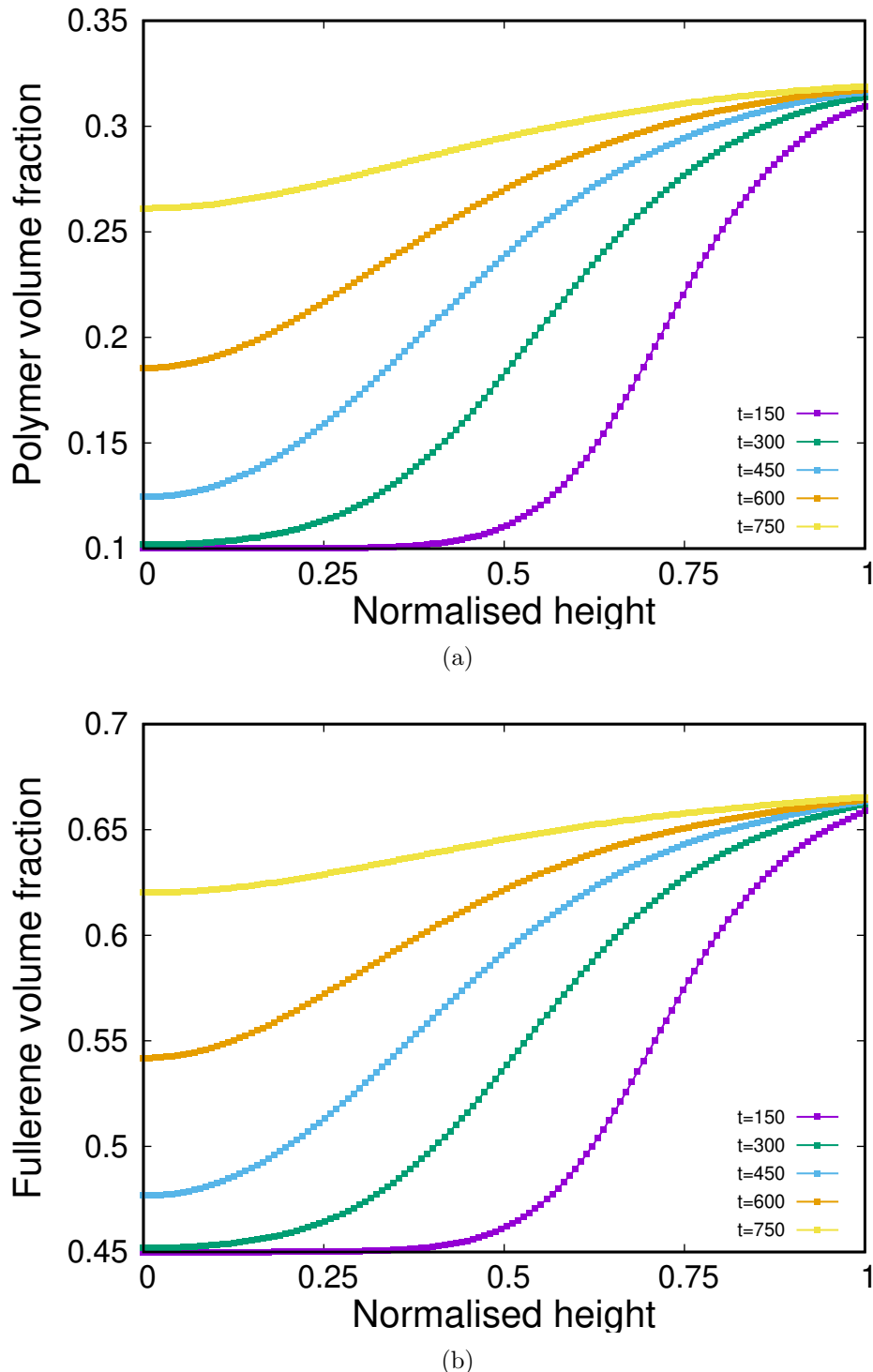


Figure 7.3: Volume fraction profiles in the 1D domain with time for (a) Polymer (ϕ_p) and (b) Fullerene (ϕ_f). Note: The system height has been normalised with respect to itself at each time step in this figure.

7. EVAPORATION INDUCED PHASE-SEPARATION IN DONOR-ACCEPTOR OPVS

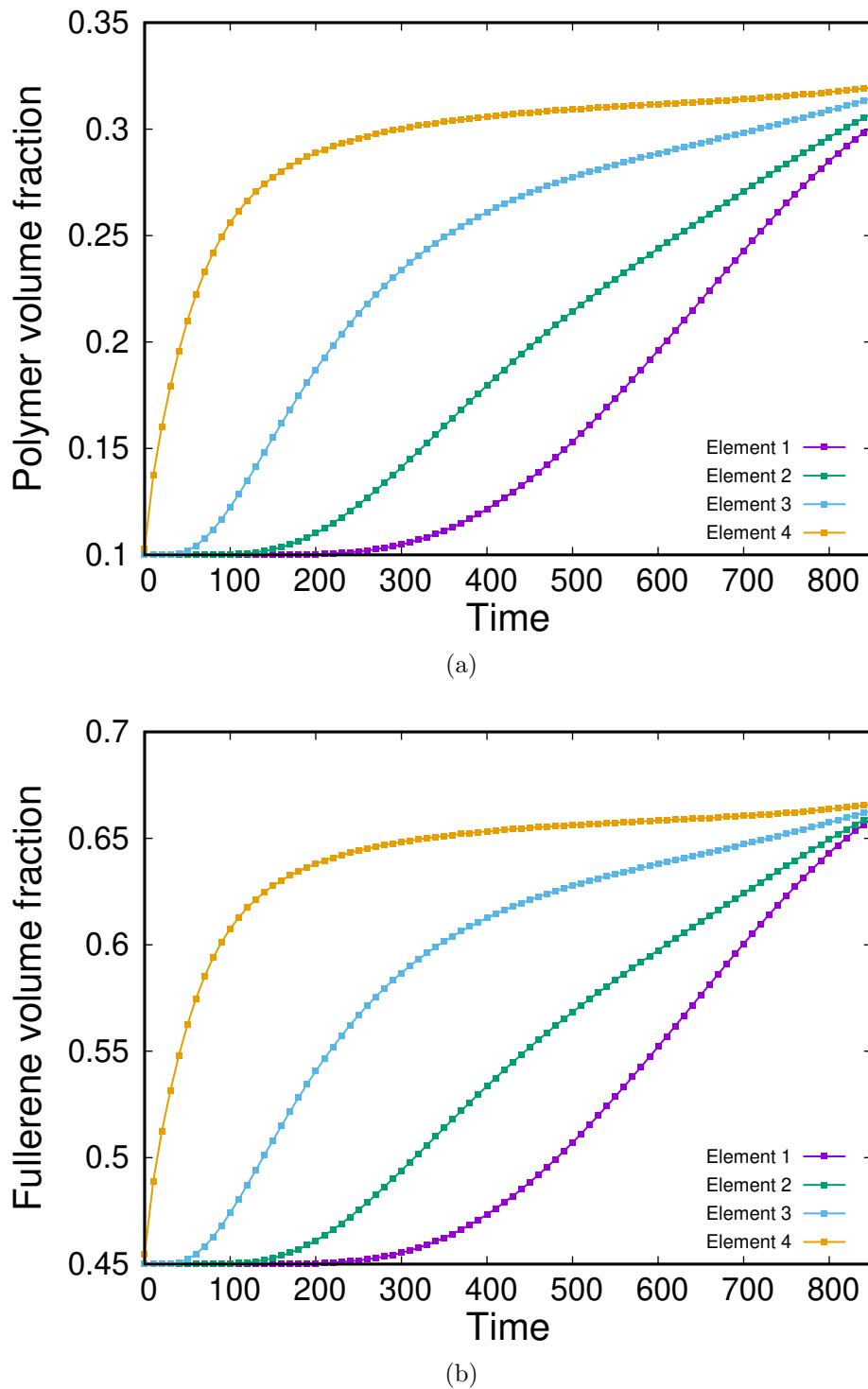


Figure 7.4: Volume fraction profiles for elements 1-4 with time for (a) Polymer (ϕ_p) and (b) Fullerene (ϕ_f)

7. EVAPORATION INDUCED PHASE-SEPARATION IN DONOR-ACCEPTOR OPVS

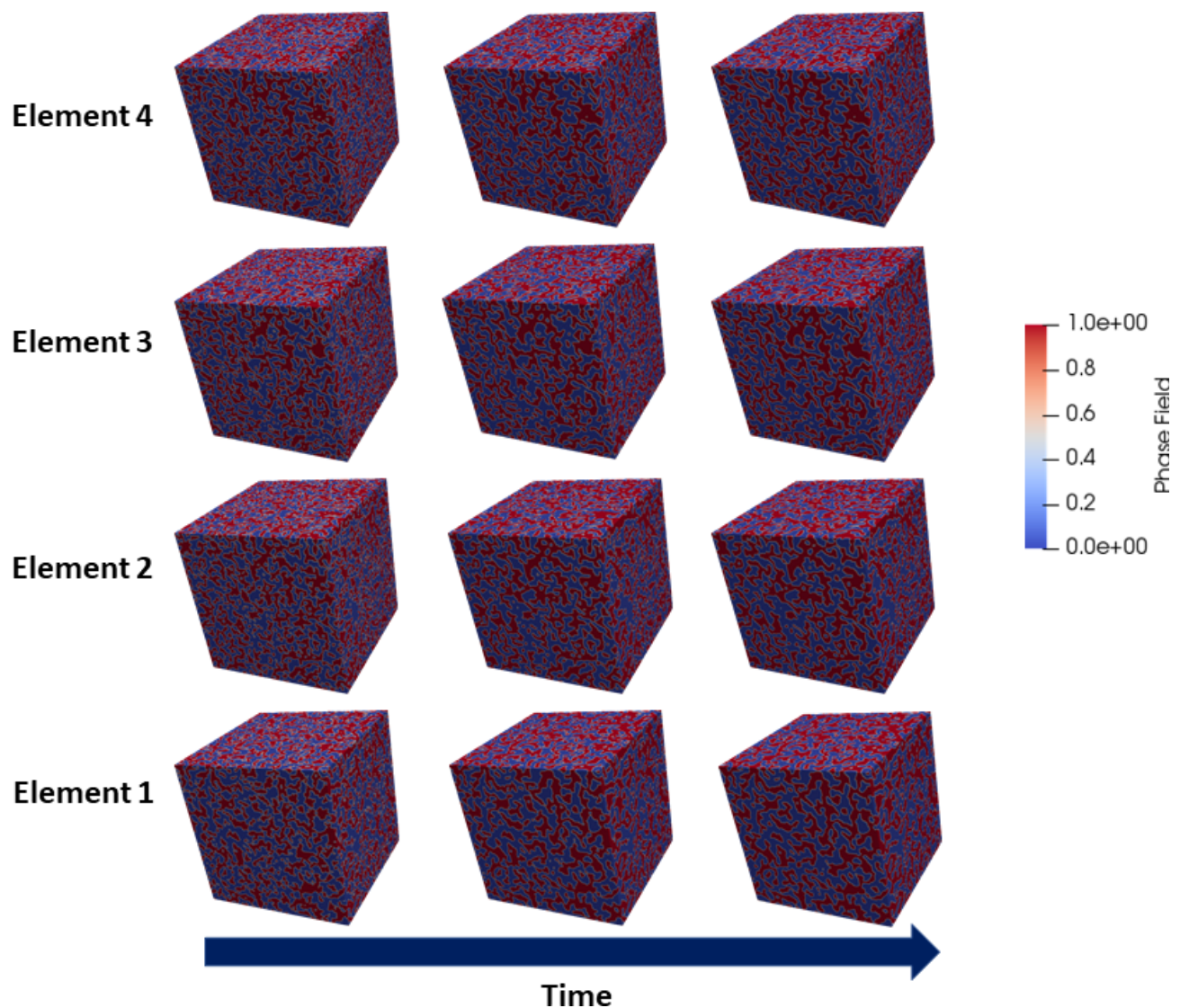


Figure 7.5: Morphology evolution of elements 1-4 as a function of time for $Bi_m = 1.66$. On the colorbar 0 corresponds to polymer rich phase whereas 1 corresponds to fullerene rich phase.

7. EVAPORATION INDUCED PHASE-SEPARATION IN DONOR-ACCEPTOR OPVS

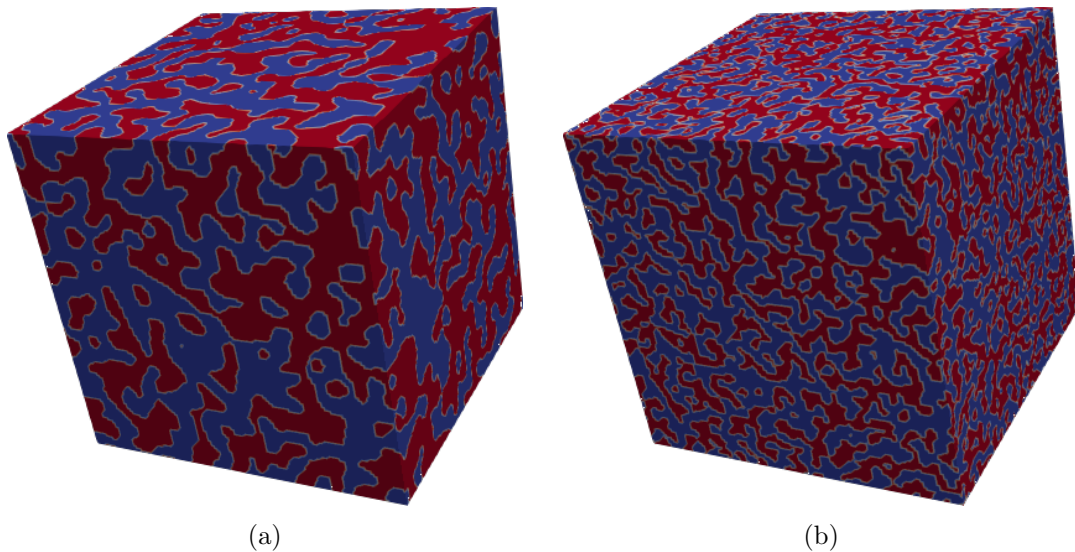


Figure 7.6: Microstructure for element 4 corresponding to (a) $Bi_m = 0.01$ and (b) $Bi_m = 1.66$. Microstructure resulting from a high Bi_m has fine domains whereas the one with low Bi_m has coarse domains.

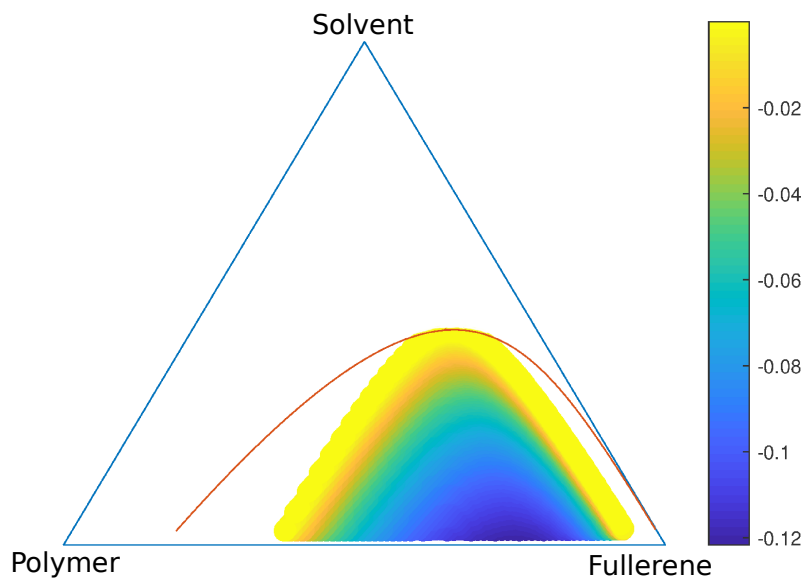


Figure 7.7: Map of B in the spinodal regime on the simplex. It can be observed that the magnitude of B is higher in the interior of the spinodal regime and lower at the periphery. The red curve corresponds to the polymer-fullerene binodal.

7. EVAPORATION INDUCED PHASE-SEPARATION IN DONOR-ACCEPTOR OPVS

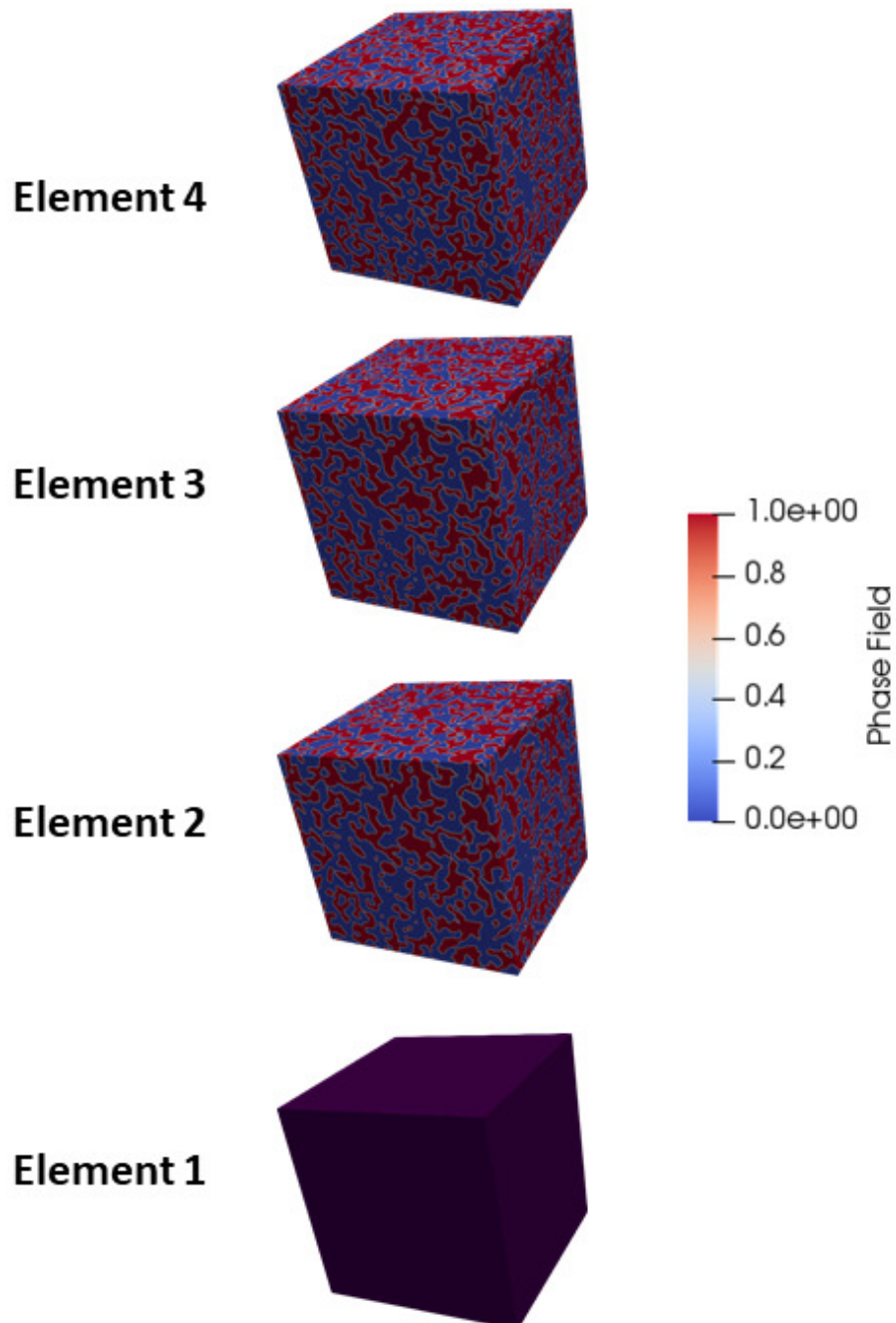


Figure 7.8: Morphologies of various elements for blend composition 0.15:0.38:0.47. It can be observed that element 1 has not phase-separated whereas elements 2-4 have undergone spinodal decomposition. On the colorbar 0 corresponds to polymer rich phase whereas 1 corresponds to fullerene rich phase.

7. EVAPORATION INDUCED PHASE-SEPARATION IN DONOR-ACCEPTOR OPVS

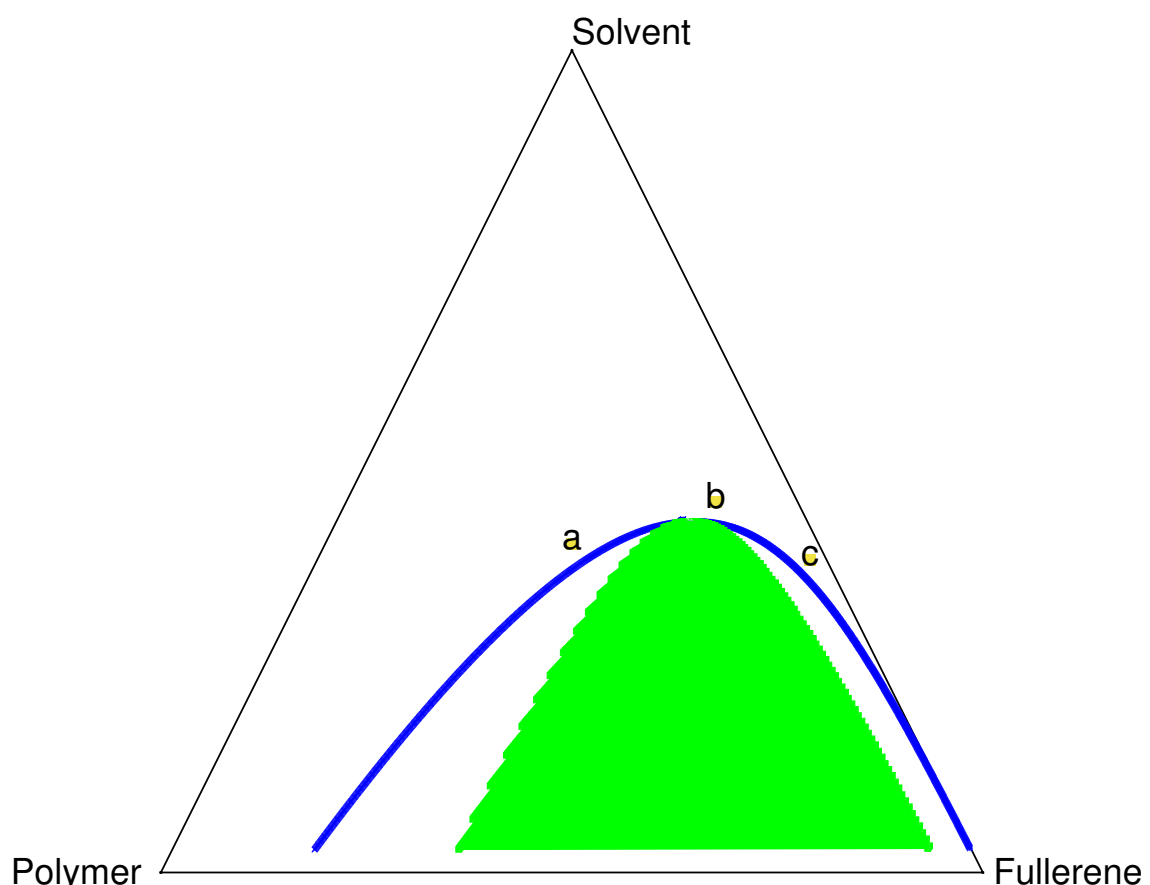


Figure 7.9: Isothermal section of the polymer-fullerene-solvent phase-diagram with points a, b and c corresponding to blend compositions 0.30:0.30:0.40, 0.15:0.38:0.47 and 0.03:0.52:0.45 respectively. The green portion of the curve represents the spinodal region.

7. EVAPORATION INDUCED PHASE-SEPARATION IN DONOR-ACCEPTOR OPVS

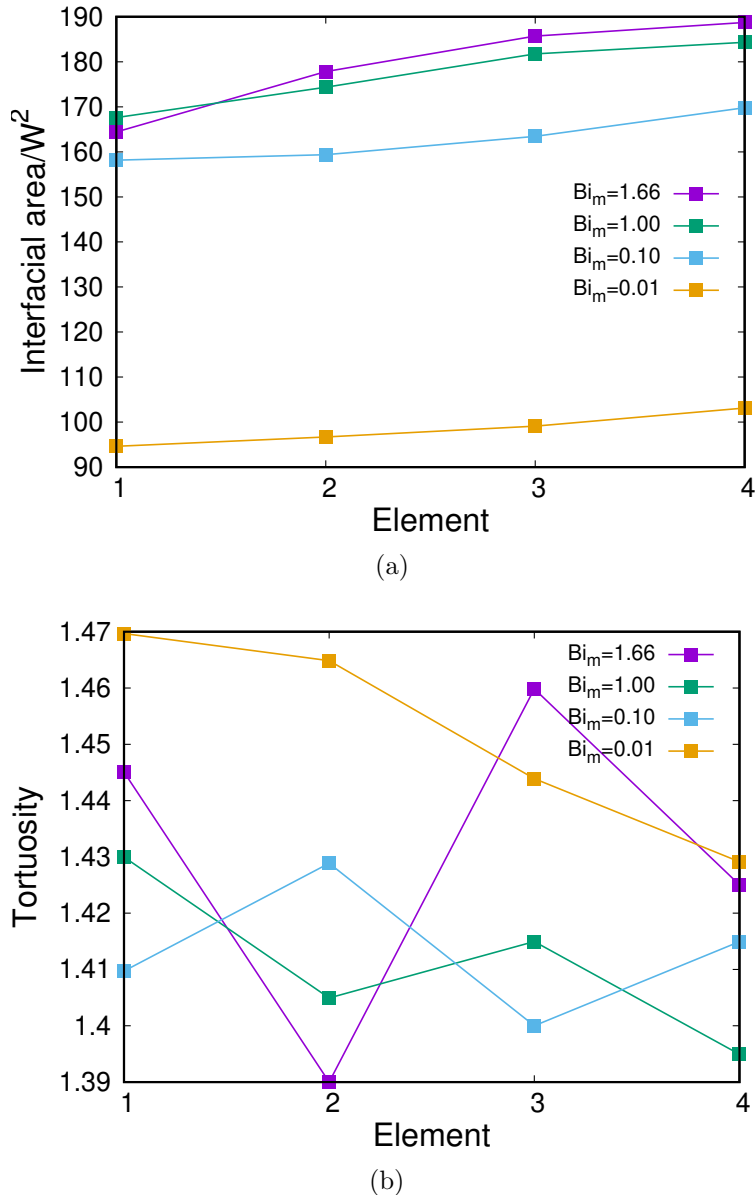


Figure 7.10: Simulation results depicting (a) interfacial area normalised by square of depletion width (W) (b) tortuosity as a function of element for blend composition 0.10:0.45:0.45 for $Bi_m = 1.66$, $Bi_m = 1.00$, $Bi_m = 0.10$, and $Bi_m = 0.01$.

7. EVAPORATION INDUCED PHASE-SEPARATION IN DONOR-ACCEPTOR OPVS

optimal device performance, these morphologies are ruled out for optimising device efficiency. Therefore, in the present work, the structure-property simulations have been carried out for morphologies (corresponding to various blend compositions) derived as a result of $Bi_m = 1.66$ since they demonstrate better performance. The variation of photovoltaic properties with blend composition for various elements is depicted in Figure 7.13. It can be observed that all elements corresponding to blend composition 0.10:0.45:0.45 perform better in terms of PCE than the asymmetric blends (label a and c) and would, therefore, lead to better devices. We found that all the elements for the blend compositions a, b and c have a percolation fraction of 1.0. The variation in PCE (Figure 7.13(a)), J_{sc} (Figure 7.13(b)) and V_{oc} (Figure 7.13(c)) follows the same trend as that of the interfacial area as shown in Figure 7.14(a). Further, no direct relationship between tortuosity (Figure 7.14(b)) and photovoltaic properties (Figure 7.13) can be ascertained. Since the PCE deteriorates as we move away from the symmetric blend b towards polymer and fullerene rich sides, we did not probe those blend compositions. It can be observed that the top layers (elements 3 and 4) perform better than the bottom layers (elements 1 and 2) owing to the higher interface area as can be seen in Figure 7.14(a). This variation in the interfacial area amongst the elements can be attributed to the difference in evaporation rates experienced by the top and bottom layers (see Figure 7.4) which in turn alters the composition at which phase-separation is initiated. Owing to faster evaporation rate experienced by the top layers, the blend composition quickly proceeds away from the spinodal critical point, and thus the phase-separation occurs in the interior of the spinodal regime rendering a fine microstructure and subsequently a higher interfacial area. In contrast, owing to a more gradual evaporation rate experienced by the bottom layers, the phase-separation occurs at the periphery of the spinodal regime, thus resulting in a coarse morphology and thus a lower interfacial area.

7.4 Summary

The influence of evaporation rate and initial blend composition on the device performance of BHJ Donor-Acceptor OPVs has been investigated. We found that at high Bi_m , the resulting morphology possesses fine domains. This resulted in higher interfacial area and thus higher generation of carriers, subsequently leading to high J_{sc} , V_{oc} and PCE. Since optimal device performance is a result of bi-percolating microstructure and high interfacial area, we further analysed the effect of blend composition on device performance by probing different initial donor-acceptor blend ratios. It was found that compositions symmetric with respect to the miscibility gap were bi-percolating, exhibited higher interfacial area and thus higher performance of all layers within the device. We would like to mention here that since we have adopted equal

7. EVAPORATION INDUCED PHASE-SEPARATION IN DONOR-ACCEPTOR OPVS

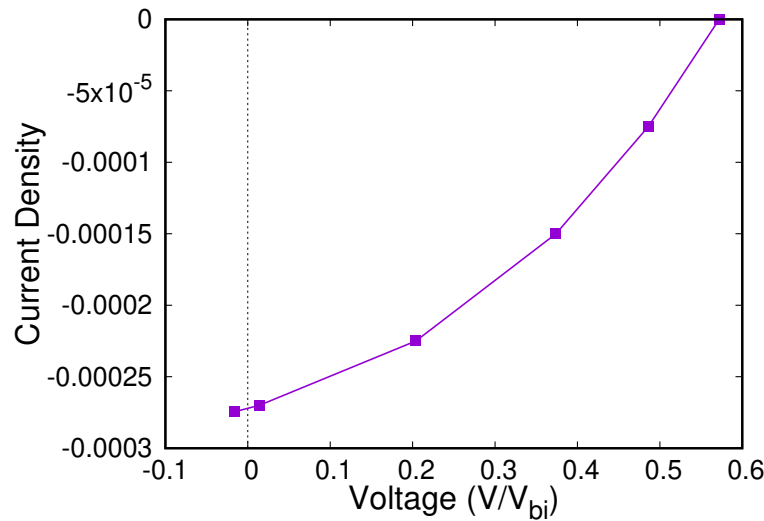


Figure 7.11: Simulated J-V characteristics of element 4 for the blend composition 0.10:0.45:0.45.

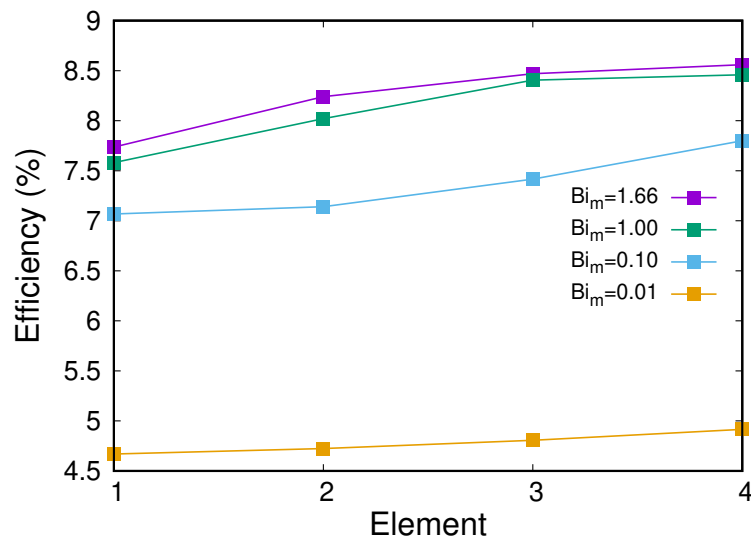


Figure 7.12: Simulation results depicting efficiency as a function of element for blend composition 0.10:0.45:0.45 for various Bi_m .

7. EVAPORATION INDUCED PHASE-SEPARATION IN DONOR-ACCEPTOR OPVS

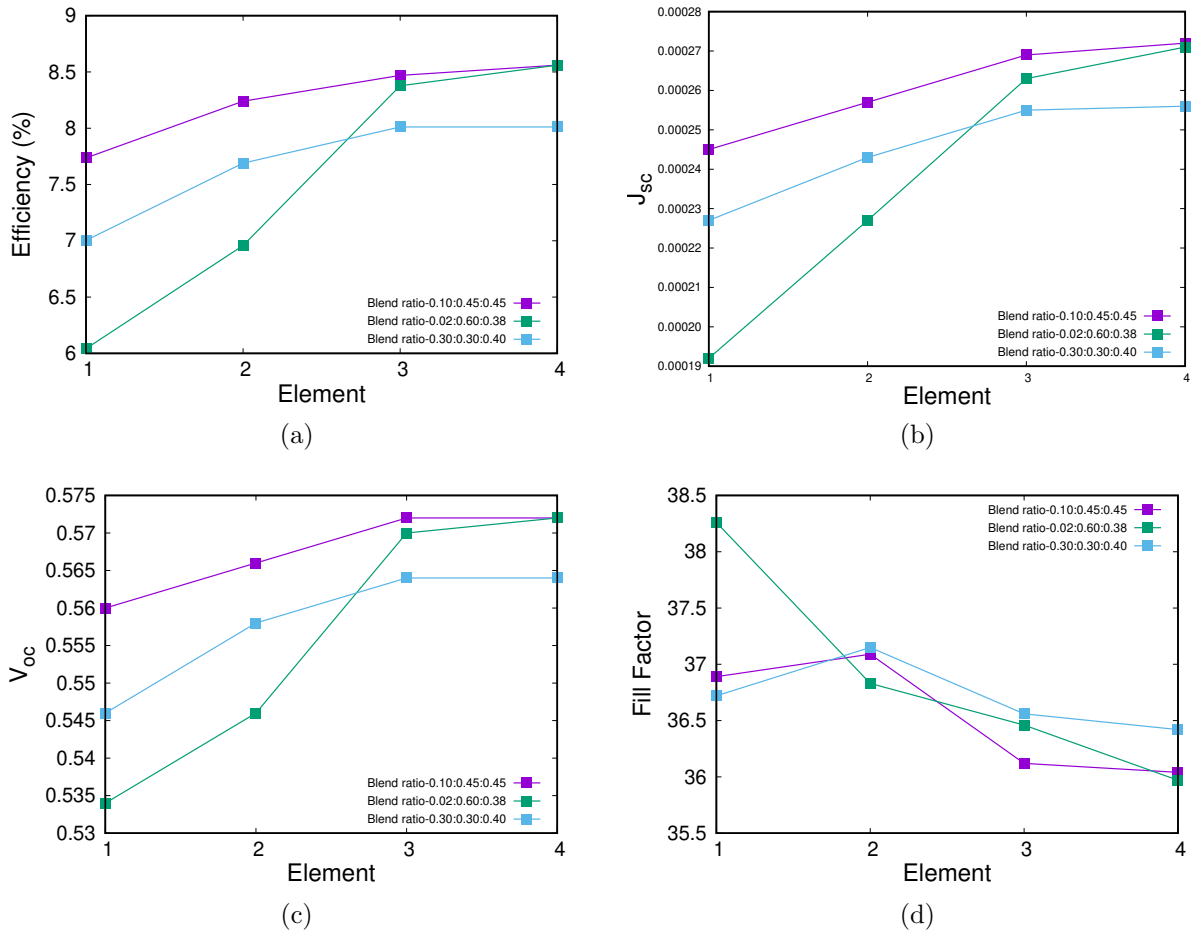
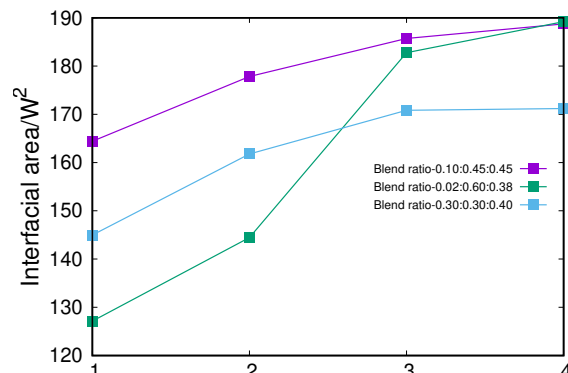
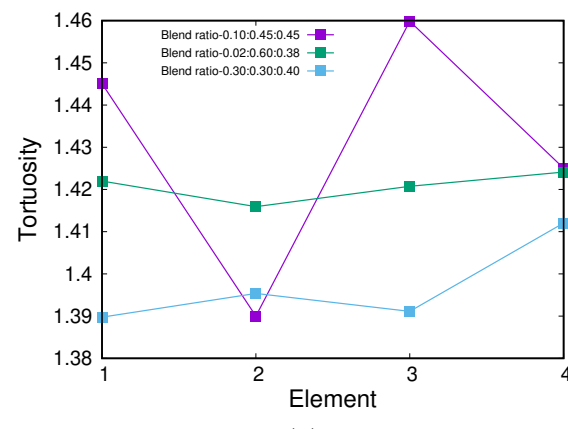


Figure 7.13: Simulation results depicting (a) Efficiency, (b) Short-circuit current density (J_{sc}), (c) Open-circuit voltage (V_{oc}) and (d) Fill Factor as a function of element for blend compositions 0.30:0.30:0.40, 0.10:0.45:0.45 and 0.02:0.60:0.38. All the elements corresponding to the blend composition 0.10:0.45:0.45 which is symmetric with respect to miscibility gap perform better than the other blend composition in terms of PCE.

7. EVAPORATION INDUCED PHASE-SEPARATION IN DONOR-ACCEPTOR OPVS



(a)



(b)

Figure 7.14: Simulation results depicting (a) interfacial area and (b) tortuosity as a function of element for blend compositions 0.30:0.30:0.40, 0.10:0.45:0.45 and 0.02:0.60:0.38.

7. EVAPORATION INDUCED PHASE-SEPARATION IN DONOR-ACCEPTOR OPVS

mobilities for all species, equal volume fraction ($\phi_i = 0.5$) of polymer and fullerene phases and thus bi-percolating morphologies are derived for blend compositions symmetric with respect to the miscibility gap. However, if unequal mobilities of the species are chosen, it is possible to derive bi-percolating microstructures even for unequal volume fraction of donor and acceptor phases which results from asymmetric blend compositions [203]. Further, it was found that there exists a threshold Bi_m , below which the bottom layers do not phase-separate leading to sub-optimal performance of the device. The application of this formulation to state-of-the-art quarternary systems such as donor-acceptor-donor-solvent and Donor-Donor-Acceptor-Solvent blends forms an exciting future work.

Chapter 8

Conclusions & Outlook

In this thesis, we have established the PSP relationship in BHJ OPVs and have pinpointed the processing conditions and resulting microstructures that optimise the device performance. This is essential since the optimisation of photovoltaic parameters like J_{sc} , V_{oc} , FF, and PCE becomes more streamlined and the experimental effort in deriving champion devices gets minimised. We firstly performed experimental studies to investigate the influence of blend ratio and annealing time on Donor-Acceptor OPVs comprising P3HT (polymer donor) and PCBM (fullerene acceptor). This set the motivation for theoretical studies in order to unravel the PSP correlation in OPVs. In the theoretical framework, we formulated a novel diffuse-interface method which is more relevant to BHJ OPVs considering their complex morphology for investigating the structure-property relationship. This also provides for an elegant methodology to model both the process-structure and structure-property relationship using a common diffuse-interface approach. Further, since Donor-Acceptor OPVs capture only a limited portion of the solar spectrum, we carried out experimental and numerical studies on Donor-Acceptor-Acceptor OPVs which render higher PCE and are more stable. The experimental studies were conducted on PTB7-Th, COi8DFIC and PC₇₀BM ternary system. In the theoretical exploration of PSP relationship in ternary OPVs comprising Donor-Acceptor-Acceptor, we used data analytics in order to expedite the prediction of optimal morphology. Finally, we modeled the effect of mass Biot number (Bi_m) and initial blend composition on the microstructure and subsequently on the device performance of Donor-Acceptor OPVs. The in-silico framework developed in this thesis is aimed at accelerating the experimental identification of optimal processing parameters for device fabrication by screening out the sub-optimal variables and focussing on the potentially viable processing parameters. Also, the PSP optimisation approach adopted in this work is fairly generic and can be applied to organic electronics in general.

In the following, a concise summary of the results obtained and the future outlook is pre-

8. CONCLUSIONS & OUTLOOK

sented:

8.1 Experiments

Several experimental studies [100, 101, 102, 103, 104, 105] have been carried out in the field of OPVs. Since polymer solar cells are sensitive to fabrication protocol, ambient conditions during experimentation, the molecular weight of donor polymer, and even the batch of commercial grades of polymer, we have conducted our own set of experiments to get first-hand information on the effect of processing parameters on device performance. P3HT and PC₆₀BM were blended in various blend ratios, and their influence on PCE was observed in Chapter 3. Also, the variation in J_{sc} with post-production annealing time was recorded. Further, experiments were done on state-of-the-art ternary OPVs comprising PTB7-Th (donor polymer), PC₇₀BM (fullerene acceptor) and COi8DFIC (non-fullerene acceptor). In all these studies, we observed an optimal blend composition and annealing time with respect to PCE. These experiments motivated the numerical investigation of PSP relationship in Donor-Acceptor and Donor-Acceptor-Acceptor OPVs. Elucidating the complex BHJ morphology remains an open challenge and the experimental characterisation of the active layer using state-of-the-art techniques such as analytical transmission electron microscopy [204] in order to quantitatively establish the correlation between processing parameters and resulting microstructure has scope for future work. This would enable tailoring the active layer morphology for deriving maximal device performance.

8.2 Donor-Acceptor OPVs

In Chapter 5, we applied the diffuse-interface formulation for modeling PSP relationship to Donor-Acceptor OPVs. Using geometrical descriptors, namely the interfacial area and percolation fraction, we were able to explain the origin of optimal efficiency. It was found that the necessary condition for optimising PCE is a bi-continuous network of donor and acceptor phases. Further, amongst the bi-percolating morphologies, the ones with higher interfacial area maximised the J_{sc} , V_{oc} and subsequently PCE. While the optimisation of PSP relationship has been done for P3HT:PCBM system, it would be an interesting future work to couple our model with microscopic models in order to investigate the optimal choice of materials. In this approach, using the microscopic model, potentially useful materials can be identified and further the derived properties can be fed into the diffuse-interface model to determine the optimal processing conditions.

8. CONCLUSIONS & OUTLOOK

8.3 Donor-Acceptor-Acceptor OPVs

In Chapter 6, we optimised the PSP correlation in ternary OPVs comprising donor and two acceptors using both physics-based and data-analytics model. Firstly, physics-based simulations for ternary OPVs were performed using the robust diffuse-interface method formulated in this thesis and PSP correlations were established using geometrically motivated morphological descriptors - interfacial area, tortuosity and percolation fraction. However, since these descriptors capture only some features of the microstructure and do not represent the complex BHJ morphology in its entirety, we used a data-analytics model in addition to these descriptors for investigating the PSP relationship and thereafter deriving optimal blend composition. Additionally, the data-analytics model expedites the prediction of PSP correlation which is otherwise computationally intensive. We found that tri-percolating morphologies possessing high interfacial area maximised the PCE. Also, the optimal blend composition predicted by the data-science model was close to the one found by the physics-based model. Since quaternary OPVs show great promise [196, 197, 198, 199] and considering that the parameter space becomes even larger; optimising their blend morphology using the combined diffuse interface and data science approach forms for interesting future work.

8.4 Evaporation induced phase-separation in Donor-Acceptor OPVs

In Chapter 7, we modeled the solvent evaporation during device fabrication and further coupled it with the diffuse-interface process-structure-property model. The objective of this exercise has been to gather information on the effect of solvent evaporation on the blend morphology along the film thickness since for an efficient OPV device, it is essential that all regions of the active layer exhibit optimal performance. We found that optimal processing conditions correspond to high Bi_m since it results in higher interfacial area of donor-acceptor phases, thus enhancing the carrier generation and subsequently the photovoltaic parameters. Further, upon simulating various initial blend ratios of donor and acceptor components, we found that initial blend compositions that are symmetric with respect to the miscibility gap demonstrated higher PCE. Although we have assumed that spinodal decomposition to be responsible for phase-transformation, some studies have reported nucleation and growth to be the mechanism, particularly for asymmetric blend compositions [200]. This sets the motivation for a challenging future work involving more variegated microstructures consisting of additional phases other than

8. CONCLUSIONS & OUTLOOK

polymer and fullerene.

List of Publications and Conferences

Journal publications

- Kaka, Fiyanshu, Khanna, Sumeet, Ramamurthy, Praveen C. and Choudhury, Abhik, 2020. Investigation of process–structure–property relationship in ternary organic photovoltaics. *Journal of Applied Physics*, 128(14), p.145501.
- Kaka, Fiyanshu, Singh, Ravi K., Ramamurthy, Praveen C. and Choudhury, Abhik, 2020. Modeling process–structure–property relationship in organic photovoltaics using a robust diffuse interface approach. *AIP Advances*, 10(6), p.065304.

Conferences

- Kaka, Fiyanshu, Singh, Ravi K., Ramamurthy, Praveen C. and Choudhury, Abhik, 2018. Optimising characteristics of morphology to improve the performance of polymer solar cells. MRS 2019 Fall Meeting, Boston, USA.
- Kaka, Fiyanshu, Singh, Ravi K., Ramamurthy, Praveen C. and Choudhury, Abhik, 2018. Designing polymer blends for photovoltaic applications. ICEE 2018, IEEE Conference Proceedings, Bangalore, India.
- Kaka, Fiyanshu, Garg, Kavita, Ramamurthy, Praveen C. and Choudhury, Abhik, 2017. Deciphering the mechanism of phase separation in organic photovoltaics. IWAM 2017, RAK-CAM, UAE.
- Kaka, Fiyanshu, Ramamurthy, Praveen C. and Choudhury, Abhik, 2017. Design of Multi-Component blends for Photovoltaic applications. NMD-ATM 2017, Goa, India.

Appendices

Appendix A

Phase equilibrium calculation

The bulk thermodynamics of the ternary system have been captured using Flory-Huggins free energy function.

$$f(\phi_a, \phi_b, \phi_c) = \chi_{ab}\phi_a\phi_b + \chi_{bc}\phi_b\phi_c + \chi_{ca}\phi_c\phi_a + \frac{\phi_a}{N_a} \log \phi_a + \frac{\phi_b}{N_b} \log \phi_b + \frac{\phi_c}{N_c} \log \phi_c, \quad (1)$$

In order to find the two-phase equilibrium between the components we solve for the following equations using the constraint $\phi_a + \phi_b + \phi_c = 1$:

$$\begin{aligned} \mu_a^\alpha &= \mu_a^\beta, \\ \mu_b^\alpha &= \mu_b^\beta, \\ \psi^\alpha &= \psi^\beta, \end{aligned} \quad (2)$$

where μ_i^j represents the diffusional potential of i^{th} component in j^{th} phase and ψ^j denotes the grand potential of j^{th} phase.

The expressions for diffusion potential, $\mu_i = \frac{\partial f}{\partial \phi_i}$ read as,

$$\begin{aligned} \mu_a &= \ln \frac{\phi_a}{N_a} + \frac{1}{N_a} - \frac{1}{N_c} \ln(1 - \phi_a - \phi_b) - \frac{1}{N_c} + \phi_b(\chi_{ab} - \chi_{bc}) + \chi_{ca}(1 - 2\phi_a - \phi_b), \\ \mu_b &= \ln \frac{\phi_b}{N_b} + \frac{1}{N_b} - \frac{1}{N_c} \ln(1 - \phi_a - \phi_b) - \frac{1}{N_c} + \phi_a(\chi_{ab} - \chi_{ca}) + \chi_{bc}(1 - \phi_a - 2\phi_b), \end{aligned} \quad (3)$$

The grand potential, $\psi = f - \sum_i^{a,b} \mu_i \phi_i$ is given by,

$$\begin{aligned} \psi &= \chi_{ab}\phi_a\phi_b + \chi_{bc}\phi_b\phi_c + \chi_{ca}\phi_c\phi_a + \frac{\phi_a}{N_a} \log \phi_a + \frac{\phi_b}{N_b} \log \phi_b + \frac{\phi_c}{N_c} \log \phi_c \\ &\quad - \phi_a \left[\ln \frac{\phi_a}{N_a} + \frac{1}{N_a} - \frac{1}{N_c} \ln(1 - \phi_a - \phi_b) - \frac{1}{N_c} + \phi_b(\chi_{ab} - \chi_{bc}) + \chi_{ca}(1 - 2\phi_a - \phi_b) \right] \\ &\quad - \phi_b \left[\ln \frac{\phi_b}{N_b} + \frac{1}{N_b} - \frac{1}{N_c} \ln(1 - \phi_a - \phi_b) - \frac{1}{N_c} + \phi_a(\chi_{ab} - \chi_{ca}) + \chi_{bc}(1 - \phi_a - 2\phi_b) \right] \end{aligned} \quad (4)$$

Upon substituting the expressions for diffusion and grand potential and doing the algebra,

the equations reduce to:

$$\begin{aligned}
& \frac{1}{N_a} \ln \left(\frac{\phi_a^\alpha}{\phi_a^\beta} \right) - \frac{1}{N_c} \ln \left(\frac{1 - \phi_a^\alpha - \phi_b^\alpha}{1 - \phi_a^\beta - \phi_b^\beta} \right) + \chi_{ab} (\phi_b^\alpha - \phi_b^\beta) \\
& \quad - \chi_{bc} (\phi_b^\alpha - \phi_b^\beta) + \chi_{ca} (2\phi_a^\beta + \phi_b^\beta - 2\phi_a^\alpha - \phi_b^\alpha) = 0, \\
& \frac{1}{N_b} \ln \left(\frac{\phi_b^\alpha}{\phi_b^\beta} \right) - \frac{1}{N_c} \ln \left(\frac{1 - \phi_a^\alpha - \phi_b^\alpha}{1 - \phi_a^\beta - \phi_b^\beta} \right) + \chi_{ab} (\phi_a^\alpha - \phi_a^\beta) \\
& \quad + \chi_{bc} (2\phi_b^\beta + \phi_b^\beta - 2\phi_b^\alpha - \phi_a^\alpha) - \chi_{ca} (\phi_a^\alpha - \phi_a^\beta) = 0, \\
& \chi_{bc} [\phi_b^\alpha (1 - \phi_a^\alpha - \phi_b^\alpha) - \phi_b^\beta (1 - \phi_a^\beta - \phi_b^\beta)] + \chi_{ca} [\phi_a^\alpha (1 - \phi_a^\alpha - \phi_b^\alpha) - \phi_a^\beta (1 - \phi_a^\beta - \phi_b^\beta)] \\
& \quad - \phi_a^\alpha [\chi_{ca} (1 - 2\phi_a^\alpha - \phi_b^\alpha) - \chi_{bc} \phi_b^\alpha] - \phi_b^\alpha [\chi_{bc} (1 - \phi_a^\alpha - 2\phi_b^\alpha) - \chi_{ca} \phi_a^\alpha] \\
& \quad + \phi_a^\beta [\chi_{ca} (1 - 2\phi_a^\beta - \phi_b^\beta) - \chi_{bc} \phi_b^\beta] + \phi_b^\beta [\chi_{bc} (1 - \phi_a^\beta - 2\phi_b^\beta) - \chi_{ca} \phi_a^\beta] = 0
\end{aligned} \tag{5}$$

These equations are then solved in a coupled manner using GNU Octave [205] to derive the phase-diagram.

Appendix B

Fermi level calculation

In order to derive the Fermi-levels (E_i^α) of a phase, such that the system is in equilibrium for the given choice of compositions, we equate the electrochemical potential of each species in various phases i.e, $\tilde{\mu}_i^\alpha = \tilde{\mu}_i^\beta = \tilde{\mu}_i^\gamma = \dots = \tilde{\mu}_i^N$. Since in this work, two species (electron and hole) and three phases (polymer, fullerene and ternary acceptor) have been considered, the unknown Fermi-levels that can be derived by solving,

$$\begin{aligned}\tilde{\mu}_e^{Polymer} &= \tilde{\mu}_e^{Fullerene} \\ \tilde{\mu}_e^{Ternary} &= \tilde{\mu}_e^{Polymer} \\ \tilde{\mu}_h^{Polymer} &= \tilde{\mu}_h^{Fullerene} \\ \tilde{\mu}_h^{Ternary} &= \tilde{\mu}_h^{Polymer},\end{aligned}\tag{6}$$

Upon substituting $\tilde{\mu}_i = RT \ln x_i^\alpha + E_i^\alpha + q_i \xi$, the preceding equation reads as,

$$\begin{aligned}E_e^{Polymer} &= E_e^{Fullerene} + RT \ln \frac{x_e^{Fullerene}}{x_e^{Polymer}} + q_e V_{bi}^{pf} \\ E_e^{Ternary} &= E_e^{Polymer} + RT \ln \frac{x_e^{Polymer}}{x_e^{Ternary}} + q_e V_{bi}^{pt} \\ E_h^{Polymer} &= E_h^{Fullerene} + RT \ln \frac{x_h^{Fullerene}}{x_h^{Polymer}} + q_h V_{bi}^{pf} \\ E_h^{Ternary} &= E_h^{Polymer} + RT \ln \frac{x_h^{Polymer}}{x_h^{Ternary}} + q_h V_{bi}^{pt}.\end{aligned}\tag{7}$$

where, the built-in potentials are given by $V_{bi}^{pf} = (\xi^{Fullerene} - \xi^{Polymer})_{eq}$ and $V_{bi}^{pt} = (\xi^{Ternary} - \xi^{Polymer})_{eq}$. Therefore, given the built-in potentials, initial carrier compositions and upon pinning fullerene Fermi-levels ($E_e^{Fullerene}$ and $E_h^{Fullerene}$) to zero, the remaining 4 unknown Fermi-levels ($E_e^{Polymer}$, $E_e^{Ternary}$, $E_h^{Polymer}$ and $E_h^{Ternary}$) can be computed.

Bibliography

- [1] Ching W Tang. Two-layer organic photovoltaic cell. *Applied physics letters*, 48(2):183–185, 1986. [ii](#), [2](#)
- [2] Yuanbao Lin, Begimai Adilbekova, Yuliar Firdaus, Emre Yengel, Hendrik Faber, Muhammad Sajjad, Xiaopeng Zheng, Emre Yarali, Akmaral Seitkhan, Osman M Bakr, et al. 17% efficient organic solar cells based on liquid exfoliated WS₂ as a replacement for PE-DOT:PSS. *Advanced Materials*, 2019. [ii](#), [7](#), [17](#)
- [3] Brent L Adams, Xiang Carl Gao, and Surya R Kalidindi. Finite approximations to the second-order properties closure in single phase polycrystals. *Acta Materialia*, 53(13):3563–3577, 2005. [iv](#), [10](#), [76](#)
- [4] David T Fullwood, Surya R Kalidindi, Stephen R Niezgoda, Alan Fast, and Neil Hampson. Gradient-based microstructure reconstructions from distributions using fast Fourier transforms. *Materials Science and Engineering: A*, 494(1-2):68–72, 2008. [iv](#), [10](#), [76](#)
- [5] David T Fullwood, Stephen R Niezgoda, and Surya R Kalidindi. Microstructure reconstructions from 2-point statistics using phase-recovery algorithms. *Acta Materialia*, 56(5):942–948, 2008. [iv](#), [10](#), [11](#), [76](#)
- [6] David T Fullwood, Stephen R Niezgoda, Brent L Adams, and Surya R Kalidindi. Microstructure sensitive design for performance optimization. *Progress in Materials Science*, 55(6):477–562, 2010. [iv](#), [10](#), [11](#), [76](#)
- [7] Stephen R Niezgoda, Surya R Kalidindi, Xiaohua Hu, Gordana A Cingara, David S Wilkinson, Mukesh Jain, Peidong Wu, Raja K Mishra, M Arafat, and J Szpunar. Applications of the phase-coded generalized hough transform to feature detection, analysis, and segmentation of digital microstructures. *Computers, Materials, & Continua*, 14(2):79–98, 2010. [iv](#), [10](#), [76](#)

BIBLIOGRAPHY

- [8] Stephen R Niezgoda, Anand K Kanjarla, and Surya R Kalidindi. Novel microstructure quantification framework for databasing, visualization, and analysis of microstructure data. *Integrating Materials and Manufacturing Innovation*, 2(1):54–80, 2013. [iv](#), [10](#), [11](#), [76](#)
- [9] Akash Gupta, Ahmet Cecen, Sharad Goyal, Amarendra K Singh, and Surya R Kalidindi. Structure–property linkages using a data science approach: application to a non-metallic inclusion/steel composite system. *Acta Materialia*, 91:239–254, 2015. [iv](#), [10](#), [11](#), [76](#)
- [10] Ahmet Çeçen, Tony Fast, Emin C Kumbur, and Surya R Kalidindi. A data-driven approach to establishing microstructure–property relationships in porous transport layers of polymer electrolyte fuel cells. *Journal of Power Sources*, 245:144–153, 2014. [iv](#), [10](#), [11](#), [76](#)
- [11] Daniel Lincot. The new paradigm of photovoltaics: From powering satellites to powering humanity. *Comptes Rendus Physique*, 18(7-8):381–390, 2017. [1](#)
- [12] ME Becquerel. Mémoire sur les effets électriques produits sous l'influence des rayons solaires. *Comptes rendus hebdomadaires des séances de l'Académie des sciences*, 9:561–567, 1839. [1](#)
- [13] William Grylls Adams and Richard Evan Day. V. the action of light on selenium. *Proceedings of the Royal Society of London*, 25(171-178):113–117, 1877. [1](#)
- [14] Martin A Green. Photovoltaic principles. *Physica E: Low-dimensional Systems and Nanostructures*, 14(1-2):11–17, 2002. [1](#)
- [15] A Einstein. Einstein's proposal of the photon conceptfia translation of the annalen der physik paper of 1905. *Ann. Physik*, 17:132, 1905. [1](#)
- [16] Anna Köhler and Heinz Bässler. *Electronic processes in organic semiconductors: An introduction*. John Wiley & Sons, 2015. [1](#)
- [17] Alfred Pochettino. Sul comportamento foto-elettrico dell'antracene. *Acad. Lincei Rend.* 15:355, 1906. [1](#)
- [18] J Koenigsberger and K Schilling. Über elektrizitätsleitung in festen elementen und verbindungen. i. minima des widerstandes, prüfung auf elektronenleitung, anwendung der dissoziationsformeln. *Annalen der Physik*, 337(6):179–230, 1910. [1](#)

BIBLIOGRAPHY

- [19] WE Pauli. Lichtelektrische untersuchungen an fluoreszierenden substanzen. *Annalen der Physik*, 345(4):677–700, 1913. [1](#)
- [20] A Bernanose, M Comte, and P Vouaux. A new method of emission of light by certain organic compounds. *J. Chim. Phys*, 50:64–68, 1953. [2](#)
- [21] David Kearns and Melvin Calvin. Photovoltaic effect and photoconductivity in laminated organic systems. *The Journal of chemical physics*, 29(4):950–951, 1958. [2](#)
- [22] Daryl M Chapin, CS Fuller, and GL Pearson. A new silicon p-n junction photocell for converting solar radiation into electrical power. *Journal of Applied Physics*, 25(5):676–677, 1954. [2](#)
- [23] Martin Pope, HP Kallmann, and PJ Magnante. Electroluminescence in organic crystals. *The Journal of Chemical Physics*, 38(8):2042–2043, 1963. [2](#)
- [24] W Helfrich and WG Schneider. Transients of volume-controlled current and of recombination radiation in anthracene. *The Journal of Chemical Physics*, 44(8):2902–2909, 1966. [2](#)
- [25] Ching W Tang and Steven A VanSlyke. Organic electroluminescent diodes. *Applied physics letters*, 51(12):913–915, 1987. [2](#)
- [26] Jeremy H Burroughes, Donal DC Bradley, AR Brown, RN Marks, K Mackay, Richard H Friend, PL Burns, and AB Holmes. Light-emitting diodes based on conjugated polymers. *nature*, 347(6293):539–541, 1990. [2](#)
- [27] Chwan K Chiang, CR Fincher Jr, Yung W Park, Alan J Heeger, Hideki Shirakawa, Edwin J Louis, Shek C Gau, and Alan G MacDiarmid. Electrical conductivity in doped polyacetylene. *Physical review letters*, 39(17):1098, 1977. [2](#)
- [28] Masahiro Hiramoto, Hiroshi Fujiwara, and Masaaki Yokoyama. Three-layered organic solar cell with a photoactive interlayer of codeposited pigments. *Applied physics letters*, 58(10):1062–1064, 1991. [2](#)
- [29] Masahiro Hiramoto, Hiroshi Fujiwara, and Masaaki Yokoyama. p-i-n like behavior in three-layered organic solar cells having a co-deposited interlayer of pigments. *Journal of applied physics*, 72(8):3781–3787, 1992. [2](#)

BIBLIOGRAPHY

- [30] Niyazi S Sariciftci, L Smilowitz, Alan J Heeger, and F Wudl. Photoinduced electron transfer from a conducting polymer to buckminsterfullerene. *Science*, 258(5087):1474–1476, 1992. [2](#)
- [31] Gang Yu, Jun Gao, Jan C Hummelen, Fred Wudl, and Alan J Heeger. Polymer photovoltaic cells: enhanced efficiencies via a network of internal donor-acceptor heterojunctions. *Science*, 270(5243):1789–1791, 1995. [2](#), [12](#)
- [32] Safa Kasap and Peter Capper. *Springer handbook of electronic and photonic materials*. Springer, 2017. [3](#)
- [33] RA Street, Sarah Cowan, and AJ Heeger. Experimental test for geminate recombination applied to organic solar cells. *Physical Review B*, 82(12):121301, 2010. [3](#)
- [34] Nicholas E Jackson, Brett M Savoie, Tobin J Marks, Lin X Chen, and Mark A Ratner. The next breakthrough for organic photovoltaics? *The journal of physical chemistry letters*, 6(1):77–84, 2014. [4](#), [20](#)
- [35] Boyuan Qi and Jizheng Wang. Fill factor in organic solar cells. *Physical Chemistry Chemical Physics*, 15(23):8972–8982, 2013. [5](#)
- [36] Sarah R Cowan, Anshuman Roy, and Alan J Heeger. Recombination in polymer-fullerene bulk heterojunction solar cells. *Physical Review B*, 82(24):245207, 2010. [6](#)
- [37] Alan J Heeger. 25th anniversary article: bulk heterojunction solar cells: understanding the mechanism of operation. *Advanced Materials*, 26(1):10–28, 2014. [6](#), [17](#)
- [38] Makoto Karakawa, Kenji Suzuki, Takayuki Kuwabara, Tetsuya Taima, Keiji Nagai, Masahiro Nakano, Takahiro Yamaguchi, and Kohshin Takahashi. Factors contributing to degradation of organic photovoltaic cells. *Organic Electronics*, 76:105448, 2020. [7](#)
- [39] Rico Meitzner, Tobias Faber, Shahidul Alam, Aman Amand, Roland Roesch, Mathias Büttner, Felix Herrmann-Westendorf, Martin Presselt, Laura Ciammaruchi, Iris Visoly-Fisher, et al. Impact of p3ht materials properties and layer architecture on opv device stability. *Solar Energy Materials and Solar Cells*, 202:110151, 2019. [7](#)
- [40] Leiping Duan and Ashraf Uddin. Progress in stability of organic solar cells. *Advanced Science*, page 1903259. [7](#), [12](#)

BIBLIOGRAPHY

- [41] Nicola Gasparini, Alberto Salleo, Iain McCulloch, and Derya Baran. The role of the third component in ternary organic solar cells. *Nature Reviews Materials*, 4(4):229–242, 2019. [8](#), [18](#)
- [42] Derya Baran, Raja Shahid Ashraf, David A Hanifi, Maged Abdelsamie, Nicola Gasparini, Jason A Röhr, Sarah Holliday, Andrew Wadsworth, Sarah Lockett, Marios Neophytou, et al. Reducing the efficiency–stability–cost gap of organic photovoltaics with highly efficient and stable small molecule acceptor ternary solar cells. *Nature materials*, 16(3):363–369, 2017. [8](#), [17](#)
- [43] Amaia Diaz de Zerio Mendaza, Armantas Melianas, Ferry AA Nugroho, Olof Bäcke, Eva Olsson, Christoph Langhammer, Olle Inganäs, and Christian Müller. A fullerene alloy based photovoltaic blend with a glass transition temperature above 200 °C. *Journal of Materials Chemistry A*, 5(8):4156–4162, 2017. [8](#)
- [44] Wenyan Su, Qunping Fan, Xia Guo, Xiangyi Meng, Zhaozhao Bi, Wei Ma, Maojie Zhang, and Yongfang Li. Two compatible nonfullerene acceptors with similar structures as alloy for efficient ternary polymer solar cells. *Nano Energy*, 38:510–517, 2017. [8](#)
- [45] JD Van der Waals. Thermodynamische theorie der kapillarität unter voraussetzung stetiger dichteänderung. *Zeitschrift für Physikalische Chemie*, 13(1):657–725, 1894. [9](#)
- [46] JS Rowlinson. Translation of JD van der Waals’ “the thermodynamik theory of capillarity under the hypothesis of a continuous variation of density”. *Journal of Statistical Physics*, 20(2):197–200, 1979. [9](#)
- [47] John W Cahn and John E Hilliard. Free energy of a nonuniform system. I. interfacial free energy. *The Journal of chemical physics*, 28(2):258–267, 1958. [9](#)
- [48] John W Cahn. On spinodal decomposition. *Acta metallurgica*, 9(9):795–801, 1961. [9](#)
- [49] Samuel M Allen and John W Cahn. A microscopic theory for antiphase boundary motion and its application to antiphase domain coarsening. *Acta metallurgica*, 27(6):1085–1095, 1979. [9](#)
- [50] Long-Qing Chen and Wei Yang. Computer simulation of the domain dynamics of a quenched system with a large number of nonconserved order parameters: The grain-growth kinetics. *Physical Review B*, 50(21):15752, 1994. [9](#)

BIBLIOGRAPHY

- [51] Ingo Steinbach, Franco Pezzolla, Britta Nestler, Markus Seeßelberg, Robert Prieler, Georg J Schmitz, and Joao LL Rezende. A phase field concept for multiphase systems. *Physica D: Nonlinear Phenomena*, 94(3):135–147, 1996. [9](#)
- [52] Mark T Lusk. A phase-field paradigm for grain growth and recrystallization. *Proceedings of the Royal Society of London. Series A: Mathematical, Physical and Engineering Sciences*, 455(1982):677–700, 1999. [9](#)
- [53] Ryo Kobayashi, James A Warren, and W Craig Carter. A continuum model of grain boundaries. *Physica D: Nonlinear Phenomena*, 140(1-2):141–150, 2000. [9](#)
- [54] Chaitanya Joshi, TA Abinandanan, Rajdip Mukherjee, and Abhik Choudhury. Destabilisation of nanoporous membranes through gb grooving and grain growth. *Computational Materials Science*, 139:75–83, 2017. [9](#)
- [55] Dong Wang, Yunzhi Wang, Zhen Zhang, and Xiaobing Ren. Modeling abnormal strain states in ferroelastic systems: the role of point defects. *Physical review letters*, 105(20):205702, 2010. [9](#)
- [56] YL Li, SY Hu, ZK Liu, and LQ Chen. Phase-field model of domain structures in ferroelectric thin films. *Applied Physics Letters*, 78(24):3878–3880, 2001. [9](#)
- [57] DJ Seol, SY Hu, YL Li, J Shen, KH Oh, and LQ Chen. Three-dimensional phase-field modeling of spinodal decomposition in constrained films. *Metals and Materials International*, 9(1):61–66, 2003. [9](#)
- [58] Jonathan E Guyer, William J Boettinger, James A Warren, and Geoffrey B McFadden. Phase field modeling of electrochemistry. I. equilibrium. *Physical Review E*, 69(2):021603, 2004. [9](#)
- [59] Jonathan E Guyer, William J Boettinger, James A Warren, and Geoffrey B McFadden. Phase field modeling of electrochemistry. II. kinetics. *Physical Review E*, 69(2):021604, 2004. [9](#)
- [60] BC Han, A Van der Ven, D Morgan, and G Ceder. Electrochemical modeling of intercalation processes with phase field models. *Electrochimica Acta*, 49(26):4691–4699, 2004. [9](#)

BIBLIOGRAPHY

- [61] Yasushi Shibuta, Yoshinao Okajima, and Toshio Suzuki. A phase-field simulation of bridge formation process in a nanometer-scale switch. *Scripta materialia*, 55(12):1095–1098, 2006. [9](#)
- [62] Wanida Pongsaksawad, Adam C Powell, and David Dussault. Phase-field modeling of transport-limited electrolysis in solid and liquid states. *Journal of The Electrochemical Society*, 154(6):F122–F133, 2007. [9](#)
- [63] Yoshinao Okajima, Yasushi Shibuta, and Toshio Suzuki. A phase-field model for electrode reactions with Butler–Volmer kinetics. *Computational materials science*, 50(1):118–124, 2010. [9](#)
- [64] Linyun Liang and Long-Qing Chen. Nonlinear phase field model for electrodeposition in electrochemical systems. *Applied Physics Letters*, 105(26):263903, 2014. [9](#)
- [65] Amel Slimani, Aicha Iratni, Hervé Henry, Mathis Plapp, Jean-Noël Chazalviel, François Ozanam, and Noureddine Gabouze. Macropore formation in p-type silicon: toward the modeling of morphology. *Nanoscale research letters*, 9(1):585, 2014. [9](#), [44](#)
- [66] IS Aranson, VA Kalatsky, and VM Vinokur. Continuum field description of crack propagation. *Physical review letters*, 85(1):118, 2000. [9](#)
- [67] Alain Karma, David A Kessler, and Herbert Levine. Phase-field model of mode III dynamic fracture. *Physical Review Letters*, 87(4):045501, 2001. [9](#)
- [68] Yulan Li, Shenyang Hu, Charles H Henager Jr, Huiqiu Deng, Fei Gao, Xin Sun, and Moe A Khaleel. Computer simulations of interstitial loop growth kinetics in irradiated bcc fe. *Journal of nuclear materials*, 427(1-3):259–267, 2012. [9](#)
- [69] Mohan Mahadevan and R Mark Bradley. Phase field model of surface electromigration in single crystal metal thin films. *Physica D: Nonlinear Phenomena*, 126(3-4):201–213, 1999. [9](#)
- [70] Deepali N Bhate, Ashish Kumar, and Allan F Bower. Diffuse interface model for electromigration and stress voiding. *Journal of Applied Physics*, 87(4):1712–1721, 2000. [9](#)
- [71] Deepali N Bhate, Allan F Bower, and Ashish Kumar. A phase field model for failure in interconnect lines due to coupled diffusion mechanisms. *Journal of the Mechanics and Physics of Solids*, 50(10):2057–2083, 2002. [9](#)

BIBLIOGRAPHY

- [72] Supriyo Chakraborty, Praveen Kumar, and Abhik Choudhury. Phase-field modeling of grain-boundary grooving and migration under electric current and thermal gradient. *Acta Materialia*, 153:377–390, 2018. [9](#)
- [73] Surya R Kalidindi. Data science and cyberinfrastructure: critical enablers for accelerated development of hierarchical materials. *International Materials Reviews*, 60(3):150–168, 2015. [10](#)
- [74] Lou Ross and John C Russ. The image processing handbook. *Microscopy and Microanalysis*, 17(5):843, 2011. [10](#)
- [75] EO Hall. The deformation and ageing of mild steel: III discussion of results. *Proceedings of the Physical Society. Section B*, 64(9):747, 1951. [10](#)
- [76] NJ Petch. The cleavage strength of polycrystals. *Journal of the Iron and Steel Institute*, 174:25–28, 1953. [10](#)
- [77] A. Argon. *Strengthening Mechanisms in Crystal Plasticity*. OSMM Series. OUP Oxford, 2008. [10](#)
- [78] Robert E Reed and HR Abbaschian. Physical metallurgy principles. *PWS Engineering, Boston, Massachusetts*, 1973. [10](#)
- [79] Geoffrey Ingram Taylor. Plastic strain in metals. *J. Inst. Metals*, 62:307–324, 1938. [10](#)
- [80] Jean Serra. A lattice approach to image segmentation. *Journal of Mathematical Imaging and Vision*, 24(1):83–130, 2006. [10](#)
- [81] JP Simmons, P Chuang, M Comer, JE Spowart, MD Uchic, and M De Graef. Application and further development of advanced image processing algorithms for automated analysis of serial section image data. *Modelling and Simulation in Materials Science and Engineering*, 17(2):025002, 2008. [10](#)
- [82] Mary Comer, Charles A Bouman, Marc De Graef, and Jeff P Simmons. Bayesian methods for image segmentation. *JOM*, 63(7):55, 2011. [10](#)
- [83] Jarrell Waggoner, Youjie Zhou, Jeff Simmons, Marc De Graef, and Song Wang. 3d materials image segmentation by 2d propagation: A graph-cut approach considering homomorphism. *IEEE transactions on image processing*, 22(12):5282–5293, 2013. [10](#)

BIBLIOGRAPHY

- [84] Markus Hütter, Gregory C Rutledge, and Robert C Armstrong. Crystal shapes and crystallization in continuum modeling. *Physics of Fluids*, 17(1):014107, 2005. [10](#)
- [85] Robert D MacPherson and David J Srolovitz. The Von Neumann relation generalized to coarsening of three-dimensional microstructures. *Nature*, 446(7139):1053–1055, 2007. [10](#)
- [86] J.P. MacSleyne, J.P. Simmons, and M. De Graef. On the use of 2-D moment invariants for the automated classification of particle shapes. *Acta Materialia*, 56(3):427 – 437, 2008. [10](#)
- [87] JP MacSleyne, JP Simmons, and M De Graef. On the use of moment invariants for the automated analysis of 3d particle shapes. *Modelling and Simulation in Materials Science and Engineering*, 16(4):045008, 2008. [10](#)
- [88] Stephen R Niezgoda, David M Turner, David T Fullwood, and Surya R Kalidindi. Optimized structure based representative volume element sets reflecting the ensemble-averaged 2-point statistics. *Acta Materialia*, 58(13):4432–4445, 2010. [10](#)
- [89] Stephen R Niezgoda, Yuksel C Yabansu, and Surya R Kalidindi. Understanding and visualizing microstructure and microstructure variance as a stochastic process. *Acta Materialia*, 59(16):6387–6400, 2011. [10](#)
- [90] Baskar Ganapathysubramanian and Nicholas Zabaras. Modeling diffusion in random heterogeneous media: Data-driven models, stochastic collocation and the variational multi-scale method. *Journal of Computational Physics*, 226(1):326–353, 2007. [10](#)
- [91] Baskar Ganapathysubramanian and Nicholas Zabaras. A non-linear dimension reduction methodology for generating data-driven stochastic input models. *Journal of Computational Physics*, 227(13):6612–6637, 2008. [10](#)
- [92] Surya R Kalidindi, Joshua A Gomberg, Zachary T Trautt, and Chandler A Becker. Application of data science tools to quantify and distinguish between structures and models in molecular dynamics datasets. *Nanotechnology*, 26(34):344006, 2015. [10](#)
- [93] David L McDowell and Richard A LeSar. The need for microstructure informatics in process–structure–property relations. *MRS Bulletin*, 41(8):587–593, 2016. [10](#)
- [94] Abhik Choudhury, Yuksel C Yabansu, Surya R Kalidindi, and Anne Dennstedt. Quantification and classification of microstructures in ternary eutectic alloys using 2-point spatial correlations and principal component analyses. *Acta Materialia*, 110:131–141, 2016. [11](#)

BIBLIOGRAPHY

- [95] Philipp Steinmetz, Yuksel C Yabansu, Johannes Hötzer, Marcus Jainta, Britta Nestler, and Surya R Kalidindi. Analytics for microstructure datasets produced by phase-field simulations. *Acta Materialia*, 103:192–203, 2016. [11](#)
- [96] Tony Fast, Stephen R Niezgoda, and Surya R Kalidindi. A new framework for computationally efficient structure–structure evolution linkages to facilitate high-fidelity scale bridging in multi-scale materials models. *Acta Materialia*, 59(2):699–707, 2011. [11](#), [19](#)
- [97] Tony Fast, Olga Wodo, Baskar Ganapathysubramanian, and Surya R Kalidindi. Microstructure taxonomy based on spatial correlations: Application to microstructure coarsening. *Acta Materialia*, 108:176–185, 2016. [11](#), [19](#)
- [98] David B Brough, Daniel Wheeler, and Surya R Kalidindi. Materials knowledge systems in python—a data science framework for accelerated development of hierarchical materials. *Integrating materials and manufacturing innovation*, 6(1):36–53, 2017. [11](#), [19](#)
- [99] Daniel Wheeler, David Brough, Tony Fast, Surya Kalidindi, and Andrew Reid. Pymks: materials knowledge system in python. 2014. [11](#), [19](#)
- [100] Pei Cheng, Gang Li, Xiaowei Zhan, and Yang Yang. Next-generation organic photovoltaics based on non-fullerene acceptors. *Nature Photonics*, 12(3):131–142, 2018. [12](#), [104](#)
- [101] Guangye Zhang, Jingbo Zhao, Philip CY Chow, Kui Jiang, Jianquan Zhang, Zonglong Zhu, Jie Zhang, Fei Huang, and He Yan. Nonfullerene acceptor molecules for bulk heterojunction organic solar cells. *Chemical reviews*, 118(7):3447–3507, 2018. [12](#), [104](#)
- [102] Christian B Nielsen, Sarah Holliday, Hung-Yang Chen, Samuel J Cryer, and Iain McCulloch. Non-fullerene electron acceptors for use in organic solar cells. *Accounts of chemical research*, 48(11):2803–2812, 2015. [12](#), [104](#)
- [103] Yuze Lin, Jiayu Wang, Zhi-Guo Zhang, Huitao Bai, Yongfang Li, Daoben Zhu, and Xiaowei Zhan. An electron acceptor challenging fullerenes for efficient polymer solar cells. *Advanced materials*, 27(7):1170–1174, 2015. [12](#), [104](#)
- [104] Katherine A Mazzio and Christine K Luscombe. The future of organic photovoltaics. *Chemical Society Reviews*, 44(1):78–90, 2014. [12](#), [104](#)

BIBLIOGRAPHY

- [105] Yongye Liang, Zheng Xu, Jiangbin Xia, Szu-Ting Tsai, Yue Wu, Gang Li, Claire Ray, and Luping Yu. For the bright future—bulk heterojunction polymer solar cells with power conversion efficiency of 7.4%. *Advanced materials*, 22(20):E135–E138, 2010. [12](#), [104](#)
- [106] Xiaoniu Yang, Joachim Loos, Sjoerd C Veenstra, Wiljan JH Verhees, Martijn M Wienk, Jan M Kroon, Matthias AJ Michels, and René AJ Janssen. Nanoscale morphology of high-performance polymer solar cells. *Nano letters*, 5(4):579–583, 2005. [12](#)
- [107] Vikas Negi, Olga Wodo, Jacobus J van Franeker, Rene AJ Janssen, and Peter A Bobbert. Simulating phase separation during spin coating of a polymer–fullerene blend: A joint computational and experimental investigation. *ACS Applied Energy Materials*, 1(2):725–735, 2018. [13](#), [14](#), [20](#), [33](#), [51](#), [84](#)
- [108] Olga Wodo and Baskar Ganapathysubramanian. How do evaporating thin films evolve? unravelling phase-separation mechanisms during solvent-based fabrication of polymer blends. *Applied Physics Letters*, 105(15):153104, 2014. [13](#), [51](#), [90](#)
- [109] Olga Wodo and Baskar Ganapathysubramanian. Modeling morphology evolution during solvent-based fabrication of organic solar cells. *Computational Materials Science*, 55:113–126, 2012. [13](#), [20](#), [33](#), [39](#), [51](#), [84](#)
- [110] Olga Wodo, Srikanta Tirthapura, Sumit Chaudhary, and Baskar Ganapathysubramanian. A graph-based formulation for computational characterization of bulk heterojunction morphology. *Organic Electronics*, 13(6):1105–1113, 2012. [13](#)
- [111] Biswajit Ray, Pradeep R Nair, and Muhammad A Alam. Annealing dependent performance of organic bulk-heterojunction solar cells: A theoretical perspective. *Solar Energy Materials and Solar Cells*, 95(12):3287–3294, 2011. [13](#), [14](#), [16](#), [18](#), [33](#)
- [112] Gavin A Buxton and Nigel Clarke. Predicting structure and property relations in polymeric photovoltaic devices. *Physical Review B*, 74(8):085207, 2006. [13](#), [14](#), [15](#), [16](#), [18](#), [33](#)
- [113] Wen Yin and Mark Dadmun. A new model for the morphology of P3HT/PCBM organic photovoltaics from small-angle neutron scattering: rivers and streams. *ACS nano*, 5(6):4756–4768, 2011. [13](#), [56](#)
- [114] Peter Kohn, Zhuxia Rong, Kai H Scherer, Alessandro Sepe, Michael Sommer, Peter Muller-Buschbaum, Richard H Friend, Ullrich Steiner, and Sven Huttner.

BIBLIOGRAPHY

- Crystallization-induced 10-nm structure formation in P3HT/PCBM blends. *Macromolecules*, 46(10):4002–4013, 2013. [13](#), [56](#)
- [115] Yan Yao, Jianhui Hou, Zheng Xu, Gang Li, and Yang Yang. Effects of solvent mixtures on the nanoscale phase separation in polymer solar cells. *Advanced Functional Materials*, 18(12):1783–1789, 2008. [13](#)
- [116] Jan Alstrup, Mikkel Jørgensen, Andrew J Medford, and Frederik C Krebs. Ultra fast and parsimonious materials screening for polymer solar cells using differentially pumped slot-die coating. *ACS Applied Materials & Interfaces*, 2(10):2819–2827, 2010. [13](#)
- [117] Franz Padinger, Roman S Rittberger, and Niyazi S Sariciftci. Effects of postproduction treatment on plastic solar cells. *Advanced Functional Materials*, 13(1):85–88, 2003. [13](#)
- [118] Gang Li, Vishal Shrotriya, Jinsong Huang, Yan Yao, Tom Moriarty, Keith Emery, and Yang Yang. High-efficiency solution processable polymer photovoltaic cells by self-organization of polymer blends. *Nature Materials*, 4(11):864–868, 2005. [13](#)
- [119] Peter K Watkins, Alison B Walker, and Geraldine LB Verschoor. Dynamical monte carlo modelling of organic solar cells: The dependence of internal quantum efficiency on morphology. *Nano letters*, 5(9):1814–1818, 2005. [14](#)
- [120] RA Marsh, Chris Groves, and Neil C Greenham. A microscopic model for the behavior of nanostructured organic photovoltaic devices. *Journal of applied physics*, 101(8):083509, 2007. [14](#)
- [121] Christopher R McNeill, Sebastian Westenhoff, Chris Groves, Richard H Friend, and Neil C Greenham. Influence of nanoscale phase separation on the charge generation dynamics and photovoltaic performance of conjugated polymer blends: Balancing charge generation and separation. *The Journal of Physical Chemistry C*, 111(51):19153–19160, 2007. [14](#)
- [122] C Groves, RA Marsh, and Neil C Greenham. Monte carlo modeling of geminate recombination in polymer-polymer photovoltaic devices. *The Journal of chemical physics*, 129(11):114903, 2008. [14](#)
- [123] Lingyi Meng, Yuan Shang, Qikai Li, Yongfang Li, Xiaowei Zhan, Zhigang Shuai, Robin GE Kimber, and Alison B Walker. Dynamic monte carlo simulation for highly efficient polymer blend photovoltaics. *The Journal of Physical Chemistry B*, 114(1):36–41, 2009. [14](#)

BIBLIOGRAPHY

- [124] Chris Groves, Robin GE Kimber, and Alison B Walker. Simulation of loss mechanisms in organic solar cells: A description of the mesoscopic monte carlo technique and an evaluation of the first reaction method. *The Journal of chemical physics*, 133(14):144110, 2010. [14](#)
- [125] Robin GE Kimber, Alison B Walker, Gerd E Schröder-Turk, and Douglas J Cleaver. Bi-continuous minimal surface nanostructures for polymer blend solar cells. *Physical Chemistry Chemical Physics*, 12(4):844–851, 2010. [14](#)
- [126] Cheng-Kuang Lee, Chun-Wei Pao, and Chih-Wei Chu. Multiscale molecular simulations of the nanoscale morphologies of p3ht: Pcbm blends for bulk heterojunction organic photovoltaic cells. *Energy & Environmental Science*, 4(10):4124–4132, 2011. [14](#)
- [127] Anton Pershin, Sergii Donets, and Stephan A Baeurle. A new multiscale modeling method for simulating the loss processes in polymer solar cell nanodevices. *The Journal of chemical physics*, 136(19):194102, 2012. [14](#)
- [128] Fanan Wei, Liming Liu, Lianqing Liu, and Guangyong Li. Multiscale modeling and simulation for optimizing polymer bulk heterojunction solar cells. In *2012 IEEE 38th Photovoltaic Specialists Conference (PVSC) PART 2*, pages 1–10. IEEE, 2012. [14](#)
- [129] Xiangchuan Meng, Lin Zhang, Yuanpeng Xie, Xiaotian Hu, Zhi Xing, Zengqi Huang, Cong Liu, Licheng Tan, Weihua Zhou, Yanming Sun, et al. A general approach for lab-to-manufacturing translation on flexible organic solar cells. *Advanced Materials*, 31(41):1903649, 2019. [14](#), [20](#)
- [130] James A Barker, Catherine M Ramsdale, and Neil C Greenham. Modeling the current-voltage characteristics of bilayer polymer photovoltaic devices. *Physical Review B*, 67(7):075205, 2003. [14](#), [18](#)
- [131] Lambert JA Koster, ECP Smits, VD Mihailetchi, and PWM Blom. Device model for the operation of polymer/fullerene bulk heterojunction solar cells. *Physical Review B*, 72(8):085205, 2005. [14](#), [18](#)
- [132] CM Martin, VM Burlakov, HE Assender, and DAR Barkhouse. A numerical model for explaining the role of the interface morphology in composite solar cells. *Journal of Applied Physics*, 102(10):104506, 2007. [14](#), [15](#), [18](#)
- [133] Jonny Williams and Alison B Walker. Two-dimensional simulations of bulk heterojunction solar cell characteristics. *Nanotechnology*, 19(42):424011, 2008. [14](#), [15](#), [18](#)

BIBLIOGRAPHY

- [134] Thomas Kirchartz, Bart E Pieters, Kurt Taretto, and Uwe Rau. Electro-optical modeling of bulk heterojunction solar cells. *Journal of applied physics*, 104(9):094513, 2008. [14](#), [15](#), [18](#)
- [135] Manas Shah and Venkat Ganesan. Correlations between morphologies and photovoltaic properties of rod- coil block copolymers. *Macromolecules*, 43(1):543–552, 2009. [14](#), [15](#), [18](#)
- [136] W Tress, M Furno, K Leo, and M Riede. Numerical drift-diffusion modeling of organic solar cells in comparison with experimental data series. In *Numerical Simulation of Optoelectronic Devices*, pages 33–34. IEEE, 2010. [14](#)
- [137] Mosè Casalegno, Guido Raos, and Riccardo Po. Methodological assessment of kinetic monte carlo simulations of organic photovoltaic devices: The treatment of electrostatic interactions. *The Journal of chemical physics*, 132(9):094705, 2010. [14](#)
- [138] Vikas Negi. *Exploring the process-structure-property relationship of organic solar cells by high performance computer simulations*. PhD thesis, Technische Universiteit Eindhoven, 2018. [14](#)
- [139] Miro Zeman, Joost van den Heuvel, BE Pieters, M Kroon, and J Willemen. Advanced semiconductor analysis. *TU Delft, The Netherlands*, 2003. [15](#)
- [140] JJM Van Der Holst, MA Uijtewaal, B Ramachandhran, Reinder Coehoorn, PA Bobbert, GA De Wijs, and RA De Groot. Modeling and analysis of the three-dimensional current density in sandwich-type single-carrier devices of disordered organic semiconductors. *Physical Review B*, 79(8):085203, 2009. [15](#), [18](#)
- [141] LJA Koster. Charge carrier mobility in disordered organic blends for photovoltaics. *Physical Review B*, 81(20):205318, 2010. [16](#), [18](#)
- [142] ZG Yu, DL Smith, A Saxena, RL Martin, and AR Bishop. Molecular geometry fluctuations and field-dependent mobility in conjugated polymers. *Physical Review B*, 63(8):085202, 2001. [16](#)
- [143] Donald L Scharfetter and Hermann K Gummel. Large-signal analysis of a silicon read diode oscillator. *IEEE Transactions on electron devices*, 16(1):64–77, 1969. [16](#)
- [144] Hari K Kodali and Baskar Ganapathysubramanian. Computer simulation of heterogeneous polymer photovoltaic devices. *Modelling and Simulation in Materials Science and Engineering*, 20(3):035015, 2012. [16](#), [18](#)

BIBLIOGRAPHY

- [145] Gavin A Buxton and Nigel Clarke. Computer simulation of polymer solar cells. *Modelling and simulation in materials science and engineering*, 15(2):13, 2006. [16](#)
- [146] Sankara Rao Gollu, Ramakant Sharma, G. Srinivas, Souvik Kundu, and Dipti Gupta. Incorporation of SiO₂ dielectric nanoparticles for performance enhancement in P3HT:PCBM inverted organic solar cells. *Organic Electronics*, 24:43 – 50, 2015. [16, 41](#)
- [147] Yu-Wei Su, Shang-Che Lan, and Kung-Hwa Wei. Organic photovoltaics. *Materials Today*, 15(12):554–562, 2012. [17](#)
- [148] Shaoqing Zhang, Long Ye, and Jianhui Hou. Breaking the 10% efficiency barrier in organic photovoltaics: Morphology and device optimization of well-known PBDTTT polymers. *Advanced Energy Materials*, 6(11):1502529, 2016. [17](#)
- [149] Tao Liu, Lijun Huo, Xiaobo Sun, Bingbing Fan, Yunhao Cai, Taehyo Kim, Jin Young Kim, Hyosung Choi, and Yanming Sun. Ternary organic solar cells based on two highly efficient polymer donors with enhanced power conversion efficiency. *Advanced Energy Materials*, 6(6):1502109, 2016. [17](#)
- [150] Luyao Lu, Mary Allison Kelly, Wei You, and Luping Yu. Status and prospects for ternary organic photovoltaics. *Nature Photonics*, 9(8):491–500, 2015. [17](#)
- [151] Tayebeh Ameri, Parisa Khoram, Jie Min, and Christoph J Brabec. Organic ternary solar cells: a review. *Advanced Materials*, 25(31):4245–4266, 2013. [17](#)
- [152] Lingxian Meng, Yamin Zhang, Xiangjian Wan, Chenxi Li, Xin Zhang, Yanbo Wang, Xin Ke, Zuo Xiao, Liming Ding, Ruoxi Xia, et al. Organic and solution-processed tandem solar cells with 17.3% efficiency. *Science*, 361(6407):1094–1098, 2018. [17](#)
- [153] Letian Dou, Jingbi You, Ziruo Hong, Zheng Xu, Gang Li, Robert A Street, and Yang Yang. 25th anniversary article: a decade of organic/polymeric photovoltaic research. *Advanced materials*, 25(46):6642–6671, 2013. [17](#)
- [154] Yusheng Chen, Pan Ye, Zhen-Gang Zhu, Xinlong Wang, Lei Yang, Xiaozhou Xu, Xiaoxi Wu, Tao Dong, Hao Zhang, Jianhui Hou, et al. Achieving high-performance ternary organic solar cells through tuning acceptor alloy. *Advanced Materials*, 29(6):1603154, 2017. [17](#)
- [155] Tao Liu, Yuan Guo, Yuanping Yi, Lijun Huo, Xiaonan Xue, Xiaobo Sun, Huiting Fu, Wentao Xiong, Dong Meng, Zhaohui Wang, et al. Ternary organic solar cells based on

BIBLIOGRAPHY

- two compatible nonfullerene acceptors with power conversion efficiency > 10%. *Advanced Materials*, 28(45):10008–10015, 2016. 17
- [156] Sonya A Mollinger, Koen Vandewal, and Alberto Salleo. Microstructural and electronic origins of open-circuit voltage tuning in organic solar cells based on ternary blends. *Advanced Energy Materials*, 5(23):1501335, 2015. 17
- [157] Petr P Khlyabich, Beate Burkhardt, and Barry C Thompson. Efficient ternary blend bulk heterojunction solar cells with tunable open-circuit voltage. *Journal of the American Chemical Society*, 133(37):14534–14537, 2011. 17
- [158] Luyao Lu, Tao Xu, Wei Chen, Erik S Landry, and Luping Yu. Ternary blend polymer solar cells with enhanced power conversion efficiency. *Nature Photonics*, 8(9):716, 2014. 17
- [159] Balaji Sesha Sarath Pokuri, Sambuddha Ghosal, Apurva Kokate, Soumik Sarkar, and Baskar Ganapathysubramanian. Interpretable deep learning for guided microstructure–property explorations in photovoltaics. *npj Computational Materials*, 5(1):1–11, 2019. 18
- [160] Dylan Kipp, Olga Wodo, Baskar Ganapathysubramanian, and Venkat Ganesan. Utilizing morphological correlators for device performance to optimize ternary blend organic solar cells based on block copolymer additives. *Solar Energy Materials and Solar Cells*, 161:206–218, 2017. 18, 90
- [161] Olga Wodo, Jaroslaw Zola, Balaji Sesha Sarath Pokuri, Pengfei Du, and Baskar Ganapathysubramanian. Automated, high throughput exploration of process–structure–property relationships using the mapreduce paradigm. *Materials discovery*, 1:21–28, 2015. 18
- [162] Frederik C Krebs. Fabrication and processing of polymer solar cells: a review of printing and coating techniques. *Solar energy materials and solar cells*, 93(4):394–412, 2009. 19
- [163] Riccardo Po, Andrea Bernardi, Anna Calabrese, Chiara Carbonera, Gianni Corso, and Andrea Pellegrino. From lab to fab: how must the polymer solar cell materials design change?—an industrial perspective. *Energy & Environmental Science*, 7(3):925–943, 2014. 19
- [164] Anke Teichler, Jolke Perelaer, and Ulrich S Schubert. Inkjet printing of organic electronics—comparison of deposition techniques and state-of-the-art developments. *Journal of Materials Chemistry C*, 1(10):1910–1925, 2013. 20

BIBLIOGRAPHY

- [165] Roar Søndergaard, Markus Hösel, Dechan Angmo, Thue T Larsen-Olsen, and Frederik C Krebs. Roll-to-roll fabrication of polymer solar cells. *Materials today*, 15(1-2):36–49, 2012. [20](#)
- [166] Gang Li, Rui Zhu, and Yang Yang. Polymer solar cells. *Nature photonics*, 6(3):153–161, 2012. [20](#)
- [167] Ying Diao, Leo Shaw, Zhenan Bao, and Stefan CB Mannsfeld. Morphology control strategies for solution-processed organic semiconductor thin films. *Energy & Environmental Science*, 7(7):2145–2159, 2014. [20](#)
- [168] Gang Li, Vishal Shrotriya, Jinsong Huang, Yan Yao, Tom Moriarty, Keith Emery, and Yang Yang. High-efficiency solution processable polymer photovoltaic cells by self-organization of polymer blends. In *Materials For Sustainable Energy: A Collection of Peer-Reviewed Research and Review Articles from Nature Publishing Group*, pages 80–84. World Scientific, 2011. [20](#)
- [169] Dian Chen, Atsuhiro Nakahara, Dongguang Wei, Dennis Nordlund, and Thomas P Russell. P3HT/PCBM bulk heterojunction organic photovoltaics: correlating efficiency and morphology. *Nano letters*, 11(2):561–567, 2011. [20](#)
- [170] Dylan Kipp and Venkat Ganesan. Influence of block copolymer compatibilizers on the morphologies of semiflexible polymer/solvent blends. *The Journal of Physical Chemistry B*, 118(16):4425–4441, 2014. [20](#)
- [171] Garyfalia A Zoumpouli and Stergios G Yiantsios. Hydrodynamic effects on phase separation morphologies in evaporating thin films of polymer solutions. *Physics of Fluids*, 28(8):082108, 2016. [20](#)
- [172] Charley Schaefer, Jasper J Michels, and PPAM van der Schoot. Structuring of thin-film polymer mixtures upon solvent evaporation. *Macromolecules*, 49(18):6858–6870, 2016. [20](#)
- [173] John Cummings, John S Lowengrub, Bobby G Sumpter, Steven M Wise, and Rajeev Kumar. Modeling solvent evaporation during thin film formation in phase separating polymer mixtures. *Soft Matter*, 14(10):1833–1846, 2018. [20](#)
- [174] Spencer Pfeifer, Olga Wodo, and Baskar Ganapathysubramanian. An optimization approach to identify processing pathways for achieving tailored thin film morphologies. *Computational Materials Science*, 143:486–496, 2018. [20](#)

BIBLIOGRAPHY

- [175] Olivier JJ Ronsin, DongJu Jang, Hans-Joachim Egelhaaf, Christoph J Brabec, and Jens Harting. A phase-field model for the evaporation of thin film mixtures. *Physical Chemistry Chemical Physics*, 22(12):6638–6652, 2020. [20](#)
- [176] Spencer Pfeifer, Balaji Sesha Sarath Pokuri, Pengfei Du, and Baskar Ganapathysubramanian. Process optimization for microstructure-dependent properties in thin film organic electronics. *Materials Discovery*, 11:6–13, 2018. [20](#)
- [177] Xiaotian Hu, Lie Chen, and Yiwang Chen. Universal and versatile moo_3 -based hole transport layers for efficient and stable polymer solar cells. *The Journal of Physical Chemistry C*, 118(19):9930–9938, 2014. [22](#)
- [178] Chris Jacobsen, S Wirick, G Flynn, and C Zimba. Soft x-ray spectroscopy from image sequences with sub-100 nm spatial resolution. *Journal of Microscopy*, 197(2):173–184, 2000. [27](#)
- [179] Saswata Bhattacharyya. *Evolution Of Multivariant Microstructures With Anisotropic Misfit*. PhD thesis, Indian Institute of Science, 2009. [33](#)
- [180] Min Kim, Jaewon Lee, Sae Byeok Jo, Dong Hun Sin, Hyomin Ko, Hansol Lee, Seung Goo Lee, and Kilwon Cho. Critical factors governing vertical phase separation in polymer-PCBM blend films for organic solar cells. *Journal of Materials Chemistry A*, 4(40):15522–15535, 2016. [39](#)
- [181] Franco Cataldo. On the solubility parameter of C_{60} and higher fullerenes. *Fullerenes, Nanotubes and Carbon Nanostructures*, 17(2):79–84, 2009. [39](#), [47](#)
- [182] Z Nevin Gerek and J Richard Elliott. Self-diffusivity estimation by molecular dynamics. *Industrial & engineering chemistry research*, 49(7):3411–3423, 2010. [39](#)
- [183] Long Qing Chen, Jie Shen, et al. Applications of semi-implicit Fourier-spectral method to phase field equations. *Computer Physics Communications*, 108(2):147–158, 1998. [39](#)
- [184] LJA Koster, VD Mihailescu, and PWM Blom. Bimolecular recombination in polymer/fullerene bulk heterojunction solar cells. *Applied physics letters*, 88(5):052104, 2006. [46](#)
- [185] Zuo Xiao, Xue Jia, and Liming Ding. Ternary organic solar cells offer 14% power conversion efficiency. *Sci. Bull.*, 62(23):1562–1564, 2017. [47](#)

BIBLIOGRAPHY

- [186] Samuel Foster, Florent Deledalle, Akiko Mitani, Toshio Kimura, Ki-Beom Kim, Takayuki Okachi, Thomas Kirchartz, Jun Oguma, Kunihito Miyake, James R Durrant, et al. Electron collection as a limit to polymer:PCBM solar cell efficiency: Effect of blend microstructure on carrier mobility and device performance in PTB7:PCBM. *Advanced energy materials*, 4(14):1400311, 2014. [47](#)
- [187] Sun-Joo Park, Kwan-Yong Lee, Do-Hyun Kim, Min-Ho Shin, and Young-Joo Kim. Improvement of electrical conductivity for high-performance organic solar cells by multi-temperature solvent annealing. *Japanese Journal of Applied Physics*, 54(4S):04DK07, 2015. [47](#)
- [188] OpenCFD Limited. OpenFOAM User Guide. 2018. [49](#)
- [189] Matteo Nicoli, Mathis Plapp, and Hervé Henry. Tensorial mobilities for accurate solution of transport problems in models with diffuse interfaces. *Physical Review E*, 84(4):046707, 2011. [49](#)
- [190] J Ettrich, A Choudhury, O Tschukin, E Schoof, A August, and B Nestler. Modelling of transient heat conduction with diffuse interface methods. *Modelling and Simulation in Materials Science and Engineering*, 22(8):085006, 2014. [49](#)
- [191] Dylan Kipp, Jorge Mok, Joseph Strzalka, Seth B Darling, Venkat Ganesan, and Rafael Verduzco. Rational design of thermally stable, bicontinuous donor/acceptor morphologies with conjugated block copolymer additives. *ACS Macro Letters*, 4(9):867–871, 2015. [51](#)
- [192] Brian A Collins, Zhe Li, John R Tumbleston, Eliot Gann, Christopher R McNeill, and Harald Ade. Absolute measurement of domain composition and nanoscale size distribution explains performance in ptb7: P_c71bm solar cells. *Advanced Energy Materials*, 3(1):65–74, 2013. [51](#)
- [193] Jacobus J Van Franeker, Mathieu Turbiez, Weiwei Li, Martijn M Wienk, and René AJ Janssen. A real-time study of the benefits of co-solvents in polymer solar cell processing. *Nature communications*, 6:6229, 2015. [51, 56](#)
- [194] J. Hoshen and R. Kopelman. Percolation and cluster distribution. I. cluster multiple labeling technique and critical concentration algorithm. *Phys. Rev. B*, 14:3438–3445, Oct 1976. [63](#)

BIBLIOGRAPHY

- [195] Dian Chen, Atsuhiro Nakahara, Dongguang Wei, Dennis Nordlund, and Thomas P Russell. P3HT/PCBM bulk heterojunction organic photovoltaics: correlating efficiency and morphology. *Nano letters*, 11(2):561–567, 2010. [64](#)
- [196] Zhaozhao Bi, Qinglian Zhu, Xianbin Xu, Hafiz Bilal Naveed, Xinyu Sui, Jingming Xin, Lin Zhang, Tengfei Li, Ke Zhou, Xinfeng Liu, et al. Efficient quaternary organic solar cells with parallel-alloy morphology. *Advanced Functional Materials*, 29(9):1806804, 2019. [82, 105](#)
- [197] Zhaozhao Bi, Hafiz Bilal Naveed, Xinyu Sui, Qinglian Zhu, Xianbin Xu, Lu Gou, Yanfeng Liu, Ke Zhou, Lei Zhang, Fengling Zhang, et al. Individual nanostructure optimization in donor and acceptor phases to achieve efficient quaternary organic solar cells. *Nano Energy*, 66:104176, 2019. [82, 105](#)
- [198] Minwoo Nam, Hye Yeon Noh, Junhee Cho, Yongkook Park, Sang-Chul Shin, Jung-A Kim, Jehan Kim, Hyun Hwi Lee, Jae Won Shim, and Doo-Hyun Ko. All-day operating quaternary blend organic photovoltaics. *Advanced Functional Materials*, 29(16):1900154, 2019. [82, 105](#)
- [199] Xiaoling Ma, Jian Wang, Qiaoshi An, Jinhua Gao, Zhenghao Hu, Chunyu Xu, Xiaoli Zhang, Zhitian Liu, and Fujun Zhang. Highly efficient quaternary organic photovoltaics by optimizing photogenerated exciton distribution and active layer morphology. *Nano Energy*, page 104496, 2020. [82, 105](#)
- [200] Kang Wei Chou, Buyi Yan, Ruipeng Li, Er Qiang Li, Kui Zhao, Dalaver H Anjum, Steven Alvarez, Robert Gassaway, Alan Biocca, Sigurdur T Thoroddsen, et al. Spin-cast bulk heterojunction solar cells: a dynamical investigation. *Advanced Materials*, 25(13):1923–1929, 2013. [84, 105](#)
- [201] Fiyanshu Kaka, Ravi K Singh, PC Ramamurthy, and Abhik Choudhury. Modeling process–structure–property relationship in organic photovoltaics using a robust diffuse interface approach. *AIP Advances*, 10(6):065304, 2020. [90](#)
- [202] Fiyanshu Kaka, Sumeet Khanna, PC Ramamurthy, and Abhik Choudhury. Investigation of process–structure–property relationship in ternary organic photovoltaics. *Journal of Applied Physics*, 128(14):145501, 2020. [90](#)

BIBLIOGRAPHY

- [203] Naveen Kumar. *Co-continuous microstructures through spinodal decomposition in ternary systems: A phase field study.* PhD thesis, Indian Institute of Science Bangalore, 2019. [102](#)
- [204] Stefanie Rechberger, Nicola Gasparini, Ranbir Singh, Min Kim, Christos L Chochos, Vasilis G Gregoriou, Kilwon Cho, Christoph J Brabec, Tayebeh Ameri, and Erdmann Spiecker. Unraveling the complex nanomorphology of ternary organic solar cells with multimodal analytical transmission electron microscopy. *Solar RRL*, page 2000114. [104](#)
- [205] John W. Eaton, David Bateman, Søren Hauberg, and Rik Wehbring. *GNU Octave version 5.2.0 manual: a high-level interactive language for numerical computations*, 2020. [110](#)